NOVA SCHOOL OF SCIENCE & TECHNOLOGY

DEPARTAMENT OF CHEMISTRY

ANA SOFIA BARRADAS DALOT

BSc in Forensic and Criminal Sciences

PLASMONIC NANOSTARS FOR SENSITIVE SERS-BASED IMMUNODETECTION

MASTER IN BIOTECHNOLOGY

NOVA University Lisbon

December, 2022

NOVA SCHOOL OF SCIENCE & TECHNOLOGY

DEPARTAMENT OF CHEMISTRY

PLASMONIC NANOSTARS FOR SENSITIVE SERS-BASED IMMUNODETECTION

ANA SOFIA BARRADAS DALOT

BSc in Forensic and Criminal Sciences

Adviser: Professor José Ricardo Ramos Franco Tavares
Associate Professor, NOVA University Lisbon

Co-advisers: Professor Hugo Manuel Brito Águas
Associate Professor, NOVA University Lisbon

Examination Committee:

President: Professor Carlos Alberto Gomes Salgueiro
Associate Professor, NOVA University Lisbon

Rapporteurs: Professor Maria Gabriela Machado de Almeida
Associate Professor, Egas Moniz School of Health and Science

Adviser: Professor José Ricardo Ramos Franco Tavares
Associate Professor, NOVA University Lisbon

Members: Professor Hugo Manuel Brito Águas
Associate Professor, NOVA University Lisbon

MASTER IN BIOTECHNOLOGY

NOVA University Lisbon
December, 2022

Plasmonic Nanostars for Sensitive SERS-based Immunodetection

Para o Paulinho, pela nossa vida

Para a minha família, por me ensinarem a ser como sou

ACKNOWLEDGEMENTS

First and foremost, I would like to thank Professors Ricardo Franco and Hugo Águas for giving me the opportunity to join and work in this lab.

To my adviser, Professor Ricardo Franco, for providing consistent support, guidance, and patience, and for always celebrating with me the good results.

To my co-adviser Professor Hugo Águas, for their support, insightful comments, and suggestions during this time.

To everyone from the Bionano lab, people that heard my lamentations. To Maria Enea, for always being curious about my work and for liking to hear me sing all day. Thanks to Diego Carvalho for teaching me all about protein purification! A special thanks to Maria João, for teaching me everything you know and encouraging me to research all my doubts. Thank you for all the "what are you doing?" and for making me think hard about everything that I'm doing; for reading all that I wrote; for all the suggestions; for listening; and for sharing the love of coffee and mint chocolate. Thank you so much MJ, without you, this thesis would be non-existent! To Alexandre, for listening to me and for putting your trust in my little knowledge.

À Raquel e à Melissa, por me ouvirem sempre! Obrigada pelas vossas palavras de apoio, por perguntarem sempre como está a correr e pela vossa força. Muito obrigada, estarei sempre com vocês passe o tempo que passar!

Para minha pequena grande família, pessoas trabalhadoras que me inspiram todos os dias. Muito obrigada a todos vocês que me apoiam sempre mesmo sem entenderem nada (muito menos inglês!), têm sempre uma palavra de apoio e um ombro para chorar se necessário. Por lutarem mais pela minha sanidade mental do que eu, e por isso por arranjarem sempre pretextos para jantaradas, às vezes até são de urgência. Mãe, és uma inspiração, que todos nós sejamos um dia como tu, lutadores e capazes de ganhar grandes batalhas como tu! Mana, obrigada por me surpreenderes sempre, por cresceres comigo e partilhares o teu grande conhecimento, mas especialmente por me teres dado três sobrinhos. Meus meninos, meus eternos bebés, obrigada por me animarem sempre e por me deixarem ser sempre

uma criança com vocês. Em especial ao terrível filho do meio, por me dares sempre a tua opinião em relação às minhas imagens e por tentares ajudar-me a trabalhar com o Blender!

Ao Paulinho, obrigada por tudo! E tudo nunca chegará nem metade para o que me dás. Obrigada por partilhares comigo a vida, pela nossa pequena e humilde casa e pela nossa pequenina família! É tudo graças a ti! Muito obrigada por todo o teu apoio constante, pelas lições de moral, pelas conversas pela noite fora mesmo após estes 5 anos, por fazeres de mim melhor, por me ouvires todos os dias, mesmo em modo automático, e pela nossa menina. És extraordinário e irei ser sempre sortuda por te ter ao meu lado, este diploma é também teu meu amor!

“There’s things more important than keepin’ a job.” (Rubeus Hagrid, J. K. Rowling)

“Imagination is the only weapon in the war against reality.” (Cheshire Cat, Lewis Carroll)

ABSTRACT

Malaria remains a global health problem and detection is essential to combat this disease. Rapid diagnostic tests in a lateral flow assay (LFA) format using *Plasmodium falciparum* histidine-rich protein II (*Pf*HRPII) as biomarker is the most common malaria detection method. These LFAs are usually low-cost and rapid but suffer from low sensitivity. Surface-enhanced Raman scattering (SERS) is a technique with high sensitivity and combined with LFA, is possible to detect *Pf*HRPII through colorimetric and SERS assays, increasing the limits of detection. The recombinant antigen *Pf*HRPII was expressed using a vector containing a His-tag in *Escherichia coli* and purified by a Ni-NTA column. The SDS-PAGE and western blot confirmed the presence of *Pf*HRPII with a molecular weight of 67 kDa (at 0.12 ± 0.03 $mg \cdot mL^{-1}$). The SERS tags were developed with star-shaped gold nanoparticles functionalised with a Raman reporter, 4-mercaptobenzoic acid, and covalently conjugated with an antibody. A proof-of-concept was made with Peroxidase/anti-Peroxidase complex with bovine serum albumin to block unspecific interactions and the SERS tags formation and activity were fully characterised through UV-Vis spectra, agarose gel electrophoresis, enzymatic activity assay, and dynamic light scattering. Each component of LFA was evaluated by the pixel intensity difference between the background and test line by ImageJ. The LFA optimisations led to the selection of a nitrocellulose membrane (CNPF8) not blocked, a sample pad (GFB-R7L), and an absorbent pad (AP-045). Anti-Peroxidase (0.9 $mg \cdot mL^{-1}$) and anti-IgG (0.5 $mg \cdot mL^{-1}$) were immobilised on the test and control lines, respectively. The sample was mixed into the SERS tags at 0.2 nM and deposited in the sample pad. The LOD and LOQ were determined as 5.24 and 7.28 $\mu g \cdot mL^{-1}$, respectively. Lastly, an LFA was incubated with recombinant *Pf*HRPII at 50 $ng \cdot mL^{-1}$ and the SERS performance was compared with a negative control (no *Pf*HRPII). The samples had a small but significant difference nevertheless further studies are needed to reduce the non-specific interactions from the control sample.

Keywords: Lateral Flow Assay; *Plasmodium falciparum* Histidine-Rich Protein II; Surface-Enhanced Raman Scattering; Surface-Enhanced Raman Scattering Tags; Malaria.

RESUMO

A malária continua a ser um problema de saúde global e a sua deteção é essencial para combater a doença. O método de deteção de malária mais comum é o teste de diagnóstico rápido em formato de teste de fluxo lateral (conhecido pelo acrónimo de LFA) usando como biomarcador a proteína rica em histidina II de *Plasmodium falciparum* (*Pf*HRPII). Estes LFAs são de baixo custo e rápidos, oferecem pouca sensibilidade. Espectroscopia de Raman aumentada pela superfície (conhecida pelo acrónimo de SERS) é uma técnica com grande sensibilidade e quando combinada com LFA, pode detetar *Pf*HRPII por análise colorimétrica e por SERS, aumentando os limites de deteção. O antigénio recombinante *Pf*HRPII foi expresso em *Escherichia coli* usando um vetor e purificado por uma coluna de níquel (Ni-NTA) através da cauda de histidinas. As técnicas SDS-PAGE e *western blot* confirmaram a presença de *Pf*HRPII com um peso molecular de 67 kDa (a 0,12 ± 0,03 $mg{\cdot}mL^{-1}$). As sondas de SERS foram produzidas com nanopartículas de ouro em formato de estrela, funcionalizadas com um repórter de Raman, o ácido 4-mercaptobenzóico, e conjugado covalentemente com um anticorpo. Através do complexo da enzima peroxidase/anti-peroxidase, e com albumina de soro bovino para bloquear interações inespecíficas, foi feito uma prova de conceito e a formação e a atividade das sondas de SERS foram caracterizadas através de espectro de UV-Vis, eletroforese em gel de agarose, ensaio de atividade enzimática e dispersão dinâmica de luz. Todos os componentes de LFA foram avaliados pela diferença de intensidade de pixel entre o fundo e a linha de teste por ImageJ. As otimizações de LFA permitiram a seleção da membrana de nitrocelulose (CNPF8) não bloqueada, do bloco de amostra (GFB-R7L), e do bloco absorvente (AP-045). O anticorpo anti-peroxidase (0,9 $mg{\cdot}mL^{-1}$) e o anti-IgG (0,5 $mg{\cdot}mL^{-1}$) foram imobilizados nas linhas de teste e controlo, respetivamente. A amostra foi misturada nas sondas de SERS a 0,2 nM e depositadas no bloco de amostra. O LOD e o LOQ foram determinados como 5,24 e 7,28 $\mu g{\cdot}mL^{-1}$, respetivamente. Por último, um LFA foi incubado com *Pf*HRPII recombinante a 50 $ng{\cdot}mL^{-1}$ e o desempenho de SERS foi comparado com o controlo negativo (sem *Pf*HRPII). As amostras tiveram uma pequena, mas significativa diferença, no entanto, são necessários mais estudos para reduzir as interações não específicas na amostra de controlo.

Palavras-chave: Teste de Fluxo Lateral; Proteína Rica em Histidina II de *Plasmodium falciparum*; Espectroscopia de Raman aumentada pela superfície; Sondas de Espectroscopia de Raman aumentada pela superfície; Malária.

CONTENTS

LIST OF FIGURES

LIST OF TABLES

ACRONYMS

ABTS	2,2'-azino-bis(3-ethylbenzthiazoline-6-sulfonic acid)
AGE	Agarose gel electrophoresis
ANOVA	One-way analysis of variance
APS	Ammonium persulphate
AuNP	Spherical gold nanoparticle
AuNS	Gold nanostar
BCA	Bicinchoninic acid
BSA	Bovine serum albumin
CCC	Critical coagulation concentration
CNPF8	Type of nitrocellulose membrane with pore size of 8 μm
CNPF10	Type of nitrocellulose membrane with pore size of 10 μm
CNPC12	Type of nitrocellulose membrane with pore size of 12 μm
CNPC15	Type of nitrocellulose membrane with pore size of 15 μm
CNPH70	Type of nitrocellulose membrane with wicking time of 70 s
CNPH90	Type of nitrocellulose membrane with wicking time of 90 s
CNPH150	Type of nitrocellulose membrane with wicking time of 150 s
CNPH200	Type of nitrocellulose membrane with wicking time of 200 s
COVID-19	Coronavirus disease 2019
DCLS	Direct classical least squares
DLS	Dynamic light scattering
DMSO	Dimethyl sulfoxide
DTNB	5,5'-dithiobis-(2-nitrobenzoic acid)
E. coli	*Escherichia coli*
EDC	1-ethyl-3-(3-dimethylamino)propyl)carbodiimide
IPTG	Isopropyl β-d-1-thiogalactopyranoside
LAMP	Loop-mediated isothermal amplification

LFA	Lateral flow assay
LOD	Limit of detection
LOQ	Limit of quantification
LSPR	Localised surface plasmon resonance
MBA	4-mercaptobenzoic acid
MES	2-ethanesulfonic acid
MW	Molecular weight
Ni-NTA	Nickel-nitrilotriacetic acid
NM	Nitrocellulose membrane
NP	Nanoparticle
P.	*Plasmodium*
***P*ALD**	*Plasmodium* aldolase
PBS	Phosphate-buffered saline
PBS-T	Phosphate-buffered saline and tween 20
PCR	Polymerase chain reaction
PDI	Polydispersity index
Perox	Horseradish peroxidase
***Pf*HGPRT**	*P. falciparum* hypoxanthine guanine phosphoribosyl transferase
***Pf*HRPII**	*P. falciparum* histidine-rich protein II
***P*GluDH**	*Plasmodium* glutamate dehydrogenase
pLDH	Parasite-specific lactate dehydrogenase
PVDF	Polyvinylidene difluoride membrane
RDT	Rapid diagnostic test
SDS	Sodium dodecyl sulphate
SDS-PAGE	Sodium dodecyl sulphate-polyacrylamide gel electrophoresis
SERS	Surface-enhanced Raman scattering
SNHS	N-hydroxysulfosuccimide
TAE	Tris-acetate-EDTA
TEMED	Tetramethylethylenediamine
TMB	3,3',5,5'-tetramethylbenzidine
Tris	Tris(hydroxymethyl)-aminomethane
UV-Vis	Ultraviolet-visible
WHO	World Health Organization

SYMBOLS

A	Absorbance
Δμ	Variations relative to the maximum mobility band
E	Strength of the driving field
ε	Extinction molar coefficient
$\boldsymbol{K_D}$	Dissociation constant
v	Velocity

1

INTRODUCTION

1.1 Malaria: impact worldwide, biology and diagnosis

Malaria is a serious global health problem, killing hundreds of thousands of people each year, particularly in low-income regions (Africa, Latin America, Caribbean, Asia, Eastern Europe, South Pacific)[1]. The most concern involves children aged under 5 years, which corresponded to 77% of total malaria deaths (627,000) in 2020. Malaria cases in eighty-five malaria-endemic countries in 2020 reached 241 million cases, 14 million more than in 2019[2]. The growth in 2020 was linked to a shift in investment in the coronavirus disease 2019 (COVID-19) pandemic rather than malaria, as well as a shortage of malaria medications and limited access to medical facilities[1]. In 2020, malaria deaths increased by 12% when compared to 2019, and is estimated that 68% of the additional deaths were due to service disruptions and restrictions of isolation during the COVID-19 pandemic[2].

The infection by malaria disease requires two hosts, a human host, and a mosquito host[3]. The infection of the human host starts with a bite from female *Anopheles* mosquitoes and the injection of the *Plasmodium* sporozoites into the human body[4]. There are many species of *Plasmodium (P.)*, such as *P. falciparum*, *P. malariae*, *P. ovale* and *P. vivax*. *P. falciparum* is the most pathogenic species, and if not treated promptly, it can be fatal[5,6]. Several proteins produced and excreted by *P. falciparum* were identified that can be used as a biomarker, such as knob-associated histidine-rich protein, histidine-rich protein II (*Pf*HRPII), histidine-rich protein III, and membrane-associated histidine-rich protein, among others[7].

As seen in Figure 1.1, the life cycle of *P. falciparum* has two stages, sexual and asexual. The sexual stage occurs in the mosquito host, which is infected when feeds on a human infected by ingesting gametocytes and can infect others through bites, transferring sporozoites formed during an asexual stage in the mosquito into the human host. These sporozoites are transported by the blood into the liver, where they asexually divide to form merozoites, which are discharged into the bloodstream, where they infect erythrocytes. These erythrocytes rupture and release merozoites in the circulation, which can cause a reinvasion of the erythrocytes, and can also differentiate into sexual stages, gametocytes[3].

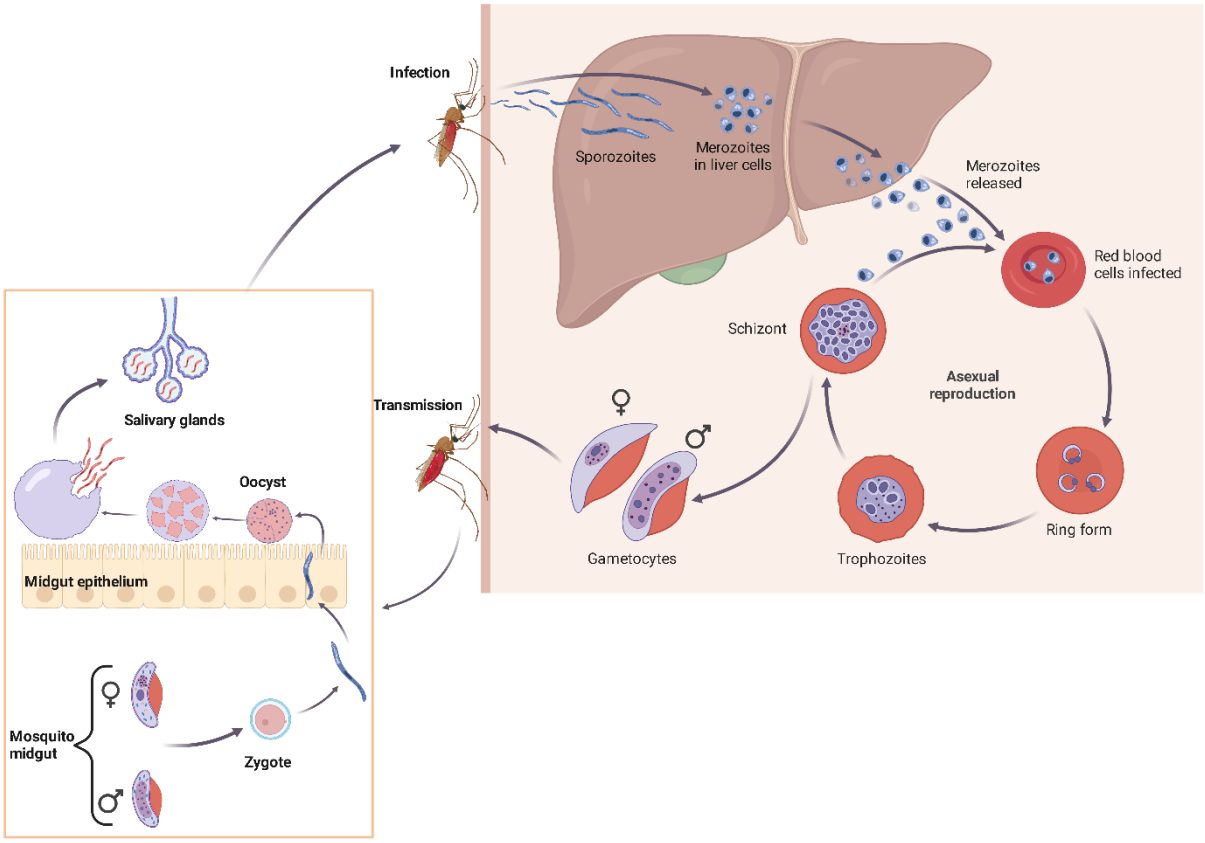

Figure 1.1: Life cycle of *Plasmodium falciparum*. Malaria infection is initiated when a mosquito infected injects sporozoites into the human host. This sporozoite is carried to the liver, where it divides asexually to generate merozoites, which are secreted into the bloodstream and infect the erythrocytes. Then, the merozoites can reinvade erythrocytes multiple times, or can differentiate into sexual stages, gametocytes. When a mosquito takes a bite in this infected host, ingests the gametocytes and a sexual cycle is initiated in the mosquito. This mosquito infected can bite again, in which the sporozoites formed during an asexual stage in this mosquito are injected, and the life cycle is completed (designed with BioRender).

Malaria infection produces usually febrile illness, and sometimes other accompanying symptoms such as chills, headache, nausea, and muscle pain. This infection can be treated, and the symptoms can disappear after a few days. In the case of untreated or partially treated individuals, the initial infection, uncomplicated (absent or very low symptoms) malaria, can progress to severe malaria, which may lead to death. The severity of malaria varies depending on several factors such as the age of the patient, immunity, the use of antimalaria drugs and the level of transmission. Young children have a different, typically more severe response to this disease because they have not yet developed protective immunity[6]. Severe malaria disease occurs especially in non-immune patients and have the following syndromes, which can occur separately or in combination: severe anaemia, cerebral malaria, respiratory failure and acute renal failure[8]. Cerebral malaria occurs when several mature-infected parasites enter the cerebral microvasculature, which can promote coma[6]. Severe malaria in older children and adults are very rare since these individuals have already developed immunity[6]. The immunity can be acquired or adaptive and exists various types such as anti-disease immunity, which offers defence

against clinical illness and influences the risk and degree of morbidity related to a specific parasite density, anti-parasite immunity, providing defence against parasitaemia affecting the density of parasites, and premunition, which shields against future infections by preserving a mild parasitaemia that usually causes no symptoms[9]. In adults and in areas with lower transmission (*e.g.*, Asia), severe malaria has more frequently symptoms of renal and hepatic dysfunction, although cerebral malaria, hypoglycaemia, and anaemia are also present[6]. Pregnant women are particularly vulnerable to malaria infection due to iron deficiency, which is a common problem during the pregnancy and a problem in malaria-endemic areas. *P. falciparum* in pregnant women infects the red blood cells that adhere to and accumulate in the placenta, which causes anaemia and low birth weight in new-born babies. This infection in pregnant women can cause abortions, premature deliveries, or death in utero[10].

1.1.1 Biomarkers for malaria detection

There are several biomarkers that can be used in malaria diagnosis such as *P. falciparum* histidine-rich protein II (*Pf*HRPII), parasite-specific lactate dehydrogenase (pLDH), *Plasmodium* aldolase (*P*ALD), *P. falciparum* hypoxanthine guanine phosphoribosyl transferase (*Pf*HGPRT) and *Plasmodium* glutamate dehydrogenase (*P*GluDH) and malaria pigment hemozoin[11]. The reason that these biomarkers are used and the possible method of detecting malaria are discussed below.

1.1.1.1 *Plasmodium falciparum* histidine-rich protein II

*Pf*HRPII is an antigenic protein and was identified during 1970s by Araxie Kilejian[12], and is exclusively produced by *P. falciparum*. *Pf*HRPII has an amino acid composition of approximately 34% histidine, 37% alanine and 10% aspartic acid[7,13,14]. Its low-complexity amino acid sequence, since contains repeats of single or short amino acid motifs, and is prone to polymorphism, leading to a variation of number and type of the repeated protein sequence[7]. This protein has been studied for a long time, the precise function of *Pf*HRPII remains undeterminated[7,13], although it has been reporter that is involved in the formation of hemozoin[15], heme binding[16], suppression of the immune response[17], and Zn^{2+} binding[13]. *Pf*HRPII has high levels of expression compared with the other biomarkers, accumulates in the host plasma, due to the rupture of infected erythrocytes[7,13,14]. For this reason, it has been found *Pf*HRPII in plasma, saliva, and urine in patients infected with *P. falciparum*, and due to its high stability, *Pf*HRPII can remain for days or weeks after treatment[14,18]. Since *Pf*HRPII levels in bloodstream are high and stable for long periods of time, this protein has been used as a biomarker for the disease studies and development of detection tools. The production at large scale of recombinant

*Pf*HRPII can generate a variable reactivity over different rapid diagnostic tests (RDTs) because their design is based on a single copy of a given vector with recombinant *Pf*HRPII[14].

1.1.1.1.1 Expression and purification of recombinant *Pf*HRPII

The production of proteins is commonly made by bacterial expression system, as *Escherichia coli* (*E. coli*). The use of this bacteria is preferred to express foreign proteins since is easy to manipulate, growths at low-cost carbon source, and can quickly produce the recombinant protein[19,20]. Exists several strategies to overexpress a desirable protein, including through a fusion protein in a soluble fraction. These fusion proteins include a "tag" that is especially used for the specific affinity purification[19]. Among the several affinity tags, the more common is the poly-histidine tag (His-tag) and the glutathione S-transferase tag, which allows the target protein to be purified through immobilised-metal affinity chromatography and glutathione-based resins, respectively[19,20]. Hence, recombinant *Pf*HRPII can be produced by *E. coli* as host with a vector which has the coding sequence for the protein *Pf*HRPII with an N-terminal His-tag[18].

Proteins can be purified by several methods, as bulk methods, chromatographic methods, affinity methods, and electrophoretic methods[21]. Among the several techniques, affinity methods, more specific immobilised-metal affinity chromatography, is one of the most used due to its simplicity and high specificity for His-tagged proteins[22].

A His-tag, which contains six or more consecutive histidine residues, is usually fused to the N- or C-terminus on the recombinant protein to facilitate its purification and detection. Protein purification with a His-tag is based on an affinity chromatography using chromatography resins containing a chelating ligand, such as nitrilotriacetic acid (NTA) with an immobilised divalent metal (*e.g.*, Ni^{2+} or Cu^{2+})[22]. The affinity of the His-tag to the chelating ligand depends on its primary structure, since His-tag usually does not affect the folding of the protein and *Pf*HRPII has low-complexity sequence which indicates lack of secondary structure, it can be purified under native or denaturing conditions[7,22]. The NTA strongly binds to the metal Ni^{2+} ions because it takes up four of the ligand binding sites, leaving two sites open for interaction with the His-tag[23], forming a coordination complex[24]. This allows for the His-tagged protein to remain immobilised while contaminants are washed away, sometimes even under harsh conditions. Following, the protein can be eluted smoothly through conditions mild and flexible, as competition with imidazole or a reduction of pH. The nickel-nitrilotriacetic acid (Ni-NTA) resin is very stable and simple to work with, and the ratio of Ni-NTA resin to the His-tagged protein should be adjusted to the amount of His-tagged in the sample, a parameter that has the highest impact on purification[22,25].

1.1.1.2 Parasite-specific lactate dehydrogenase

pLDH is the most abundant water-soluble enzyme in *P. falciparum* produced both in sexual and asexual stages. This enzyme is found in the glycolytic pathway, converting pyruvate to lactate in the last step of glycolysis[11]. There are different isomers of pLDH for each of the four *Plasmodium* spp. that infect humans, and their detection can be used for point-of-care devices[26]. pLDH is as commonly used in RDTs as *Pf*HRPII and appears to be a more trustworthy diagnostic target since it is produced by live parasites, *i.e.*, the absence of pLDH is indicative that the patient is not infected. pLDH can be also detected by measuring its enzymatic activity[27].

1.1.1.3 *Plasmodium* aldolase

*P*ALD is an enzyme present in glycolytic pathway of the parasite, that contributes significantly to energy production by converting fructose-1,6-bisphosphate to glyceraldehyde-3-phosphate and dihydroxyacetone phosphate. The active and soluble form of the enzyme is found in the parasite's cytoplasm and is also bound to the parasite's membrane[11]. Aldolase is essential for parasite survival, so it could be used as a marker or target molecule in the development of sensors for malaria diagnosis[26]. This protein is present in all malaria species, which can be used to detect individual species[7]. RDTs based on *P*ALD have shown poor sensitivity and are suitable at higher parasitaemia in the sample. Thus, these *P*ALD-based RDTs have been used for evaluating the treatment during infection where the parasitaemia levels are high[27].

1.1.1.4 *P. falciparum* hypoxanthine guanine phosphoribosyl transferase

*Pf*HGPRT is a key enzyme in the parasite's purine metabolism, that is reported to be essential for the growth of this parasite. Despite the fact that a similar protein is found in both bacteria and humans, it can be used as a reliable target for malaria diagnosis and therapeutic applications[11]. These enzymes are not normally used since they are unstable during the purification and storage to proceed with further studies[28].

1.1.1.5 *Plasmodium* glutamate dehydrogenase

*P*GluDH is an enzyme present in *Plasmodium* parasites but is not found in host red blood cells. It is essential for parasite survival and growth because it connects the carbon and nitrogen metabolisms. Even though malaria parasites have different isoforms of *P*GluDH, these enzymes serve as a reliable and selective biomarker for malaria diagnosis[11]. This enzyme can detect the presence of the *P.*

falciparum parasite by western blotting, as described by the authors Rodríguez, *et al.*[29] and can be used in an enzyme-type method[29].

1.1.1.6 Malaria pigment hemozoin

Plasmodium parasites consume red blood cells as source of amino acids during an infection, resulting in the formation of heme, which is extremely toxic. To avoid the toxicity of heme and survive, the parasites convert it into hemozoin, an inert, insoluble, crystalline brownish-red pigment. Hemozoin is absent in healthy people, so it serves as a biomarker for diagnosis of malaria[11] by flow cytometry and automated blood cell counting techniques[27].

1.1.2 Current malaria diagnosis methods

Malaria clinical diagnosis based on symptoms evaluation, is frequently the initial one made by a medical doctor and normally is followed by other methods of detection[30]. These include microscopy[31], nucleic acid amplification tests[32], fluorescence[33], and RDTs[26] methods, among others[31]. The symptoms of malaria are very similar to many other diseases such as flu, gastroenteritis, septicaemia and viral diseases[34], misleading to a false diagnosis and contributing to malaria drug-resistant strains, therefore it is very important to have other methods to prove the disease[5].

1.1.2.1 Microscopic analysis method

The microscopic analysis is widely considered the gold standard method for malaria diagnosis. This method allows the visualisation of morphological stages of parasites and the quantification of the density of parasite infection, under a light microscope by thick and thin blood smear and staining. The staining and visualisation processes are time-consuming, and the sensitivity of this method depends on the instrument, staining protocol, and the technician's skill, as well as on the quality of the reagents used. A trained technician can detect 5-10 parasites·μL^{-1} of blood, while a non-expert can detect only > 50 parasites·μL^{-1}. Although this method has a very low cost, an expert is required to analyse the samples, so that mixed infections and low parasitaemia do not lead to misdiagnosis[30,31].

1.1.2.2 Nucleic Acid Amplification Tests

Polymerase chain reaction (PCR) technique allows specific amplification of malaria DNA. When compared with the microscopic method, this method has higher specificity and sensitivity for all four species of human malaria parasites, and can detect 1-5 parasites·μL^{-1} of blood[32]. PCR can also

detect drug-resistant parasites, mixed infections, and quantification at low parasitaemia by real-time PCR, and this process can be automated to large amounts of samples[32]. Nevertheless, both expensive laboratory equipment and technical expertise are required, which is not suitable for low-income countries[30,31].

Loop-mediated isothermal amplification (LAMP) is a simple, quick, and easy to perform technique, used to amplify specific DNA sequences. A high expertise can detect as low as 5 parasites·μL^{-1} with this technique. Also, LAMP has a moderate cost, but reagents need cold storage[31].

1.1.2.3 Immunofluorescence antibody test

Malaria can be also diagnosed by detecting specific antibodies produced during the immunological response of the human host against malaria parasites, namely immunofluorescence antibody test[30,31]. The principle of this method identifies specific antibodies produced two weeks after the infection, which can endure until 3-6 months after this infection, by using a specific antigen or crude antigen. This method is simple, highly sensitive and specific, but it cannot correlate to clinical symptoms because of the prevalence of *Pf*HRPII antibodies in the bloodstream. It can also quantify IgG and IgM antibodies present in serum samples, however, it is not possible to determine the parasitaemia in the patients[30,31]. It is time-consuming and requires fluorescence microscopy and trained technicians, which is not suitable for areas without electricity. Therefore, this method is not useful for making decisions regarding the treatment of patients[33].

1.1.2.4 Rapid diagnostic tests

RDTs based on a lateral flow assay (LFA), consist of the migration of a blood sample through the surface, such as a nitrocellulose membrane (NM). The parasite antigen present in the peripheral blood is captured by a monoclonal antibody that is conjugated to gold nanoparticles or other type of signal transducers[26]. This method is simple, has rapid results, is easy to perform, is suitable for fieldwork and does not require specific equipment, or electricity or special training to perform and interpret the results[30,31].

World Health Organization (WHO) recommends that for RDTs should achieve at least 75% in "panel detection score" for low parasite density samples (200 parasites·μL^{-1}), and less than 10% of false positive tests and fewer than 5% of invalid tests[35]. These false positive results are recorded in cases when the gametocytes are present in the peripheral blood and are absent of asexual parasitaemia[30]. The RDTs are constructed to detect target antigens abundant in all asexual and sexual stages of the parasite. Currently, the RDTs are focused to detect *Pf*HRPII specific for *P. falciparum*, and pLDH or *P*ALD from the glycolytic pathway found in all parasite species. *Pf*HRPII-based RDTs

will have negative results for samples containing other human malaria species, therefore the patient will be misdiagnosed as malaria negative. These tests may remain positive after the host is clear from the infection since *Pf*HRPII persists in the host after weeks[26]. Other variabilities exist for these tests, such as the presence or absence or variation in number of the target epitope, genetic variability of number of alanine- and histidine-rich amino acid repeats and its size between strains, and rare amino acid variants[36]. Normally, it is used *Pf*HRPII-based RDTs, except in areas where ≥ 5% of *P. falciparum* cases results in negative RDTs due to *pfhrp2/3* deletions, codons with low complexity which encodes mostly tri- or hexapeptide repeats[7]. In these areas where these deletions are common, it is used RDTs to detect *P. falciparum* and to detect and discriminate *P. falciparum* from non-*P. falciparum* infections (*e.g., P. vivax*). These RDTs can be exclusively for the detection of the protein *Pf*HRPII, or the enzyme pLDH, or alternatively, can be in some cases a combination of protein and enzyme in the same test line or in separated test lines[35].

1.2 Gold nanoparticles and their application in immunoassays

Spherical gold nanoparticles (AuNPs) are materials with at least one dimension less than 100 nm and distinct optical, physical and chemical attributes from their bulk counterparts, which is excellent for the assembly of chemical and biological sensors[37]. Because their reduce size, AuNPs have unique optoelectronic properties and a high surface-to-volume ratio offering a reactive surface suitable for many applications including in clinical diagnostics due to the gold biocompatibility[37,38].

Among the interesting proprieties of AuNPs, the localised surface plasmon resonance (LSPR) phenomenon is the feature that showed the most promise in biosensor field because it can be linked to the presence or absence of target biomarker[37,38]. For metal nanoparticles (NPs) having a smaller dimension than the wavelength of incident light, LSPR is an optical phenomenon caused by free electron oscillations at the surface of NPs in resonance with the incident electromagnetic field. Therefore, these metal NPs produce absorption and scattering spectra, and so their LSPR peaks are referred to as extinction spectra. The energy of the LSPR band depends on the composition, size, shape (*e.g.*, nanorods, nanotriangles, nanostars), and dielectric environment of the nanoparticle[39,40]. AuNPs with a spherical shape possess one extinction peak in the visible-near-infrared frequency region, and the variation of their size leads to changes in the LSPR extinction maximum. For instance, AuNPs with a diameter of 15 nm have an LSPR maximum at 520 nm, which red shifts to 600 nm as the diameter increases to 100 nm[41]. The difference between the sizes of AuNPs is explained by the relative magnitude of the absorption cross-section and the cross-section of scatter. Therefore, the red shift occurs because

more light is dispersed than absorbed with increasing size[39]. AuNPs with a spherical shape have a narrower LSPR band, while varying the shape creates more than one absorption peak, *i.e.*, a LSPR band larger, such as triangles, cubes, and nanostars due to the junction of several LSPR that are generated. Increased edges in the NPs results in a red shift and a different colour in the nanoparticle solution[39,42]. AuNPs with different shapes have unique and different LSPR bands than the spherical AuNPs increasing the potential of NPs for biodetection[43,44]. Star-shaped gold nanoparticles, also known as gold nanostars (AuNSs), have a structure containing multiple sharp edges, whose optical properties can be changed from the visible to the near-infrared region by altering their size and number of tips[45]. The AuNSs have the LSPR peak around 647, 700, 783 nm, with a size of 100 nm, as we can see in Figure 1.2 the difference between AuNPs and AuNSs.

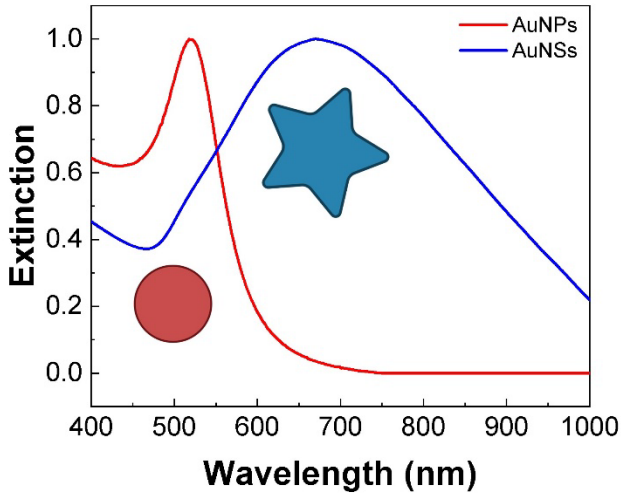

Figure 1.2: UV-Vis spectra of AuNPs and AuNSs. Spherical gold NPs (AuNPs) with a diameter of ca. 15 nm, have an LSPR maximum wavelength around 520 nm, and star-shaped gold NPs (AuNSs) have an LSPR maximum wavelength around 670 nm.

AuNPs have many applications in different fields, including medicine, cellular and molecular biology, microbiology, immunology, and physiology[46]. In biosensors, AuNPs can increase the sensitivity in detection of tests due to their optical properties, biocompatibility and their easily conjugation with several molecules, improving the detection sensitivity of fluorescence, chemiluminescence, surface plasmon resonance (SPR) and surface-enhanced Raman scattering (SERS)[47]. The tips from AuNSs provide “hot spots”, explained by the enhanced field around the tips. Also, the LSPR band shifts to the near-infrared region, which is a good feature for application in SERS substrates to be used in biodiagnostic and chemical detection[41,48] due to the reduction of autofluorescence of biological materials, and the advantage to pass the deep tissue in imaging, when used near-infrared laser

excitation[49,50]. One application that is widely known these days is the LFA, which AuNPs captures in the sample an antigen and conjugates the test line, producing a coloured line.

1.2.1 Plasmonic based detection and Surface Enhanced Raman Spectroscopy

The LSPR phenomenon, describe before 1.2 in Introduction, can be used to detect DNA and other molecules by visual inspection and through light absorbance spectroscopy, where when the DNA is not present the AuNPs are not stabilised leading to aggregation, which leads to a change of colour and a shift in the LSPR[51].

SPR is an optical technique that is used to monitoring the changes in the refractive index after the attachment of a target molecule to a planar metal sensor. This device can be developed by using a streptavidin-coated gold surface with biotinylated aptamer immobilised, where an avian influenza virus H5N1 is recognised and detected[52,53].

Raman spectroscopy is a rapid and non-destructive spectroscopic technique, which relies on inelastic light scattering by molecules, known as Raman scattering[54]. The vibrational excitation depends on the environment through the chemical interaction, while the absorption and the re-emission depends on the availability of photonic states at the positions of the molecules. The re-emission has different frequencies, which the sum or difference results in anti-Stokes or Stokes Raman scattering, respectively[55]. These energy differences between the vibrational states reflects in the modification of the energy of the photons, resulting in a Raman spectrum that gives the chemical "fingerprint", identifying the analyte[42]. SERS combines the specificity of a biomolecular fingerprint with improved sensitivity brought on by the intensification of the Raman signal of molecules close to a plasmonic nanostructure. There are two different enhancement mechanisms: electromagnetic and chemical enhancement. The first one is associated with plasmon excitation in metal NPs, and chemical enhancement is related to the target molecule adsorbed to metal nanoparticle electron transfer capabilities. Enhancement factors can achieve up to 10^8 or even larger, opening the way for single molecule detection[53,55]. By utilising anisotropic NPs, SERS generates an enhanced Raman signal for molecules adsorbed to the surface of NPs, such as 4-mercaptobenzoic acid (MBA). The presence of "hot spots", such as spaces between NPs, aggregates, or sharp edges or tips of AuNSs, can also enhanced the Raman signal[39,42]. The "hot spots" present in the AuNSs provide an enhanced Raman signal and if these AuNSs are functionalised with a molecule, this signal can have a further enhancement that in specific conditions can detect single molecules[56]. In SERS-based immunoassay can be used, for example, a AuNSs labelled with a Raman reporter conjugated with an antibody, providing selectivity and specificity to detection[39]. As example, the authors Oliveira *et al.*[57] developed a SERS immunoassay were in

a cellulose hydrogel-based platform can detect the presence of a protein, which in this case was horseradish peroxidase (Perox)[57].

1.2.2 SERS tag development

SERS tags merge metallic NPs, such as gold or silver, and a Raman reporter molecule absorbed on the surface of the NPs, which has a known spectrum[49,58]. Normally it is used spherical NPs (*e.g.*, AuNPs), due to their easy synthesis. Nevertheless, spherical NPs provide a weak enhancement of the molecules Raman signals which can be further improved by using aggregates of the spherical NPs (obtained by increasing the ionic strength of the medium, for example), or different using anisotropic AuNPs, such AuNSs[58]. The functionalisation of the AuNPs and AuNSs with a Raman reporter molecule or SERS tag, grants the amplification of the unique Raman vibrational fingerprint of a molecule due to the strong electromagnetic fields at the particle surface that polarise the local volume around the nanoparticle and ideally, the molecule chosen can simultaneously act as a coating layer, *e.g.* MBA[59]. SERS tags have multiple advantages, such as (i) highly sensitivity to detect molecules that are in the surface of the NPs; (ii) they can be used for multiple detections and (iii) can be used in a quantitative analysis by a specific binding between the target and the SERS tag[58]. Despite their exciting advantages, SERS tags still have some problems that need to be addressed before their final application in bioanalysis, such biocompatibility, toxicity and long-term stability[49].

1.2.2.1 Synthesis of gold nanoparticles

The synthesis of AuNPs can be accomplished by two approaches, "top-down" and "bottom-up" methods. Depending on the method, it is possible to control their size, shape, solubility, and stability[38,60].

The "top-down" synthesis is based on a physical manipulation whereby a bigger material is broken down into smaller parts, resulting into NPs[38,60]. Decomposition techniques as grinding/milling and physical vapor deposition are examples of this method[38,60].

The "bottom-up" approach is a chemical transformation, which starts with simpler substances, and it is build up until the formation of NPs. Examples of this method include synthesis with reduction of metal salts and the seeding-mediated growth[38,60].

The most common NPs synthesis is based on the reduction of gold with citrate as a reducing agent acting simultaneously as a capping agent for stabilizing the AuNPs colloidal solution, and a pH mediator by modifying the reactivity of AuNPs which reflected in their reduction potential, resulting in lower NPs sizes. Normally, this synthesis results in AuNPs with varying sizes of 8 to 150 nm[61].

This synthesis was developed by Turkevich[62] in 1951, and since then many others approaches have been developed varying parameters including the $HAuCl_4$/trisodium citrate ratio, pH control, and temperature which influence NPs size and stability. In 2011, Ojea-Jiménez *et al.*[61] proposed a different approach, where a change in the order of reagent addition results in an improvement in the size distribution and a uniform spherical shape[38,63].

The synthesis by seeding-mediated growth uses small AuNPs as seeds to produce monodisperse larger particles or NPs with different shapes, such as nanorods, branched gold nanocrystals, nanoplates and AuNSs[64,65]. Yuan *et al.*[66], described a method where it is used silver nitrate to assist the anisotropic growth, AuNPs as seeds to form smaller AuNSs size (< 100 nm diameter) and ascorbic acid, where ascorbic acid and silver nitrate are added simultaneously[66].

1.2.2.2 Functionalisation and bioconjugation of gold nanoparticles

AuNPs and AuNSs can interact with several molecules, *i.e.*, enzymes, proteins, DNA, etc. This interaction can have many applications, such as photo thermal therapy, targeting, drug delivery, imaging and toxin and microbial agent removal[46].

The molecule MBA is a Raman probe molecule with thiol and carboxylic groups that anchor to the AuNSs through the thiol group functioning as a Raman reporter and as a linker to other molecules due to the carboxylic group[67]. This molecule can preserve the colloidal stability, acting as a stabilising agent, and binds to AuNPs and AuNSs surface through chemisorption[68]. AuNPs synthetised by citrate reduction have in their surface negative citrate ions, which binds to the thiol group from MBA through chemisorption, leaving the carboxyl group deprotonated, and so the surface remains negatively charged at pH 7.5[63,68]. As seen in Figure 1.3, AuNPs and AuNSs functionalised has a red shift of the LSPR peak of 3 and 11 nm, respectively.

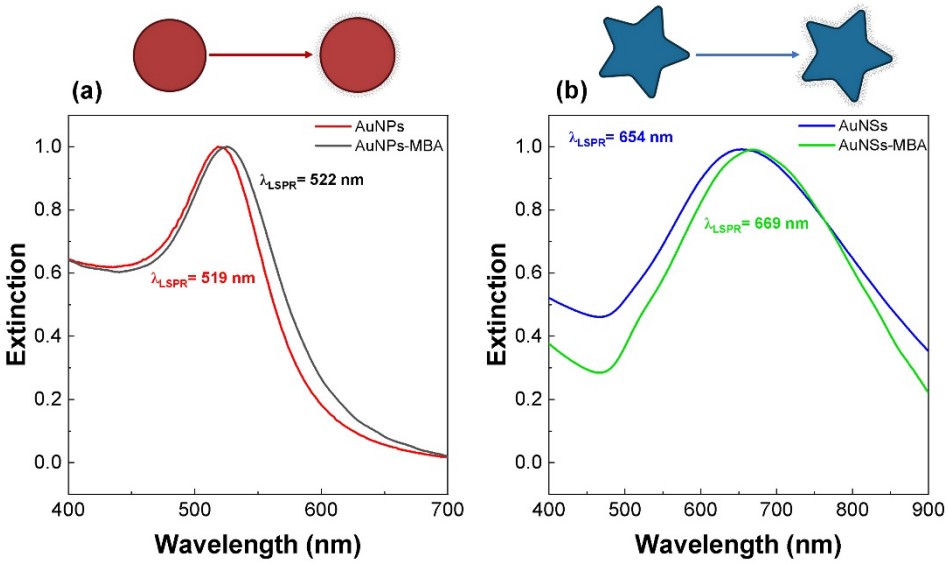

Figure 1.3: UV-Vis spectra of AuNPs (a) and AuNSs (b) and both functionalised with MBA. A successful functionalisation is confirmed with a red shift of the LSPR peak of 3 and 11 nm for AuNSs and AuNPs, respectively.

The AuNPs and AuNSs can be conjugated with a targeting component, such as antibody, and these conjugations can happen by a covalent or non-covalent bound to the existing capping agent[69].

The non-covalent conjugation, *i.e.*, electrostatic interactions, between an antibody and NPs occurs as a spontaneous absorption in the surface of the NPs. This conjugation has some obstacles, for instance it is necessary high concentrations of antibody to produce NPs-antibody conjugation, the antibody can have a random orientation on the NPs surface, which can be difficult to capture a protein of interest, this binding can change the pH and the antibody in the surface of NPs can be replaced by other molecules[69].

The covalent conjugation between the antibody and NPs surface happens with a mediator linker, as the use of 1-ethyl-3-(3-dimethylamino)propyl)carbodiimide (EDC) and N-hydroxysulfosuccimide (SNHS) (EDC/SNHS) coupling. The NPs functionalised with MBA have a carboxyl group to covalent binding, which forms a reactive NHS ester within contact with EDC/SNHS. This ester can form a covalent bound when in contact with a primary amine group in an antibody. This conjugation has a stronger bound and a more stable NPs-antibody conjugate than the non-covalent conjugation, although pH variations can decrease this efficiency[69,70].

1.3 Lateral Flow Assays

LFA is a conventional test strip that is one of the most adopted in commercial formats (*e.g.,* pregnancy testing, COVID-19 Rapid Antigen Test). These tests are commonly used in point-of-care

testing, because of their simple, cost-effectiveness and quick response[71]. Noble metal NPs, such as AuNPs, are the most commonly used as a colorimetric indicator because of their ability to form conjugates with biomolecules and to their high surface area, stability and intense red colour[72].

LFA is composed of two parts: chromatographic system and immunochemical reaction. The chromatographic system is based on the separation of the basis of the mixture on the differences in transmembrane migration capacities via capillary forces[73]. The immunochemical reaction is between antibody-antigen or nucleic acid-analyte with specific recognition of the target. An LFA device has four parts: a nitrocellulose membrane (NM), a sample pad, a conjugation pad, and an adsorption pad (Figure 1.4). The sample is loaded on the sample pad and moves by capillarity through the conjugate pad, where the target in the sample is specifically captured by the optical tags in the conjugate pad. These optical tags consist of optical NPs (*e.g.*, AuNPs) functionalised with molecules (*e.g.*, antibodies and aptamer) that recognize and capture the target. The sample continues moving toward the adsorption pad, and the complex formed (*e.g.*, AuNPs conjugated with the antibody and the target) can be immobilised by the capture probes that are fixed on the test line. The control line appears by the capture of excess optical labels with or without the target is present and is used to test if the LFA are functioning properly, which is necessary to determine if the test is positive or negative (Figure 1.4)[72]. The adsorption pad absorbs the excess reagents and prevents the backflow of the sample[74].

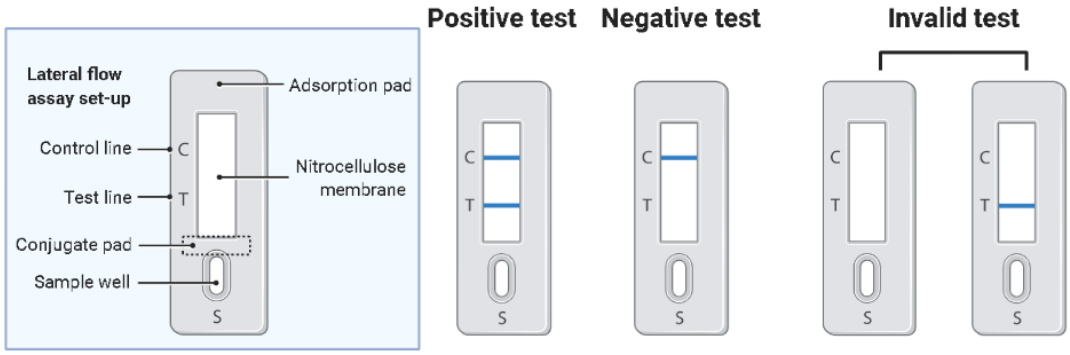

Figure 1.4: Representation of an LFA. Is composed by a NM, a sample pad, a conjugation pad, and an adsorption pad. The sample in the sample pad migrates via capillary forces until it reaches the adsorption pad. The positive and negative tests are valid when a colour line appears in the control line, which indicates that the LFA is functioning properly. When this colour does not appear, the test is invalid (designed with BioRender).

There are usually two main sensing strategies: competitive or non-competitive (sandwich) assays. In the competitive assay, the target in the sample and the labelled target (in conjugate pad or in test line) compete for the test-line capture bioreceptor. Usually this class of assay, is used for small target molecules (<1 kDa), which cannot bind to two antibodies simultaneously, therefore the analyte blocks the binding sites on the antibody and then block the interactions with the conjugate, resulting in

a positive test when there is no signal on the test line. The higher target concentration results in a lower intensity signal. The sandwich (non-competitive) assay detected mid- and big-size analytes (>1 kDa) (*e.g.*, proteins and antibodies), and the presence of the test line indicates a positive result. The target molecule is captured by the detection bioreceptor in the conjugate pad, and the test line captures the target molecule with the bioreceptor, producing a signal that increases with the concentration of the target in the sample[75]. The control line has a species-specific anti-immunoglobulin antibody that binds to the antibody in the conjugate, producing a signal[74].

Although AuNPs are the most used as labels, LFAs have significant limitations for applications demanding highly sensitive detection. Several LFA systems with improved sensitivity were developed, such as with anisotropic NPs (*e.g.*, AuNSs) and with SERS labels[76]. For increased sensitivity, fluorescence-based, enzyme-amplified signal and magnetic-nanoparticle-based LFA systems have been proposed, but they involve a complicated preparation and/or experimental process or they present increased optical interferences[72,77].

1.4 Surface Enhanced Raman Spectroscopy as an ultrasensitive detection technique for Lateral Flow Assay

SERS-based test strips with AuNSs have an increased sensitivity than the conventional colloidal test strips. Nevertheless, anisotropic NPs have lower colloidal stability than the more commonly used spherical NPs, which may cause problems in obtaining reproducible assays[72].

Several SERS-based LFAs have been developed for single and multi-targets detection, where this last has several line tests or multiple Raman-labelled SERS probes for different targets. These test strips can be designed in competitive or sandwich assays, and uses isotropic (*e.g.*, AuNPs, core-shell NPs of gold core with silver shell, core-shell NPs of silver core with gold shell, etc.) or anisotropic (*e.g.*, AuNSs, nanoflowers, gold nanorods, etc.) NPs and a Raman reporter (*e.g.*, 5,5'-dithiobis-(2-nitrobenzoic acid) (DTNB), MBA, 4-aminothiolphenol)[72]. As an example, Lin *et al.*[77], developed a SERS-LFA with AuNSs as the tags, functionalised with 4-aminothiolphenol and an antibody. This LFA has a competitive format between the target (bisphenol A) and 4,4-bis(4-hydroxyphenyl) valeric acid-bovine serum albumin, where the Raman intensity was inversely proportional to the concentration of bisphenol A[77]. The authors Zhang *et al.*[78] developed another example of a competitive assay, where is possible to detect six major mycotoxins simultaneously, aflatoxin B1, zearalenone, fumonisin B1, deoxynivalenol, ochratoxin A, and T-2 toxin. In another example, core-shell NPs of gold core with silver shell were prepared with two Raman reporters, DTNB and MBA, and one single LFA has three tests lines, whereby each test line had two different capture antigens[78].

Sánchez-Purrà, *et al.*[76] developed a SERS-based LFA to detect Zika and Dengue biomarkers. This LFA can detect these biomarkers visually and through Raman spectroscopy, relating the image analysis with the Raman signal. This assay was performed with AuNSs with two Raman reporters, MBA and 1,2-bis(4-pyridyl)ethylene. These SERS tags were captured in the test and control line after incubated with the sample, and the test line was analysed afterwards. The authors obtained a limit of detection (LOD) of 0.72 ng·mL^{-1} and 7.67 ng·mL^{-1} for Zika and Dengue, respectively[76].

1.5 Objectives and experimental approach

Malaria continues to be a serious and sometimes fatal disease, especially in low-income regions. WHO recommends the use of microscopy method or RDTs to confirm the diagnosis in case of suspected malaria. There is a great diversity of RDTs approved for malaria detection, mainly for *P. falciparum* detection since it is the most pathogenic[6]. The protein *Pf*HRPII, produced exclusively by *P. falciparum*, is mostly used as biomarker for malaria detection since is highly expressed in the human host. The RDTs are based on LFA, which have some limitations that can be overcome by improving the sensitivity. SERS-based LFAs can be a solution for this problem by using a Raman reporter with a known signal that enhanced the signal. Thus, in this work, a SERS-based LFA in sandwich format for malaria detection was attempted (Figure 1.5). The expression and purification of recombinant *Pf*HRPII, the development of SERS tags and their characterisation, and the optimisation of LFA were vital steps to perform before the malaria detection by SERS-based LFA.

The protein *Pf*HRPII was used as an analyte since is highly expressed during a malaria infection, which also can be easily produced at a larger scale in *E. coli* using a vector that overexpresses the protein containing an His-tag, allowing its purification using a Ni-NTA column (Figure 1.5b), as described in section 1.1.1.1.1. The purity and homogeneity of the purified protein was evaluated by sodium dodecyl sulphate-polyacrylamide gel electrophoresis (SDS-PAGE), western blotting, and protein concentration was determined by the bicinchoninic acid (BCA) assay.

To perform a non-competitive assay, also known as sandwich assay[75], the anti-*Pf*HRPII antibody was immobilised in the test line and used in the SERS tags. For colorimetric and SERS detection, SERS tags were developed using AuNSs coated with MBA and conjugated with this specific antibody. The functionalisation of AuNSs with a Raman reporter such as MBA is important as it allows to amplify the unique Raman vibrational fingerprint from MBA due to the strong electromagnetic fields at the particle surface that polarise the local volume around the NP. Additionally, MBA can simultaneously act as a coating layer. The AuNSs were synthesised by seeding-mediated growth, where AuNPs are the seeds used[62]. The conjugate pad of the LFA had the SERS tags incorporated (AuNSs-MBA-antibody), which capture the protein when is present in the sample, and it is captured

by the test line producing a coloured line (Figure 1.5a). The control line has the anti-IgG immobilised to capture the antibody present in the SERS tags when the LFA is valid.

Previously, a several LFA optimisations regarding the components and the concentrations of the reagents were performed with an enzyme Perox, which the system Perox-anti-Perox can correlate to recombinant *Pf*HRPII-anti-*Pf*HRPII.

In case of a positive sample in a LFA sandwich assay, two coloured lines appears in the test and control lines[75]. Conversely, in case of a negative sample, only one coloured line appears, which corresponds to the control line. After the optimisations, the LFA was ran for the detection of *Pf*HRPII, where SERS signals of the test lines of a positive and negative sample were compared (Figure 1.5c).

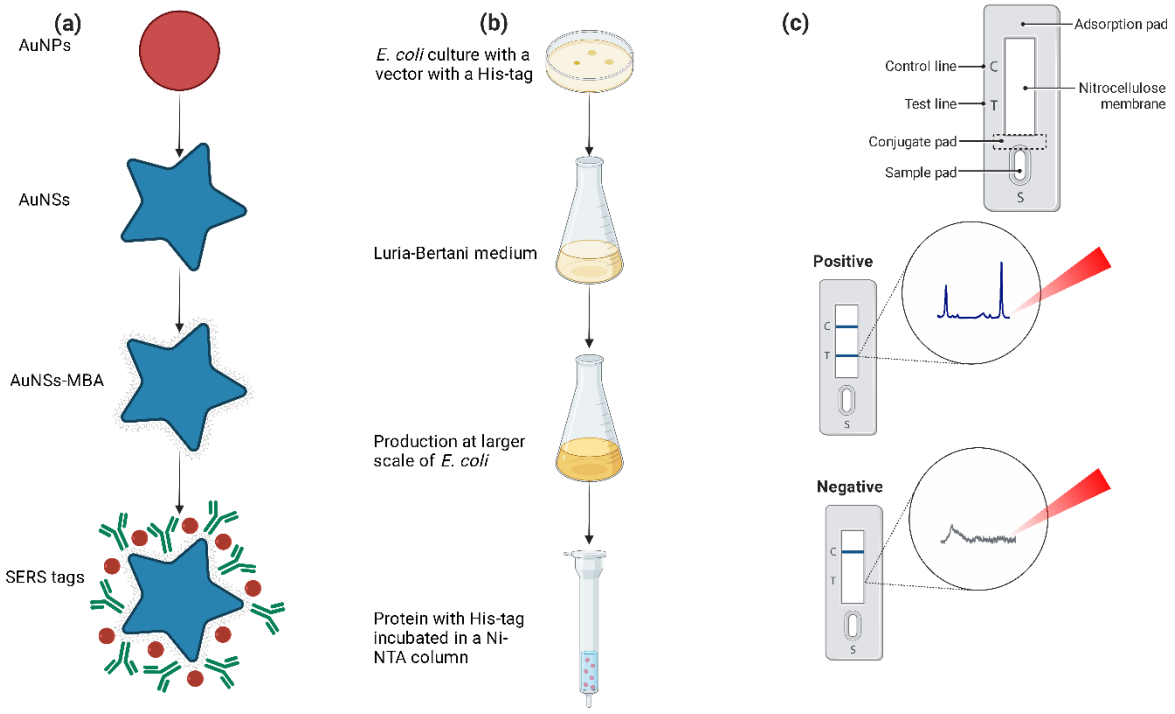

Figure 1.5: Representation of the three main experimental approaches for the development of a SERS-based sandwich LFA for detection of *Pf*HRPII. (a) Top to bottom: Through a seeding-mediated growth, AuNSs were synthesised by using AuNPs as seeds. Synthesised AuNSs were functionalised with MBA and conjugated with a specific antibody. (b) Top to bottom: An *E. coli* culture overexpressing recombinant *Pf*HRPII containing an His-tag was used, allowing protein purification by a Ni-NTA column. (c) By using all of components (top) and after the optimisations involved, the LFA was constructed to *Pf*HRPII detection, and the Raman spectra of the test lines of a positive and negative sample were compared (designed with BioRender).

2

MATERIAL AND METHODS

2.1 Materials

The following reagents were used for the expression of recombinant *Pf*HRPII: yeast extract, tryptone, ampicillin sodium salt and magnesium sulphate 7-hydrate ($MgSO_4$), which were purchased from Panreac AppliChem, Gatersleben, Germany. Protease inhibitors (mini EDTA-free) and DNase I were both purchased from Roche, Switzerland. It was also used sodium chloride (NaCl, Scharlau, Spain), Luria-Bertani agar (Merck, Germany), and isopropyl β-d-1-thiogalactopyranoside (IPTG, NZYTech, Portugal). The purification of this protein was performed using a nickel-nitrilotriacetic acid column (Ni-NTA Agarose) from Qiagen, Hilden, Germany. The buffers potassium phosphate buffer dibasic (≥ 98%) and monobasic (≥ 99%), were both purchased from Sigma-Aldrich, St. Louis, MO, USA. Imidazole (99%) was from Alfa Aesar – Thermo Fisher Scientific, Waltham, USA, sodium hydroxide from AkzoNobel, Eka Chemicals, Portugal and ethanol absolute was purchased from Carlo Erba Reagents, Val de Reuil, France.

The following reagents were used for SDS-PAGE and immunoblot: ammonium persulphate (APS, ≥ 98%), β-mercaptoethanol (≥ 99%), glycine (≥ 99%), brilliant blue R-250, skim milk powder, phosphate-buffered saline (PBS), tween 20, 3,3',5,5'-tetramethylbenzidine (TMB, ≥ 99%), anti-mouse IgG (whole molecule) – peroxidase (produced in rabbit), dimethyl sulfoxide (DMSO), sodium phosphate dibasic dihydrate and citric acid monohydrate, were all purchased from Sigma-Aldrich, St. Louis, MO, USA. It was also used sodium dodecyl sulphate (SDS), glycerol, bromophenol blue and hydrogen peroxide (H_2O_2, 30%), all purchased from Panreac AppliChem, Gatersleben, Germany. The reagents purchased from NZYTech, Portugal, molecular weight (MW) marker (NZYColour Protein Marker I) and Ponceau S (0.5% (w/v) Ponceau S in 1% (v/v) acetic acid) were also used. Glacial acetic acid, methanol, and tris (tris(hydroxymethyl)-aminomethane, ≥ 99.5%) were purchased from Carlo Erba Reagents, Val de Reuil, France, and acrylamide/bis-acrylamide from Bio-Rad, Portugal, tetramethylethylenediamine (TEMED, 99%, Amresco, VWR, Radnor, PA, USA). The mouse monoclonal malaria anti-*Pf*HRPII antibody was from Meridian Life Science, Luckenwalde, Germany. The anti-Mouse - IgG - peroxidase antibody produced in rabbit was purchased from Sigma-Aldrich, St. Louis, MO, USA. Isopropyl alcohol (≥ 99.8%) and hydrochloric acid were both purchased from Honeywell Fluka – Thermo Fisher Scientific, Waltham, USA.

The protein bovine serum albumin (BSA, ≥ 98%) was used in the BCA assay, with de BCA solution and copper (II) sulphate solution, all purchased from Sigma-Aldrich, St. Louis, MO, USA.

The synthesis of AuNPs and AuNSs, and their functionalisation, were made using the following reagents: nitric acid (65%, purchased from Panreac AppliChem, Gatersleben, Germany), ascorbic acid (purchased from Carlo Erba Reagents, Val de Reuil, France), sodium citrate tribasic dihydrate (≥

99%), $HAuCl_4$ solution (30 wt. % Au (III) chloride in dilute HCl), silver nitrate (≥ 99.8%) and MBA (99%), all purchased from Sigma-Aldrich, St. Louis, MO, USA.

The electrophoresis was prepared with UltraPure™ agarose purchased from Invitrogen, Thermo Fisher Scientific, Waltham, USA.

The reagents used in the bioconjugate assay 1-ethyl-3-(3-(dimethylamino)propyl)carbodiimide (EDC) and N-hydroxysulfosuccinimide (SNHS, ≥ 98%), the buffer 2-ethanesulfonic acid (MES, 99%) and the enzyme Perox, were all purchased from Sigma-Aldrich, St. Louis, MO, USA. The substrate 2,2'-azino-bis(3-ethylbenzthiazoline-6-sulfonic acid) (ABTS, > 98%) was used in the enzymatic assay, and was purchased from Roche, Switzerland. The antibody anti-horseradish peroxidase (anti-Perox) and the secondary antibody anti-IgG (ImmunoPure™ Mouse IgG, Whole Molecule) were purchased from Antibodies-Online, Germany and Thermo Fisher Scientific, Waltham, USA, respectively.

It was also used sucrose for the pre-treatment of the conjugate pad in the LFA assay, purchased from Sigma-Aldrich, St. Louis, MO, USA.

The equipment used during these experiments it is in a table in the annex I (Table I. 1).

2.2 Methods

2.2.1 Recombinant *Pf*HRPII expression in *E. coli*

The expression of the recombinant *Pf*HRPII was based on the method described by Ndonwi *et al.*[18]. *E. coli* BL 21/DE3 was the host cell, in which *Pf*HRPII was constructed in pET-15b vector.

From a seed stock solution stored in a cryoprotective medium and maintained in a vial at -80ºC, was prepared 10 mL of Luria-Bertani medium (5 $g \cdot L^{-1}$ of yeast extract, Panreac AppliChem, Gatersleben, Germany, 10 $g \cdot L^{-1}$ of tryptone, Panreac AppliChem, Gatersleben, Germany, and 10 $g \cdot L^{-1}$ of sodium chloride, NaCl, Scharlau, Spain) with 50 $\mu g \cdot mL^{-1}$ of ampicillin (ampicillin sodium salt, Panreac AppliChem, Gatersleben, Germany). This culture was growth for 16 h at 37ºC, 220 rpm in an incubator (Gallenkamp Orbital Shaker Incubator, Cambridge, United Kingdom). Then, a serial dilution was performed by transferring 1 mL from this culture to a plate with 9 mL of Luria-Bertani medium, yielding a 10^{-1} dilution. It was performed this serial dilution until a 10^{-4} dilution solution. A volume of 100 µL of each dilution solution was inoculated into different Luria-Bertani agar (10 $g \cdot L^{-1}$ peptone from casein, 5 $g \cdot L^{-1}$ yeast extract, 10 $g \cdot L^{-1}$ sodium chloride, 12 $g \cdot L^{-1}$ agar-agar, Merck, Germany) plates and was incubated at 37ºC for 16 h.

An isolated colony was collected from the 10^{-4} plate and placed in 20 mL of Luria-Bertani medium with 50 $\mu g \cdot mL^{-1}$ of ampicillin, then was incubated at 37ºC, 220 rpm for 16 h. Afterwards, these 20 mL from the overnight culture was transferred to 2 L of Luria-Bertani medium, divided in four

Erlenmeyer. These flasks were incubated at 37ºC, 220 rpm until the measure of the absorbance at 600 nm, was less than 0.6. After lowering the temperature (≈ 20ºC) 0.5 mM of IPTG (NZYTech, Portugal) was added. Then, these flasks were incubated for 20 h at 180 rpm.

The culture inside in these four Erlenmeyer flasks, were centrifuged for 15 min, 3,951 *g* at 4ºC, in 0.5 L centrifuge tubes (Beckman Coulter, California, USA) in the Centrifuge Beckman Coulter Avanti J26-XPI (California, USA) with a JA-10 rotor. The *pellets* were resuspended in a wash buffer (50 mM monobasic potassium phosphate buffer (≥ 99%) and dibasic potassium phosphate buffer (≥ 98%) at pH 7.5, Sigma-Aldrich, St. Louis, MO, USA, 30 mM NaCl, 30 mM imidazole, 99%, Alfa Aesar – Thermo Fisher Scientific, Waltham, USA) and stored at -20ºC until further use.

After thawing the suspension, 1 tablet per 10 mL of protease inhibitors (Mini EDTA-free, Roche, Switzerland), 50 µL of DNase I 5 $mg \cdot mL^{-1}$ (Roche, Switzerland) and magnesium sulfate 7-hydrate (Panreac AppliChem, Gatersleben, Germany) with a final concentration of 50 mM were added to the solution. Then, this solution was subjected to French Press at 20,000 psi (French pressure cell press, Thermo Electron Corporation – Thermo Fisher Scientific, Waltham, USA) for three times. Afterwards, the solution was centrifuged at 45,000 rpm for 1 h at 4ºC, in an ultracentrifuge (Beckman Optima LE-80K, California, USA). The supernatant was collected, and the *pellet* was discarded.

2.2.2 Recombinant *Pf*HRPII purification with a Ni-NTA column

For the purification process, 7 mL of Ni-NTA Agarose (Qiagen, Hilden, Germany) was pre-charged with nickel metal ions (see section A.1 in appendix A). The first step for purification of a protein is to equilibrate the column by adding two volumes of column wash buffer (50 mM potassium phosphate buffer at pH 7.5, 500 mM NaCl, 30 mM imidazole) and mixing the column as it seen in the Figure 2.1. This step was repeated four times. A solution of 500 mM NaCl was used to remove non-specific interaction of contaminant proteins with the resin, and 30 mM of imidazole was used to remove proteins that bind less strongly to the resin[25].

Afterwards, the supernatant from the expression of the recombinant protein (see section 2.2.1 in Material and Methods) was introduced into the chromatography column, and the column was incubated for 30 min after mixing. The column was then washed with the wash buffer with two volumes until the observed absorbance was below than 0.1 at 280 nm. This guaranteed that most of all proteins with nonspecific interactions had been washed from the resin.

Subsequently, the protein was eluted by adding one volume of column elution buffer (50 mM potassium phosphate buffer at pH 7.5, 30 mM NaCl, 500 mM imidazole) and incubated for 10 min, whereby imidazole competes with tagged proteins for binding sites on the Ni-NTA resin. This step was repeated until the observed absorbance was below than 0.1 at 280 nm.

All the flow through from the column was collected for further analysis. The elution was concentrated using protein concentrators (Amicon Ultra-4 Centrifugal Filter Units, 30k, 4 mL, Merck Milipore, Cork, Ireland) and resuspended in potassium phosphate buffer pH 7.5, at 1 mM.

The concentrated protein was aliquoted in cryovials and stored in liquid nitrogen until further use. Later, SDS-PAGE, western blot and the BCA assay were performed to assess the quality of the purification product, identify the protein, and determine their total concentration.

When the purification process was completed, the column was washed with 500 mL of sodium hydroxide (AkzoNobel, Eka Chemicals, Portugal) at 0.5 M and stored in 30% ethanol (ethanol absolute, Carlo Erba Reagents, Val de Reuil, France) at 4ºC, to remove residuals on the resin and inhibit microbial growth.

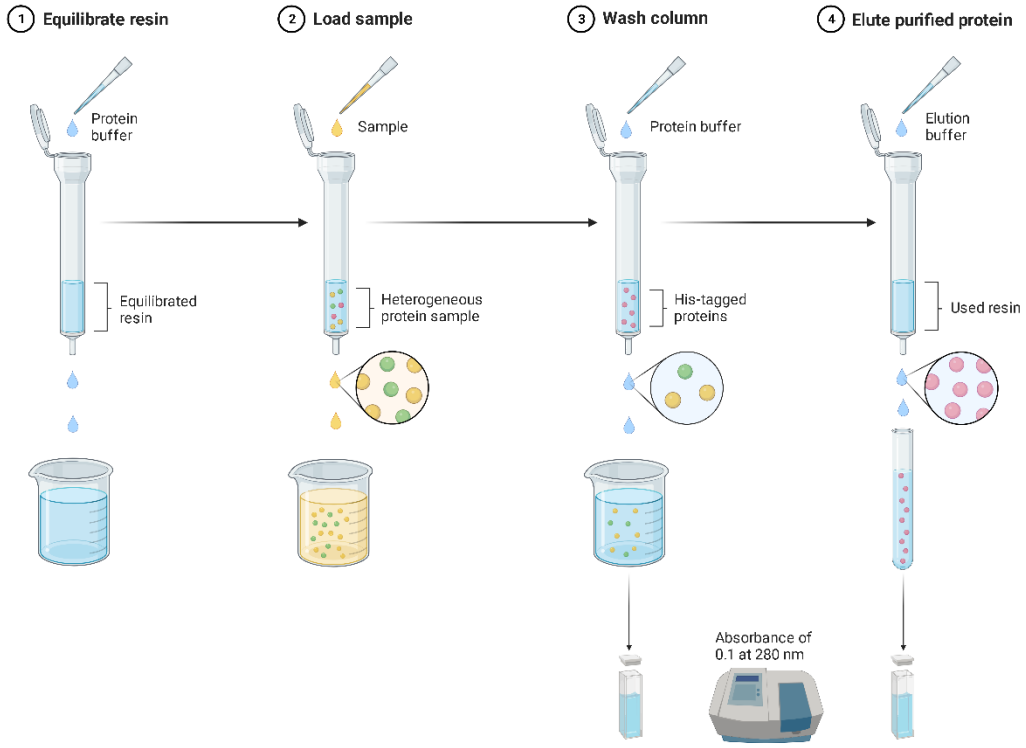

Figure 2.1: Scheme of the typical procedure used for the purification process. 1, in the first step the Ni-NTA column was equilibrated by adding wash buffer. 2, the supernatant from the expression of the recombinant protein was added to the column and was incubated for 30 min after mixing. 3, the column was washed with wash buffer until the absorbance was below 0.1 at 280 nm. 4, elution buffer was added to the column and incubated for 10 min, repeatedly until the absorbance was below 0.1 at 280 nm (designed with BioRender).

2.2.3 Sodium dodecyl sulphate-polyacrylamide gel electrophoresis

Before performing this technique, all the material was cleaned with ultrapure water (H_2O, 18 MΩ·cm at 25ºC) and the glass plates were cleaned with ethanol 70% (w/v), so all could be clean and free of dust.

The two glass plates (1 spacer and 1 short glass plate) were put in position and water was used for leak check. Then, the water was removed, and the resolving gel solution was added in the space between the plates. The resolving gel at 12% of acrylamide is prepared by combining a buffer solution (1.5 M Tris-HCl at pH 8.8, Tris(hydroxymethyl)-aminomethane, ≥ 99.5%, Carlo Erba Reagents, Val de Reuil, France, hydrochloric acid, Honeywell Fluka – Thermo Fisher Scientific, Waltham, USA), a solution of acrylamide/bis-acrylamide (37.5:1) (Bio-Rad, Portugal), SDS (10% w/v, Panreac AppliChem, Gatersleben, Germany), ultrapure water, APS (10% w/v, ≥ 98%, Sigma-Aldrich, St. Louis, MO, USA) and TEMED (99%, Amresco, VWR, Radnor, PA, USA). APS and TEMED were added right before adding this solution in the glass plates. Immediately, the solution was overlaid with isopropyl alcohol (≥ 99.8%, Honeywell Fluka – Thermo Fisher Scientific, Waltham, USA). After 15-30 min the polymerisation reaction was finished.

Next, the isopropyl alcohol was removed, and the stacking gel solution was added. The stacking gel solution with 4% of acrylamide was prepare combining a buffer solution (0.5 M Tris-HCl, pH 6.8), a solution of acrylamide/bis-acrylamide (37.5:1), SDS (10% w/v), ultrapure water, APS (10% w/v) and TEMED. APS and TEMED were added right before adding this solution in the glass plates. Afterwards, the comb was placed between spacers. The polymerisation reaction was finished after 15-30 min.

All the samples were prepared by a mixture of 5 µL of sample and 5 µL of sample buffer. The sample buffer is prepared by combining a stacking gel solution, SDS (10% w/v), β-mercaptoethanol (≥ 99%, Sigma-Aldrich, St. Louis, MO, USA), glycerol (Panreac AppliChem, Gatersleben, Germany), bromophenol blue (0.5% w/v, Panreac AppliChem, Gatersleben, Germany) and ultrapure water. After this preparation, the samples were incubated at 95ºC for 5 min.

All the components for the electrophoresis were placed into the electrode assembly and the inner chamber was filled with a running buffer solution (Tris-glycine at pH 8.3 - glycine, ≥ 99%, Sigma-Aldrich, St. Louis, MO, USA). Then, 10 µL of each sample were loaded into the gel and 2 µL of a molecular weight (MW) marker (NZYColour Protein Marker I, NZYtech, Portugal). The electrophoresis was performed at constant voltage (90 V) for 120 min. After this process, the gel was washed with ultrapure and placed into the staining solution Coomassie Brilliant Blue R-250 (0.1% Brilliant Blue R-250, Sigma-Aldrich, St. Louis, MO, USA, 5% glacial acetic acid, Carlo Erba Reagents, Val de Reuil, France, and 30% methanol, Carlo Erba Reagents, Val de Reuil, France) for at least 1 h in the

rocking shaker (mini-rocking shaker, Biosan, Latvia). Afterwards, the staining solution was removed and added the destaining solution (5% glacial acetic acid and 30% methanol). The destaining solution was changed periodically until the gel background was clear at continuous shake. The results were analysed using a gel MW analyser from the OriginPro2021 software.

2.2.4 Immunoidentification by western blot

The protein blotting to a polyvinylidene difluoride membrane (PVDF, Sigma-Aldrich, St. Louis, MO, USA) was done after a complete SDS-PAGE run, as we can see in the Figure 2.2. The gel was soaked for 15 min in a transfer buffer (Tris 25 mM, glycine 192 mM, methanol 20% v/v) to equilibrate, so that it removed contaminating electrophoresis buffer salts. The two fibre pads and two blotting papers were also soaked in the transfer buffer for 15 min. The PVDF membrane was wet in 100% methanol for 1 minute prior to equilibration in the transfer buffer. To prepare the gel and membrane sandwich, the gel holder cassette was placed with the cathode (black) side at the table and the fibre pad was placed at the top, followed by the blotting paper. Then, the gel was placed on top of it and the PVDF membrane was placed squarely at once into the gel, avoiding moving so it could not form air bubbles. A blotting paper and a wet fibre pad were placed on top of the PVDF membrane. Then, the gel holder was closed, locked, and inserted into the inner module with the black side of the cassette facing the black side of the blotting module. The inner module was placed into the electrophoresis chamber with a magnetic stir with an ice pack and filled with a transfer buffer. The gel and membrane sandwich were run at 100 V for 60 min in ice with continuous stirring. After the run, the membrane was removed from the gel holder cassette and washed with ultrapure water.

The PVDF membrane was then stained for 1 minute with Ponceau S (0.5% w/v Ponceau S in 1% v/v acetic acid, NZYTech, Portugal) to make the protein bands visible. Afterwards, the membrane was destained in ultrapure water until the background was clear. Then, the membrane was incubated for 60 min in skim milk powder (5% w/v, Sigma-Aldrich, St. Louis, MO, USA) in phosphate-buffered saline 1× (PBS, Sigma-Aldrich, St. Louis, MO, USA) and tween 20 0.1% (w/v) (Sigma-Aldrich, St. Louis, MO, USA) to block the membrane. The membrane was then washed three times with PBS-T (phosphate-buffered saline 1× and tween 20 0.1% w/v) for 5 min followed by washing with PBS at pH 7.4, 5 mM to remove the tween 20 from the membrane surface prior to blot development and imaging. The PVDF membrane was incubated overnight in primary antibody solution (from 1:2,000 to 1:100,000 with PBS-T with 1% skim milk powder) with gentle agitation at 4^{o}C. Subsequently, the membrane was again washed three times with PBS-T followed by one wash with PBS, 5 min per wash. The secondary antibody solution (anti-mouse IgG (whole molecule) – peroxidase (produced in rabbit), Sigma-Aldrich, St. Louis, MO, USA, 1:80,000 with PBS-T with 1% skim milk powder) was

added to the membrane for at least 3 h with gentle agitation. Afterwards, the membrane was washed three times with PBS-T for 5 min per wash and followed by PBS at pH 7.4, 5 mM wash.

If the purified protein present in the PVDF membrane is the intended, the antibody binds to the protein in the membrane, and the secondary antibody with a peroxidase coupled will bind to the primary antibody. This can be revealed with a colorimetric substrate such as TMB (≥ 99%, Sigma-Aldrich, St. Louis, MO, USA). Based in the Sigma-Aldrich Protocol[79], the TMB solution was prepared with DMSO (Sigma-Aldrich, St. Louis, MO, USA) at 1 $mg \cdot ml^{-1}$. This solution was diluted with 9 mL of phosphate citrate buffer (sodium phosphate dibasic dihydrate at 0.102 M, Sigma-Aldrich, St. Louis, MO, USA, and citric acid monohydrate at 0.05 M, Sigma-Aldrich, St. Louis, MO, USA) at 0.15 M, pH 5. Then, was added 2 µL of fresh hydrogen peroxide (30%, Panreac AppliChem, Gatersleben, Germany) immediately prior to use. The combination of Perox and H_2O_2 causes the oxidation of TMB, resulting the formation of a blue colour.

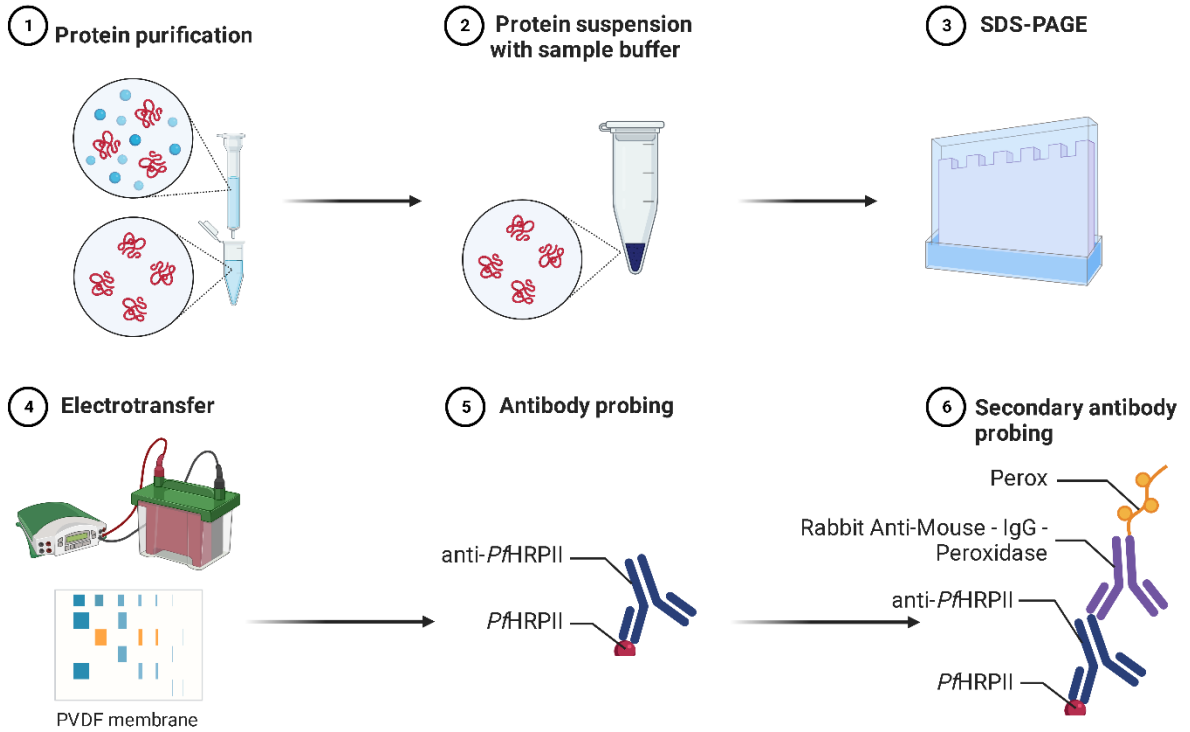

Figure 2.2: Procedure used for western blot analysis. The step 1 represents the purification described before. 2, a sample of the protein purified was suspended with sample before and placed in wells of a gel for performing an SGS-PAGE (3). 4, afterwards, the gel and PVDF membrane was run to perform an electrotransferase. 5, the antibody (anti-*Pf*HRPII) was incubated in the PVDF membrane to be captured by the antigen (*Pf*HRPII) present in this membrane. 6, a secondary antibody with a Perox accoupled was then incubated with the same membrane to be captured by the antibody (anti-*Pf*HRPII) (designed with BioRender).

2.2.5 Bicinchoninic acid assay for total protein determination

The BCA assay was based on the method described by Smith *et al.*[80], and is a biochemical assay for the colorimetric detection and quantification. This method is a combination of the reduction of Cu^{2+} to Cu^{+} by a protein in an alkaline environment (biuret reaction) and a colorimetric detection of the cuprous cation (Cu^{+}) using a reagent containing BCA. The total protein concentration is revealed by a colour change of the solution from green to an intense purple in proportion to protein concentration, which can provide a standard curve with reading the absorbance at 562 nm and quantification of an unknown protein[81].

For the standard curve was used a protein standard BSA (≥ 98%, Sigma-Aldrich, St. Louis, MO, USA) with a series of dilutions of known concentrations (0 to 17.5 $\mu g \cdot mL^{-1}$ range in 2.5 $\mu g \cdot mL^{-1}$ intervals). The working reagent was prepared by mixing 50 parts of BCA solution (Sigma-Aldrich, St. Louis, MO, USA) with 1 part of copper (II) sulphate solution (Sigma-Aldrich, St. Louis, MO, USA). The unknown concentration samples were prepared with different dilutions (1:10 and 1:20).

A volume of 50 µL of each solution (standard and unknown) were added in each tube with 950 µL of working reagent and vortex. These solutions were then incubated accordingly with enhanced protocol at 60ºC for 30 min (working range of 5 to 250 $\mu g \cdot mL^{-1}$) or with the standard protocol at 37ºC for 30 min (working range of 20 to 2,000 $\mu g \cdot mL^{-1}$)[81]. The samples were cool down to room temperature for 10 min. Afterwards, absorbance at 562 nm was measured of all the solutions. Through the plotting BSA standard *vs* its concentration in $\mu g \cdot mL^{-1}$ it was determined the protein concentration of each unknown sample.

2.2.6 Spherical gold nanoparticle synthesis

Throughout the experiments, all glassware and magnetic stirrer used were previously washed with *aqua regia*, a 1:3 mixture of concentrated nitric acid (65%, Panreac AppliChem, Gatersleben, Germany) and hydrochloric acid (Honeywell Fluka – Thermo Fisher Scientific, Waltham, USA). This mixture allows dissolution of noble metals and other inert metals contained, that avoid the occurrence of aggregation or contamination[82]. Then, these materials were vigorously washed with ultrapure water. The pH was monitored and a pH 7 was established.

The method used is an alternative to the conventional synthesis process by Turkevich[83], proposed by Ojea-Jiménez *et al.*[61] that allows an improved size distribution and an uniform spherical shape of AuNPs. A volume of 98 mL of ultrapure water was added to an Erlenmeyer flask and put under heating and stirring (≈ 700 rpm) using a magnetic stirrer under reflux to maintain total reaction volume and concentration. The volume of 2 mL of trisodium citrate (≥ 99%, 343 mM, Sigma-Aldrich, St. Louis, MO, USA) was added to the flask and kept away from sunlight with aluminium foil. After

bringing this solution to boiling, 69.2 µL of a 1.445 M $HAuCl_4$ solution (30 wt. % Au (III) chloride in dilute HCl, Sigma-Aldrich, St. Louis, MO, USA) were added to start the gold reduction reaction. After 5 min, the heating, reflux and stirring were stopped so that the reaction could stop, and then was cooled to room temperature. Afterwards, the AuNPs solution was filtered by a 0.20 µm syringe filter (GVS North America, Sandford, USA) and store at 4ºC kept away from sunlight.

2.2.6.1 AuNPs UV-Vis spectroscopy characterisation

The characterisation of AuNPs was through ultraviolet-visible spectra (UV-Vis spectrophotometer Cary 50 Bio, Varian®, San Francisco, CA, USA), which were performed using quartz cells with 1 cm length (Hellma®, Müllheim, Germany), in a range 200 to 800 nm in a UV-Vis spectrophotometer. According to the correlation between the AuNPs diameter and the extinction coefficient ($\varepsilon_{450\,nm}$) established by Haiss *el al.*[84], the diameter and concentration of the NPs were determined. This characterisation allows us to analyse the LSPR band of AuNPs, the colloidal stability, degree of monodispersivity and average size and concentration of AuNPs[84].

For NPs with 5 to 100 nm diameter, it is possible to determine their diameter with the ratio between the absorbance of the maximum LSPR (A_{LSPR}) and the absorbance at 450 nm (A_{450}) (Equation 2.1):

$$diameter(y) = 0.112e^{2.998\times\left(\frac{A_{LSPR}}{A_{450}}=x\right)} \qquad \text{Equation 2.1}$$

With the average diameter of the AuNPs, extinction molar coefficient is determined according to the function between the logarithms of diameter values and the logarithms of extinction molar coefficient (Equation 2.2):

$$ln\,\varepsilon_{450\,nm}(y) = 3.0869 \times ln\,diameter(x) + 10.869 \qquad \text{Equation 2.2}$$

Through the Lambert-Beer law[85], the final concentration of the NPs solution (C) can be calculated (Equation 2.3):

$$C = \frac{A_{450\,nm}\times 1\times Dilution\ Factor}{\varepsilon_{450\,nm}} \qquad \text{Equation 2.3}$$

After the characterisation of the colloidal solution, the AuNPs solution was transferred to a flask covered with aluminium foil and stored in the dark at 4ºC until further use.

2.2.7 Star-shaped gold nanoparticles synthesis

A seed-mediated growth method adapted from Yuan *et al.*[66] was used to synthesised AuNSs, where the suspension of AuNPs was used as seeds. At this seed suspension of AuNPs in the volume of 7.5 mL at 2 nM and 15.5 µL of $HAuCl_4$ at 1.455 mM were added. Quickly, 450 µL of a 4 mM silver nitrate (≥ 99.8%, Sigma-Aldrich, St. Louis, MO, USA) and 450 µL of a 100 mM ascorbic acid (Carlo Erba Reagents, Val de Reuil, France) were simultaneously added. The solution was stirred for 30 seconds, and the colour rapidly turned from light red to greenish-black. Then, the solution was centrifuged at 2,500 *g* for 25 min at 10ºC (Centurion Scientific K3 Series centrifuge, North America by Core Life Sciences, USA). Immediately, the LSRP peak was observed by UV-Vis spectroscopy and the concentration of AuNSs was determined through the molar extinction coefficient[66].

2.2.8 Gold nanoparticles functionalisation

The NPs need to be functionalised with a capping agent, which functions as a capping agent and an intermediate for protein bioconjugation. In this case, MBA (99%, Sigma-Aldrich, St. Louis, MO, USA) was used since adsorbs strongly on Au substrates[86].

A suitable volume of the ethanolic solution of the capping agent at 10 mM was added to the AuNPs suspension to yield a molar ratio of 2,500 under vigorous stirring at 700 *g* for 15 min. After an overnight reaction to ensure a complete self-assembly monolayer formation, the excess of MBA was removed through centrifugation for 10 min at 11,200 *g*. To confirm a successful functionalisation and identify possible aggregation effects, a red shift of the LSPR peak was observed by UV-Vis spectroscopy. The functionalisation of AuNSs was performed similarly to the functionalisation of AuNPs except that the molar ratio used was 50,000. Both suspensions were stored at 4ºC until further use.

2.2.9 Colloidal stability of synthesized nanoparticles

Several AuNPs and AuNSs suspensions were prepared with different concentrations of NaCl, namely, 10 to 100 mM range in 10 mM intervals and 100 to 500 mM range in 100 mM intervals for both NPs types. For AuNSs, a smaller interval was included from 2 to 10 mM range in 0.2 mM intervals. These concentration ranges allowed to study the influence of ionic strength on the stability of NPs. The concentration of the AuNPs and AuNSs were kept constant at 2 nM and 0.2 nM, respectively. The UV-Vis spectrum of each sample was observed in a scan window of 300 to 800 nm, and this experiment was performed in three independent batches.

2.2.10 Star-shaped gold nanoparticles conjugation

2.2.10.1 Conjugation through physisorption

The AuNSs were bioconjugated with BSA or anti-Perox, and incubated overnight at 4ºC on aliquots of functionalised AuNSs at 0.2 nM. Afterwards, the samples were centrifuged at 1,000 *g* for 10 min, and the supernatant was removed, and the pellets were resuspended in potassium phosphate buffer at 1 mM. After this preparation, the electrophoretic mobility of the samples was verified and performed in an electrophoretic assay (see section 2.2.13 in Material and Methods).

2.2.10.1.1 With BSA and effect by varying the pH value

This study can show the influence of the pH and the maximum concentration of BSA on this conjugation. Several AuNSs-BSA bioconjugates were prepared with different pH values (5.5, 6.5 and 7.5) with potassium phosphate buffer at 1 mM and different final concentrations of BSA (from 0 to 1,500 molar ratio) and incubated overnight.

2.2.10.1.2 With anti-Perox

The AuNSs were bioconjugated with anti-Perox (Antibodies-Online, Germany) on aliquots of functionalised AuNSs at 0.2 nM. This antibody was used since it represents a generic IgG antibody. This study allows to determine the concentration present in the sample necessary to form a full corona at AuNSs-MBA surface. Several AuNSs-anti-Perox solutions were prepared with different final concentrations of anti-Perox (from 0 to 1,150 molar ratio).

2.2.10.2 Covalent conjugation

To simulate the sandwich immunoassay, the following samples were tested: anti-Perox, Perox (Sigma-Aldrich, St. Louis, MO, USA) and BSA, all conjugated with AuNSs functionalised with MBA and to what was added EDC (Sigma-Aldrich, St. Louis, MO, USA) and SNHS (≥ 98%, Sigma-Aldrich, St. Louis, MO, USA) at 1 mM with a molar ratio [EDC]:[SNHS] of 1:2, diluted in ultrapure water and MES (99%, Sigma-Aldrich, St. Louis, MO, USA), respectively. All the proteins were added with a molar ratio of 1:422 and incubated in an orbital shaker (Biosan TS-100, Latvia) for 90 min at 250 rpm and 25ºC. Then, the samples were centrifuged for 10 min at 4ºC and 2,500 *g* in all the conjugation steps to remove the excess of protein and the bioconjugates were resuspended in 5 mM potassium phosphate at pH 7.5.

2.2.11 Enzymatic activity assay of peroxidase

This enzymatic assay is used to determine if the anti-Perox antibodies binds to Perox antigens. Perox enzyme catalyse the oxidoreduction reaction between ABTS (Roche, Switzerland) and hydrogen peroxide (H_2O_2, 30%). The principle of this reaction is represented in the next equation (Equation 2.4):

$$H_2O_2 + ABTS \xrightarrow{Peroxidase} 2H_2O + oxidised\ ABTS \qquad \text{Equation 2.4}$$

This protocol is based on the Sigma-Aldrich Protocol[87]. The conditions of this reaction were at 25ºC and pH 5. The oxidation of ABTS was measured with the absorbance at 405 nm with a light path length of 1 cm.

For bioconjugates assay (see section 2.2.10.2 in Materials and Methods), it was prepared fresh 1 mL of 9.1 mM ABTS in 10 mM potassium phosphate buffer (monobasic, ≥ 99%, Sigma-Aldrich, St. Louis, MO, USA), pH 5 at 25ºC. A volume of 17 µL of sample and 34 µL of H_2O_2 (0.3% v/v) were added. Quickly, the absorbance was measured at 405 nm in every 10 s during 10 min.

The Perox activity was calculated with the next equation (Equation 2.5):

$$Units/mg_{solid} = \frac{(\Delta A_{405\,nm}/min\ (test) - \Delta A_{405\,nm}/min\ (blank)) \cdot V_{final} \cdot DF}{\varepsilon \cdot V_{Blank/Enzyme}} \qquad \text{Equation 2.5}$$

$\Delta A_{405\,nm}/min$ were calculated from the slope of the curve obtained using the maximum linear rate for both test and blank. The final volume (V_{final}) is in mL of the reaction and DF is the dilution factor of the enzyme. The millimolar extinction coefficient (Ɛ) of oxidized ABTS at $A_{405\,nm}$ is 36.8 $mM^{-1} \cdot cm^{-1}$ [87]. The volume of blank/enzyme ($V_{Blank/Enzyme}$) was 17 µL, as mentioned before.

2.2.12 Dynamic light scattering

The dynamic light scattering (DLS) is a technique that can determine the polydispersity and hydrodynamic diameter in colloidal suspension[88]. DLS measurements were performed in a SZ-100 Nanopartica series (Horiba, Japan) with a 4 mW He–Ne laser (532 nm) fixed at 90º scattering angle. Each sample had 60 µL from the bioconjugates that were transferred to a quartz cell with 3 mm pathlength (Hellma®, Müllheim, Germany) with a scattering angle of 90º. Each sample was measured three times at 25ºC.

2.2.13 Agarose Gel Electrophoresis

In all experiments, UltraPure™ Agarose (Invitrogen, Thermo Fisher Scientific, Waltham, USA) was used at 0.3% (w/v) in 1:8X Tris-acetate-EDTA (TAE) buffer (pH 8). This suspension was heated to ≈ 85ºC in constant stirring until the liquid became translucid. The liquid agarose was put in a gel tray (mini-sub cell GT or wide mini-sub cell GT, Bio-Rad, Portugal), with a tooth comb. Then, the gel was cool down until it solidifies, for 30 min at 4ºC. Afterwards, the solid agarose gel was placed in the chamber and immersed in the 1:8X TAE buffer.

The samples were incubated overnight at 4ºC and centrifuged at ≈ 9,500 *g* at 10ºC for 10 min. The supernatant was discarded and 10 µL of each sample was poured in the gel. The agarose gel electrophoresis (AGE) with a mini-sub cell GT was performed with a voltage of 150 V for at least 20 min. The AGE with a wide mini-sub cell GT had an execution with a voltage of 150 V for at least 40 min. The analysis was made using eReuss, a gel analysis application currently under development (freely available at https://github.com/lkrippahl/eReuss).

2.2.14 Lateral flow assay

A started kit from Advanced Microdevices, Ambala Cantt, India, was used for this assay. The kit offers two types of cellulose fibre absorbent pads with different thickness (AP-045 with 0.4 mm and AP-080 with 0.9 mm), three types of NMs with different protein binding capacities, two glass fibre sample pads (GFB-R4 without any specific pre-treatment and GFB-R7L pre-treated with buffers and detergents to prevent non-specific binding of sample components to the pad), and two conjugate pads (PT-R5, a polyester matrix without any specific pre-treatment, and PT-R7, pre-treated with buffers for uniform movement of gold nanoparticle conjugates). The type CNPF of NM is a low protein binding membrane with pore sizes of 8 (CNPF8) and 10 µm (CNPF10), the type CNPC is a high protein binding membrane with pore sizes of 12 (CNPC12) and 15 µm (CNPC15), and the type CNPH is the highest protein binding membrane with wicking times of 70 (CNPH70), 90 (CNPH90), 150 (CNPH150), and 200 s (CNPH200) (Figure 2.3). All the components were cut manually, namely absorbent pads into 3 × 0.5 cm, NM into 6 × 0.5 cm, sample pads into 3 × 0.5 cm and conjugate pad into 1 × 0.5 cm. The sample pad GFB-R7L and the conjugate pad PT-R7 was pre-selected because of the pre-treatment given previously by the supplier. The absorbent pad and the NM were tested and selected by visual inspection and with the use of analysis image software (ImageJ). An additional blocking step and the concentration of the AuNSs-MBA-EDC/SNHS-anti-Perox-BSA (hereafter referred as "SERS tags") (0.2 nM or 1 nM) were also tested. Several dilutions in the test (anti-Perox, 1:10 to 1:10,000) and control line (anti-IgG, 1:10 to 1:100) was also tested and selected.

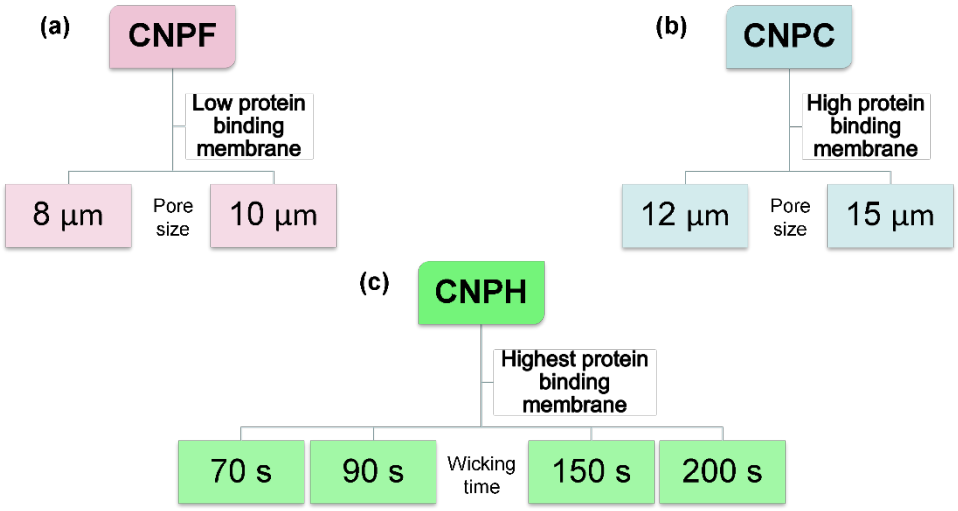

Figure 2.3: The started kit from Advanced Microdevices had three types of NM: low, high, and highest protein binding membrane. (a) The low protein binding membrane, CNPF, has two types of pore sizes (8 and 10 µm), (b) the high protein binding membrane, CNPC, with two types of pore sizes (12 and 15 µm), and the highest protein binding, CNPH, with four different wicking times (70, 90, 150, and 200 s).

2.2.14.1 Nitrocellulose membrane selection and blocking process

The control and test line were spotted manually by depositing 1 µL of 5 mg·mL^{-1} of anti-IgG (ImmunoPure™ Mouse IgG, Whole Molecule, Thermo Fisher Scientific, Waltham, USA) and 1 µL of 90 mg·mL^{-1} of anti-Perox (the same antibody present in the SERS tags) in the NM, respectively, both diluted 1:10 in Tris buffer (10 mM Tris-HCl, pH 7). The NM was then dried for at least 15 min at room temperature. A blocking process of the NM was performed by incubation with skim milk powder (2% w/v) with PBS-T (PBS 1:10, tween 20 at 0.05% w/v) for 30 min with gentle agitation, followed by three washes with PBS-T (PBS 1:10, tween 20 at 0.05% w/v) and one wash with PBS (1:10), 5 min per wash. Afterwards, the NM was incubated for at least 1 h with 400 µL of positive sample, in this case Perox at 10 mg·mL^{-1} diluted 1:100 in potassium phosphate buffer at 5 mM, pH 7.5. Then, the NM was incubated for 30 min with 400 µL of SERS tags at 1 nM. The AuNSs were synthesised as described before (see section 2.2.7 in Materials and Methods) and then the covalent conjugation (see section 2.2.10.2 in Materials and Methods) with the antibody, in this case anti-Perox, and with BSA was made prior of these simulations. In this experiment was used only the NM without any other variables. A simulation with the eight types of NM was performed similarly as described before.

With the NM selected, absorbent pad, conjugate pad, and sample pad were assembled as seen in the Figure 2.4. 15 µL of the SERS tags were deposited in the conjugate pad and dried for 2 h at room temperature or 60 min at 37ºC inside a desiccator (Vacuo-Temp, JP Selecta, Barcelona, Spain). An additional step of conjugate pad pre-treatment was tested, with PBS (1:10) containing 5% sucrose (Sigma-Aldrich, St. Louis, MO, USA), 1% BSA and 0.5% tween 20 and dried as described before.

Then, the sample pad was immersed into 200 µL of a positive sample, Perox, at 10 mg·mL^{-1} diluted 1:100 in potassium phosphate buffer at 5 mM, pH 7.5.

All the tests of LFA were selected by visually inspection and with the use of an image analysis software (ImageJ, National Institutes of Health, https://imagej.nih.gov/ij/), the images were taken after 30 min the addition of the sample.

2.2.14.2 Concentration of SERS tags selection

After selecting the NM and with or without a blocking process, a simulation was performed with the SERS tags at 0.2 and 1 nM. In both simulations, the covalent conjugation was made at 0.2 nM, and to use at 1 nM the SERS tags were concentrated five times. The control and test line were spotted manually with 1 µL in opposite sides in the NM, and after the LFA assembled with the NM selected with or without blocking process, 15 µL of the SERS tags at 0.2 and 1 nM were deposited in the conjugate pad and dried, as described before. Afterwards, the sample pad was immersed into 200 µL of a positive sample, Perox, at 10 mg·mL^{-1} diluted 1:100 in potassium phosphate buffer at 5 mM, pH 7.5. This incubation was taken place for 30 min and then the selection was performed as described before.

2.2.14.3 Absorbent pad selection

As described before in section 2.2.14.1 of Materials and Methods, this assay had a control and test line, Perox at 1:10, and 200 µL of the sample was incubated at 1:100 for 30 min. The absorbent pad selection (AP-045 and AP-080) was executed similarly to describe before in section 2.2.14.2 of Materials and Methods.

2.2.14.4 Control and test line dilution selection and sample dilution selection

Different dilutions in Tris buffer for the control line (anti-IgG at 5 mg·mL^{-1}), 1:10 to 1:100, and for the test line (anti-Perox at 90 mg·mL^{-1}), 1:10 to 1:10,000, were tested. As described before, the sample pad was immersed into 200 µL of the sample, Perox at 1:100 for 30 min at room temperature. After analysis of the images, the lowest dilutions that were visually at naked eye were used from now on. Then was tested several dilutions of the sample from 1:100 to 1:1,000,000 in 1:10 intervals. These analyses were made at naked eye and with the use of an image analysis software (ImageJ).

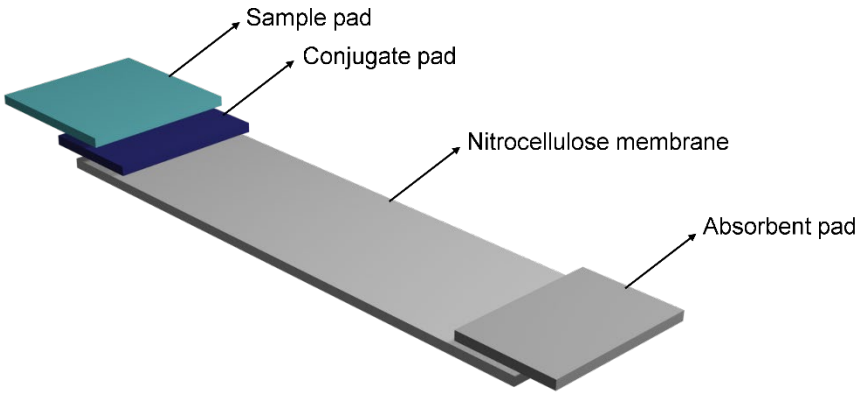

Figure 2.4: Representation of an LFA assembled, where the conjugate pad is in contact with the NM and the sample pad is in contact with the conjugate pad. The absorbent pad is in the other side in contact with the NM. The test line is placed next to the conjugate pad and the control line is placed on the other side (created in Blender).

2.2.15 Raman and SERS measurements

Raman measurements were performed using a Renishaw inVia Qontor micro-Raman spectrometer equipped with an air-cooled CCD as detector and a He–Ne laser operating at 32 mW of 632.81 nm laser excitation. In all different days, it was equilibrated using a Si wafer at 520.7 cm^{-1}. The samples were focused with a 50× Leica objective lens (N Plan EPI) of numerical aperture 0.12. A mapping was performed with 441 spectra with 0.1 s each, with limits of -10 µm per 10 µm and step of 1 µm. All the spectra were taken in triplicates at room temperature. All data were collected with Wire 5.0 software and later processing, such as noise reduction, subtract baseline and elimination of possible cosmic rays.

2.2.16 Statistical analysis

When it was possible, the experiments were run at triplicates. The results are present as mean ± standard deviation, except for the results from LFA experiments which are median ± standard deviation. For AGE and LFA results, was performed normality tests by Kolmogorov-Smirnov[89] test and Shapiro-Wilk[90] test and Grubbs[91] test for identification of outliers. For AGE, all the conjugations were compared by two-sample Student t-test, which gives the value of *p*-value, accordingly with Welch correction[92]. Afterwards, one-way analysis of variance (ANOVA)[93] and Turkey's multiple comparison[94] test were performed. For the LFA results, was applied two-sample Student t-test for comparison of the pixel at background and test line or control line.

3

RESULTS AND DISCUSSION

3.1 Recombinant *Pf*HRPII expression, purification, and characterisation

*Pf*HRPII was chosen as analyte for malaria detection in the SERS-based LFA system. *Pf*HRPII is a sensitive biomarker and its concentration can be correlated to disease severity, and prognosis. Thus, this protein was produced and characterised in the laboratory with the objective of using for subsequent assays. The recombinant protein was produced in *E. coli* BL 21/DE3 as the host cell, containing the pET-15b vector, in which the *Pf*HRPII sequence had been cloned, with a His-tag added to its N-terminus[18]. The recombinant *Pf*HRPII was then purified from the bacterial extract, using a chromatography column loaded with Ni-NTA agarose. This resin is very stable and has a very high affinity with His-tags located at either the amino or carboxyl terminal of the protein of interest[25]. Because of this affinity, contaminants can be easily washed away under harsh conditions, not affecting the binding of *Pf*HRPII, which can be successfully purified even if the protein is expressed at low levels[25]. The bounded protein in the Ni-NTA resin was eluted by competition with imidazole[22].

To verify if the protein expressed was in fact *Pf*HRPII, and if the concentration obtained was enough for the subsequent assays, BCA assay, SDS-PAGE and western blot were performed. Previously to perform western blot with the sample derived from expression and purification of recombinant *Pf*HRPII, a model protein, horseradish peroxidase (Perox) was used to optimise the conditions required for this protocol.

3.1.1 Western blot optimisation with Horseradish peroxidase

Horseradish peroxidase (Perox) is an enzyme widely used in biochemistry since it catalyses the conversion of several substrates into coloured products and thus, was chosen to optimise the conditions of the western blot[95]. An SDS-PAGE was completed to confirm the purity and molecular weight (MW) of purchased enzyme.

The SDS-PAGE stained with Coomassie Brilliante Blue R-250 analysis gives the MW of the Perox through a calibration curve that correlates the MW of the marker with the relative migration of the proteins inside the gel. From the obtained results, it was determined that Perox has a MW of 43.4 kDa (Figure 3.1). It has been reported that the MW of Perox is between 40 and 45 kDa[96], and 40 kDa by the supplier (Sigma-Aldrich, St. Louis, MO, USA), which confirms the SDS-PAGE results.

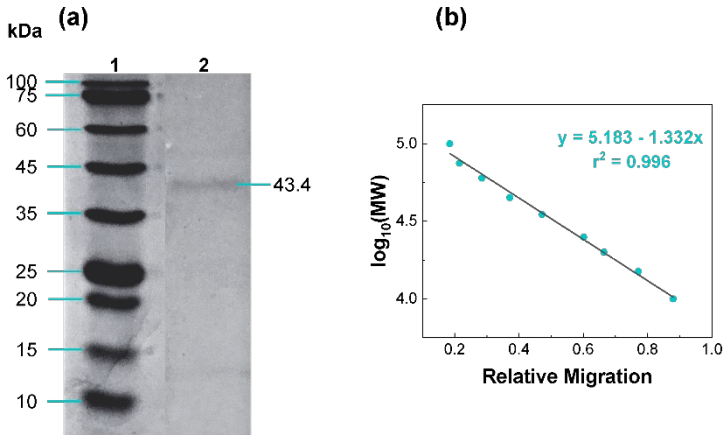

Figure 3.1: Analysis of the Perox enzyme. (a) SDS-PAGE, 4-12% gradient gels. Lane 1, MW marker. Lane 2, Perox. (b) Calibration curve of logarithm of MW - log (MW) - *vs* relative migration in the SDS-PAGE.

The western blot is a procedure that transfers proteins from an SDS-PAGE gel to a protein-adsorbent membrane, such as PVDF membrane, which is used to identify the proteins[97]. This membrane is incubated with labelled secondary antibodies to bind to the protein of interest, which is bound to the membrane. One of the most common strategies of labelling of the secondary antibody is using a peroxidase enzyme and a substrate, which their oxidation results in a change of colour revealing the protein bounded to the antibody. Only the bands that the primary antibody recognises are visible in the end, proving the identification of the protein of interest. Among of multiples advantages, the accessibility of different ligands to the protein immobilised and high protein binding capacity are the most important for this analysis[98]. Thus, a similar SDS-PAGE without any staining was performed and transferred to a PVDF membrane. After the transfer, the PVDF membrane was blocked with skim milk powder to prevent non-specific binding of contaminating proteins[98]. Then, the membrane was incubated with the primary antibody, in this case anti-Perox, followed by the secondary antibody coupled with a Perox (anti-mouse IgG-Peroxidase antibody), both diluted with PBS-T with 1% (w/v) skim milk to prevent further non-specific binding[97]. Between these incubations, the PVDF membrane was washed with PBS-T and PBS to remove the electrostatically bound and the unbound antibody molecules allowing to minimise the background[97]. Perox substrate (TMB) then added with H_2O_2 and allowed to react. The presence of the Perox from the secondary antibody catalyses the reaction resulting in the formation of a blue colour line. The blue line in the PVDF membrane is indicative that the protein in the SDS-PAGE gel was indeed the Perox enzyme. Several of optimisations regarding the Perox and primary antibody concentrations were made to determine the amount needed for a reliable detection in the PVDF membrane (Figure 3.2b and c). For all these conditions, the secondary antibody concentration used was 0.125 $\mu g \cdot mL^{-1}$.

As seen in the Figure 3.2b, a concentration range of Perox from 2 to 2,000 µg·mL^{-1} was incubated with a solution of anti-Perox at 45 µg·mL^{-1} in a PVDF membrane. Perox with concentrations lower than 20 µg·mL^{-1} did not exhibit colour indicating that the oxidation of TMB by Perox from the secondary antibody did not occur. For this reason, 20 µg·mL^{-1} was selected as the minimum concentration for a reliable detection. Several dilutions of anti-Perox (18 to 0.09 µg·mL^{-1}) in a PVDF membrane were tested using Perox at 20 µg·mL^{-1}. The concentrations 18 and 6 µg·mL^{-1} produced a blue colour in the PVDF membrane, which proofs that these dilutions were suitable for Perox detection, as seen in the Figure 3.2c.

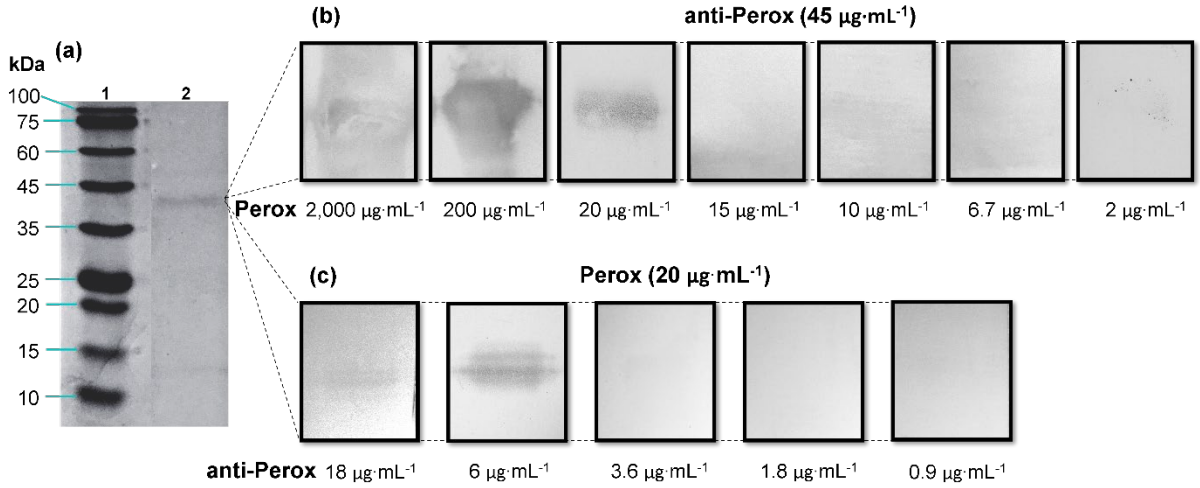

Figure 3.2: Analysis of the Perox. (a) SDS-PAGE. Lane 1, MW marker. Lane 2, Perox. (b) Western blot, varying concentrations of Perox, between 2 µg·mL^{-1} and 2,000 µg·mL^{-1}, in a PVDF membrane, all incubated with anti-Perox solution at 45 µg·mL^{-1}. (c) Western blot, several dilutions of primary antibody, anti-Perox (18 to 0.09 µg·mL^{-1}), used to incubate a PVDF membrane with Perox at 20 µg·mL^{-1}. In all tests anti-IgG coupled with Perox enzyme were used at 0.125 µg·mL^{-1}.

As a result of these optimisations, Perox at 20 µg·mL^{-1} conjugated with the respective primary antibody at 6 µg·mL^{-1}, and the secondary antibody at 0.125 µg·mL^{-1}, were considered ideal for Perox detection. These concentrations were then used for recombinant *Pf*HRPII detection by western blot.

3.1.2 Recombinant *Pf*HRPII characterisation

After the expression of the recombinant *Pf*HRPII in *E. coli* (DE3), the supernatant from this production was purified with a Ni-NTA column. All the fractions from column washing and elution of the protein, were collected and analysed.

As we can see in the Figure 3.3 in lane 2, the flow through of the supernatant of the recombinant *Pf*HRPII expression has proteins and products resultant of the expression by *E. coli* that did not interact with the Ni-NTA column. Most of the contaminants were washed away in the first step using

a washing buffer, containing low concentration of imidazole which can be later increased to elute the protein from the column[25] (Figure 3.3, lane 3). The washing process was monitored by measuring the absorbance at 280 nm and continued, since proteins absorb light at this wavelength, until was below 0.1 (Figure 3.3, lanes 4 and 5).

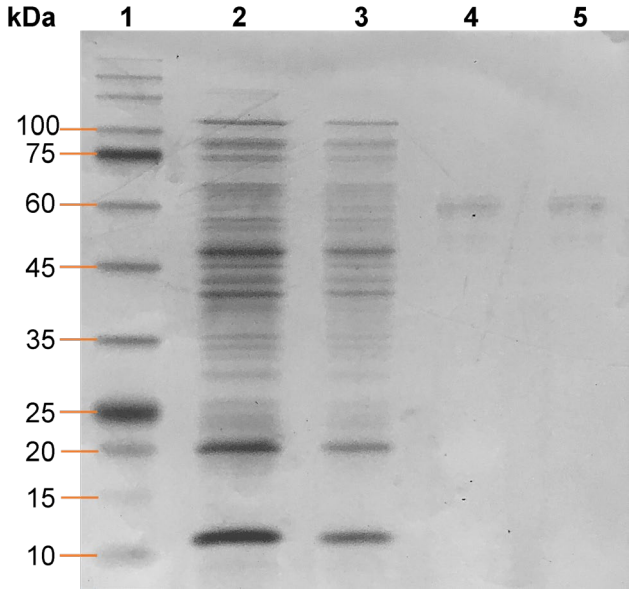

Figure 3.3: Analysis of the fractions collected from the Ni-NTA column. SDS-PAGE. Lane 1, MW marker. Lane 2, flow through of the supernatant of recombinant *Pf*HRPII expression. Lane 3, first step of washing the column. Lane 4 and 5, last steps of washing. The washing step continued until absorbance at 280 nm was below 0.1.

As it can be concluded from the calibration curve on Figure 3.4b, a MW of 67 and 22 kDa was obtained. A similar value to the MW value (around 50 kDa) described by the author which supplied us the overexpression vector (Professor Daniel E. Goldberg (Washington University, USA))[18]. Some authors have reported different MW values, between 60 and 105 kDa, with different possible explanations. Rock *et al.*[99] show this difference with several samples from parasites with different geographic origins[99]. Post-translational changes can also explain this difference, wherein galactose attached to the protein during or just before their release from infected erythrocytes, might change their apparent MW[13,100]. Some anomalous migration during the SDS-PAGE can also explain this difference, a problem observed in other malaric proteins with tandem repeats, due to low binding between SDS and the protein[100]. Ndonwi *et al.*[18] gives the possibility of the unusual amino acid content in the protein[18]. Substitution of glutamine for histidine may occur during an overexpression in *E. coli*, which does not increase greatly the MW, but can explain some differences obtained by other authors[101].

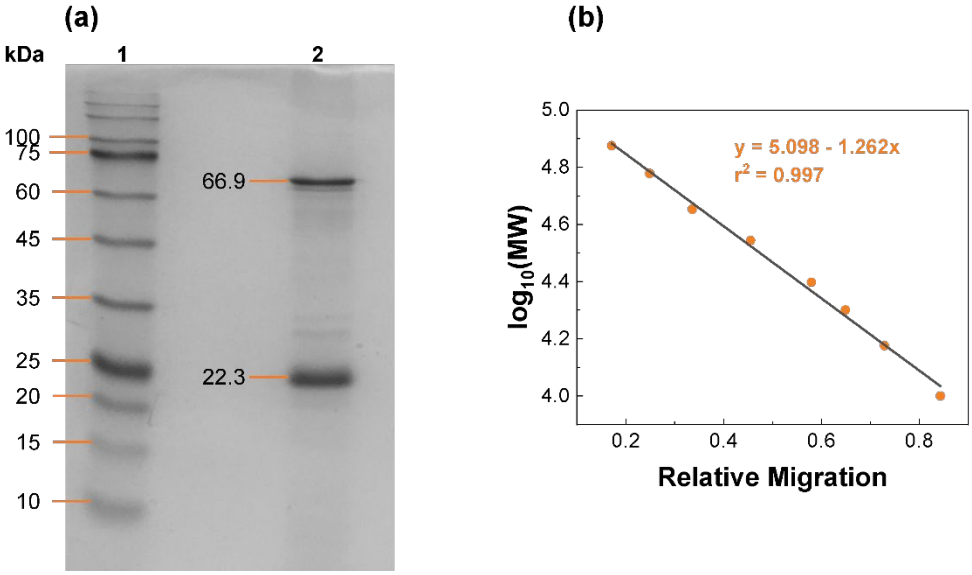

Figure 3.4: Analysis of the protein recombinant *Pf*HRPII. (a) SDS-PAGE. Lane 1, MW marker. Lane 2, recombinant *Pf*HRPII. (b) Calibration curve of logarithm of MW – log (MW) – *vs* relative migration in SDS-PAGE gel.

A western blot protocol similar to the one described previous section 3.1.1 was followed: an SDS-PAGE was performed to transfer the protein to a PVDF membrane, followed by incubation with the antibody against recombinant *Pf*HRPII, incubation with the secondary antibody with a coupled Perox. TMB was used as the substrate and H_2O_2 was added.

As it is shown in Figure 3.5, the recombinant *Pf*HRPII with a MW of 67 kDa was bound by the respective antibody, as anti-*Pf*HRPII at 0.6 $\mu g \cdot mL^{-1}$ conjugated with the secondary antibody at 0.125 $\mu g \cdot mL^{-1}$ recognised the latter. The blue stain that appears in the PVDF membrane, proved that the expressed and purified protein is indeed recombinant *Pf*HRPII. A second band appears in the SDS-PAGE with a MW of 22 kDa. This band could not be detected in the western blot, which allows to conclude that the antibody did not recognise this band as *Pf*HRPII. This is an indication that this band is a possible contaminant coeluted that have some affinity to the Ni-NTA resin from the *E. coli* expression[23,102] and is not a proteolysis product of the recombinant *Pf*HRPII. These optimisations had the purpose to reduce the costs of the western blot, although other authors has been used *Pf*HRPII and anti-*Pf*HRPII with higher concentrations[14].

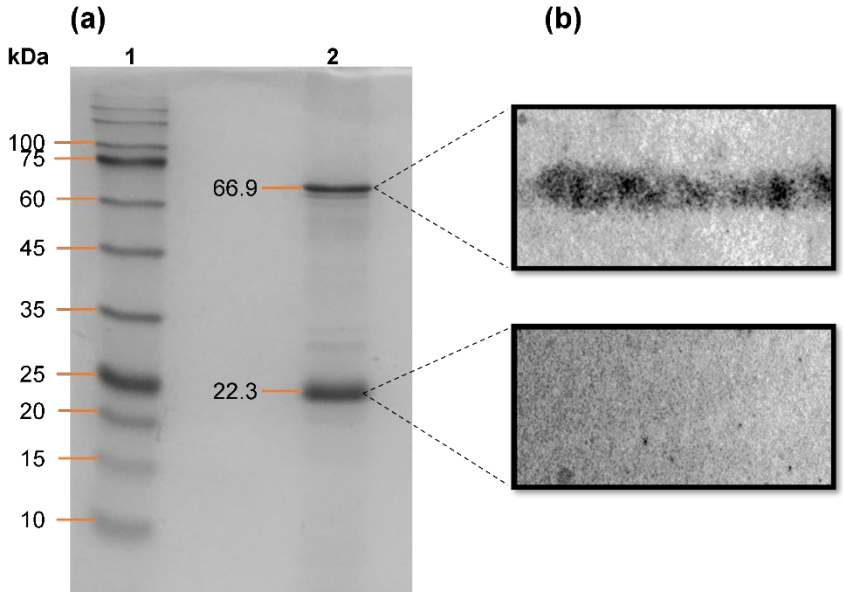

Figure 3.5: Analysis of the recombinant *Pf*HRPII protein. (a) SDS-PAGE. Lane 1, MW marker, where the values are present on the left. Lane 2, recombinant *Pf*HRPII. (b) Western blot, recombinant *Pf*HRPII transferred to a PVDF membrane and conjugated with anti-*Pf*HRPII at 0.6 $\mu g \cdot mL^{-1}$ and anti-IgG with Perox enzyme coupled at 0.125 $\mu g \cdot mL^{-1}$.

3.1.2.1 Protein quantification

As described in section 2.2.5 in Material and Methods, a standard curve was used to determine the recombinant *Pf*HRPII concentration by the BCA method[81]. Each time this colorimetric method is used, a new standard curve should be performed by using a protein standard (BSA) with several known concentrations. By measuring absorbances at 562 nm of the samples described before in section 3.1.2 and the equation obtained by the standard curve (Figure 3.6), the total protein concentration was determined as 0.44 ± 0.11 $mg \cdot mL^{-1}$.

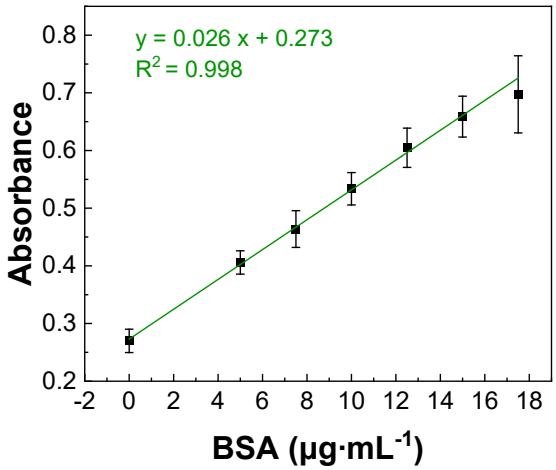

Figure 3.6: Standard curve with a protein standard BSA, with several known concentrations (0 to 17.5 µg·mL^{-1} range in 2.5 µg·mL^{-1} intervals).

The BCA method is useful to quantify total protein, nevertheless, it cannot differentiate distinct proteins that might be present in a sample. Hence, to obtain the approximate amount of *Pf*HRPII without the contribution of the contaminants, analysis of the SDS-PAGE gel can be used. Quantification is based in the intensity of the pixels in each band dyed with Coomassie Brilliant Blue. The bands pixel intensities from *Pf*HRPII and contaminants, were compared to the total protein concentration. Therefore, it was measured that 27% and 73% of the recombinant *Pf*HRPII and the contaminants, respectively, contained 0.12 ± 0.03 mg·mL^{-1} of recombinant *Pf*HRPII concentration in the solution purified.

Other expressions and purifications were performed, and several different batches were obtained during this Thesis (Table 3.1). The determination of the protein concentration and the MW was performed as described before (see sections 2.2.3 and 2.2.5 in Material and Methods). The homogenous batches had small and not significant differences on the MW, between 59 and 67 kDa, and concentration of total protein, that can be explained by the expressions by the *E. coli*. Other authors have reported similar protocols that obtain 10-50 mg of protein per liter culture volume[22] and other works with the same protocol was obtained 2.5 mg of recombinant *Pf*HRPII per liter of culture[103], however in this work was obtained between 3.6 ± 0.9 and 36.1 ± 2.1 mg per liter of culture (Table 3.1). This indicates that the purification might need some optimisations with varying reagents and their quantity[22].

Table 3.1: Purification batches of recombinant *Pf*HRPII performed during this Thesis, with a Ni-NTA column. *DC – Diego Carvalho

Purification number	Volume of purified protein fraction (mL)	Protein concentration ($mg \cdot mL^{-1}$)	Molecular weight (kDa)	Purity (%)	Pure protein yield (mg) per liter of culture
DC – Broken cells (2019)	0.2	2.2 ± 0.6	67	27	3.6 ± 0.9
Growth at 03/2022	0.6	$0.7 \pm (3.7 \times 10^{-2})$	65	23	36.1 ± 2.1
Growth at 03/2022	0.05	$0.2 \pm (7.5 \times 10^{-3})$	59	95	3.7 ± 0.1
Growth at 03/2022	0.1	$0.4 \pm (7.8 \times 10^{-4})$	53	95	$15.2 \pm (3.0 \times 10^{-2})$

3.2 Synthesis and characterisation of gold nanoparticles

3.2.1 Spherical gold nanoparticles

To synthetise seed-mediated AuNSs, AuNPs were firstly produced by a an alternative method to the Turkevich[83] protocol, described by Ojea-Jiménez *et al.*[61]. In this protocol the reagent addition order is inverted, *i.e.,* citrate is added before the chloroauric acid. This method improves size distribution and a uniform spherical shape of AuNPs[61]. Through UV-Vis spectroscopy, it is possible to observe a LSPR band at approximately 520 nm indicative of AuNPs ≈ 15 nm with no significant absorbance in the 600 nm region which is characteristic of aggregated NPs (Figure 3.7a). The UV-Vis spectrum obtained for the two synthesis were identical (see section A.2 in Appendices), meaning that this protocol was reproducible, similar to the study of the authors Ojea-Jiménez *et al.*[61].

The average diameter and concentration of the synthetised AuNPs were calculated, using the methodology described by Haiss *et al.*[84] and through the Lambert-Beer law[85] (see Equation 2.1 to Equation 2.3, section 2.2.6.1 in Materials and Methods). An average diameter of 11.8 ± 0.3 nm and concentration of 17.0 ± 2.0 nM was determined, with a standard-deviation of 11.6%. This procedure was performed every time the AuNPs were used as seeds for the AuNSs synthesis to assure a successful synthesis.

As can be seen in the Figure 3.7b, the LSPR band of the AuNPs has a slight red shift (≈ 5 nm) and a small increase in scattering between 600 and 700 nm which was confirmed by the aggregation index increase from 0.183 to 0.202 (see section 3.4 for AuNPs aggregation index). This suggest a very small aggregation and thus one month (0.203 of aggregation index) were accepted as the storage limit of the batch. Nevertheless, the relative standard deviation was 3%, confirming that AuNPs have remained stable for at least 4 months.

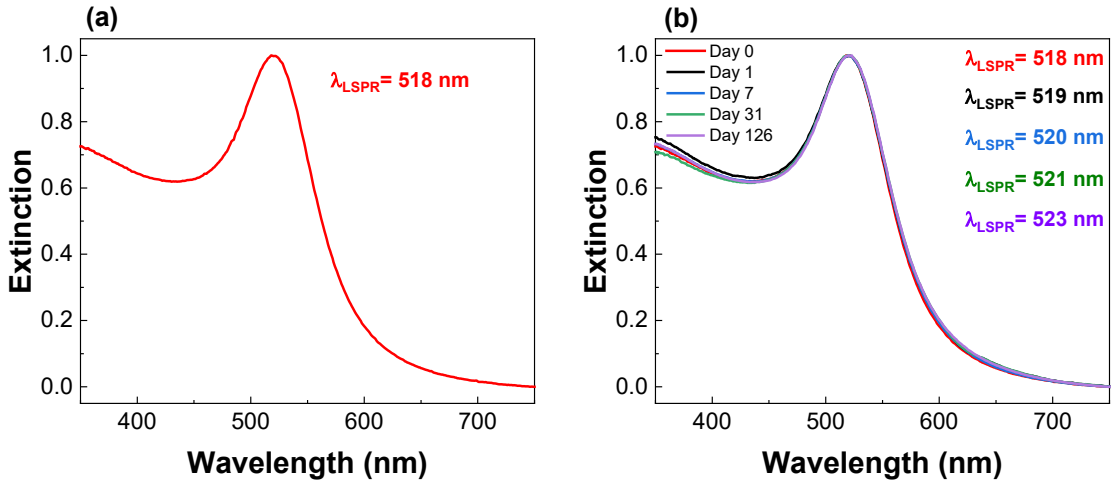

Figure 3.7: UV-Vis characterisation of AuNPs. (a) Normalised UV-Vis spectrum taken immediately after AuNPs synthesis, with a LSPR band at 518 nm. (b) Several normalised UV-Vis spectra of the same AuNPs synthesis taken over time, where the LSPR band varies between 518 and 523 nm.

3.2.2 Star-shaped gold nanoparticles

To improve the Raman signal enhancement provided by the SERS tags, AuNSs were produced. The AuNSs synthesis protocol described by Yuan *et al.*[66] was chosen since no surfactants are used, avoiding potential toxicity and problems related to replace the capping agent during further modifications[66]. Therefore, this method produces surfactant-free AuNSs which need to be functionalised with a capping agent immediately after the synthesis, to avoid AuNSs aggregation.

In contrast to spherical NPs, non-spherical NPs, such as AuNSs, have frequently several plasmonic modes originated from the core and the branches, which also depends on the NPs size and shape formed[39,104]. The LSPR bands obtained from several batches were between 588 to 775 nm, and the same was reporter for other authors[39] (see section A.2 in Appendices).

As we can see in the Figure 3.8 an example of a UV-Vis spectrum of AuNSs, the LSPR obtained was 671 nm and a small band approximately at 520 nm. The latter is thought to correspond to the core or ungrown seeds[104]. The AuNSs concentration was calculated through the molar extinction coefficient[66], which in this case was 0.80 ± 0.01 nM with 1.86% of standard-deviation.

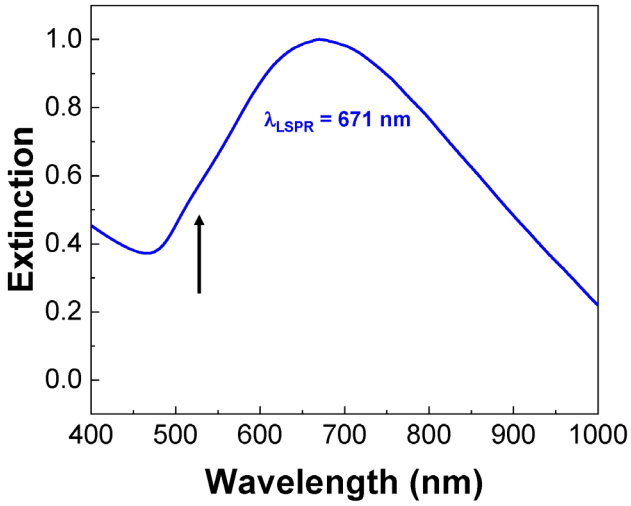

Figure 3.8: Example of an UV-Vis spectrum normalised of AuNSs taken immediately after the synthesis. The LSPR band obtained was centred at 671 nm.

3.2.3 Functionalisation of AuNPs and AuNSs

In this work, MBA was used as a Raman reporter, doubling as capping agent and intermediate layer, appropriate for protein bioconjugation. AuNPs and AuNSs were functionalised with this molecule, where the functionalised AuNPs are used as model for comparison with functionalised AuNSs. MBA was chosen since it binds to negatively charged AuNPs and AuNSs, through chemisorption with thiol group leaving a carboxyl group deprotonated to bind with other molecules, such as proteins[67]. When this molecule binds to the surface of the NPs, the local refractive index change, which cause a measurable shift in the LSPR band[42].

To functionalise AuNPs a 10 mM of ethanolic solution of MBA was incubated to achieve a molar ratio of 2500 as previously optimised by other authors[105]. The UV-Vis spectrum proved a successful functionalisation through the red shift of 3 nm of the LSPR band (Figure 3.9a).

To cover a full MBA layer, AuNSs were incubated overnight with MBA at 10 mM, with a molar ratio of 50,000[68]. As seen in the Figure 3.9b, AuNSs before functionalisation had a LSPR band centred at 654 nm, and after the incubation a shift to 669 nm was observed. AuNSs present larger change in the refractive index than AuNPs, this phenomenon is due to the hot spots of the AuNSs, tips or dips, that conducts enhanced electromagnetic field[106].

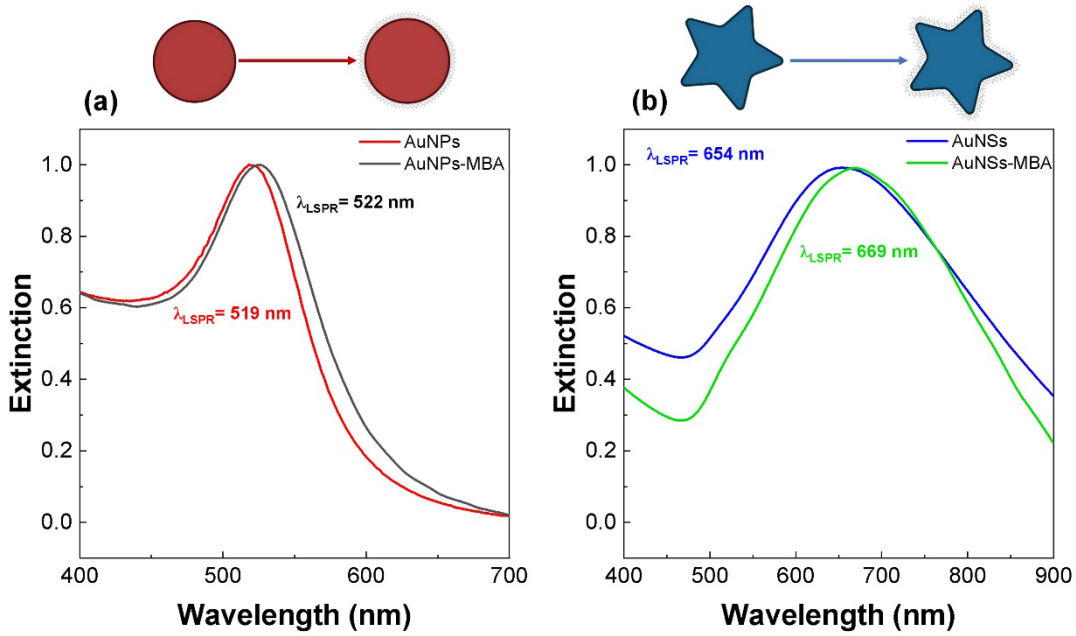

Figure 3.9: UV-Vis spectra of AuNPs (a) and AuNSs (b), and both functionalised with MBA. (a) AuNPs successful functionalisation was confirmed by a 3 nm red shift of the LSPR peak. (b) AuNSs successful functionalisation was confirmed by an 11 nm red shift of the LSPR.

3.3 Star-shaped gold nanoparticles conjugation

3.3.1 Conjugation through physisorption

3.3.1.1 Conjugation with BSA and effect by varying the pH value

BSA is a protein that is commonly used to block non-specific interactions[107], and in this case was used to bind to the NPs to understand how pH affects the bioconjugation. Thus, BSA was conjugated with AuNSs-MBA at different pH.

The BSA has a isoelectric point around 4.7[108], thus at pH 7, BSA is negatively charged. The AuNSs-MBA surface is also negatively charged at a physiological environment. Thus, if one introduces a biomolecule with opposite charge, electrostatic interactions will occur spontaneously and the electrostatic protein-protein repulsions are minimised[109,110]. Although BSA at pH 7 is mainly negatively charged, BSA adsorbs preferentially on the negatively charged of surfaces (*e.g.,* AuNSs-MBA) as reported by Dominguez-Medina *et al.*[111].

In this work, AuNSs-MBA at 0.2 nM were incubated with several BSA concentrations from 0 to 286 nM and at different pH values to compare influence of the pH in the binding capacity. After the incubation was performed, an AGE was used to characterise the binding between AuNSs-MBA and BSA at different pH values. As shown in Figure 3.10, the incubations at pH 6.5 and 7.5 have identical

results, and at pH 5.5 the AuNSs solution with BSA show some aggregation. At pH 5.5, the electrophoretic mobility of the samples revealed high variability between the triplicates whereby as seen in Figure 3.10. The first samples with BSA (from 0 to 59 nM) did not migrate in the gel, remaining in the well, unlike the other samples (from 79 to 286 nM) that could migrate. A trend could not be observed relating migration distance and BSA concentration. Nonetheless, for higher molar ratios of BSA (175, 194 and 286), the samples fully migrate in the sample, but these three samples were not enough to conclude about the formation of a full corona in AuNSs-MBA surface (for more information see section A.3 in Appendices).

As observed on Figure 3.10, for AGE from samples incubated at pH 6.5 and 7.5, the sample without BSA migrates more than the rest of the samples. As more protein is added to the sample and it is adsorbed by the AuNSs-MBA surface, its mass increases, AuNSs-MBA loses negative charge at the surface, and their electrophoretic mobility decreases, resulting in less migration. At concentrations higher than 98 nM BSA at pH 6.5 and 7.5, the mobility remains the same, which corresponds to the saturation of BSA in the conjugate. Thus, the most suitable BSA concentration to form a full corona was between 79 and 98 nM.

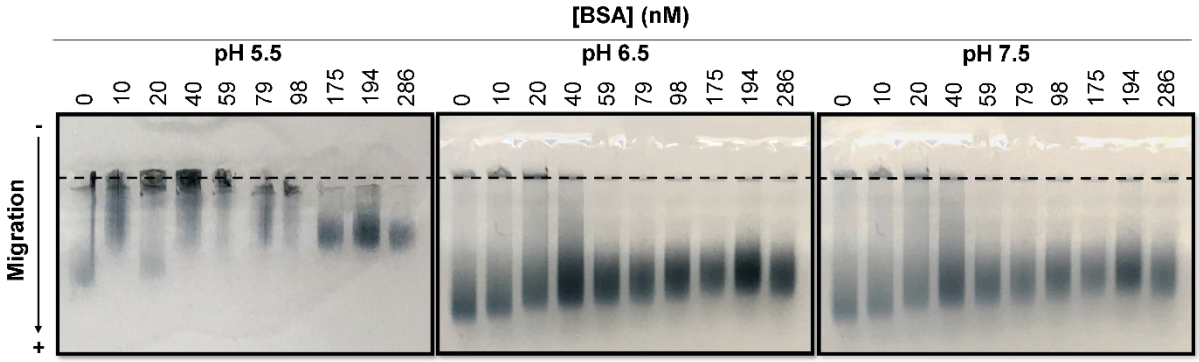

Figure 3.10: Digital images of AGE with samples of AuNSs-MBA incubated with several BSA final concentrations (from 0 to 286 nM) at different pH values (5.5, 6.5 and 7.5).

The migration of each band was measured through the eReuss software, by fitting Gaussian curves to the image intensity profiles, which was used to calculate the electrophoretic mobility of each sample. Electrophoretic mobility is defined as the ratio of a component migration velocity (v) to the strength of the driving field (E). This velocity was calculated by the migration given by the software divided by the AGE running time. The energy field is defined by the ratio between the voltage used and the distance between the electrodes. The results of AGE are represented by the variation of mobilities, which are the variations relative to the maximum mobility band ($\Delta\mu$), this equation is represented bellow and have $m^2 \cdot V^{-1} \cdot s^{-1}$ as units (Equation 3.1):

$$\Delta\mu = \frac{v}{E} \qquad \text{Equation 3.1}$$

This data was plotted with BSA final concentration and fitted to a Hill-type adsorption isotherm, represented in the next equation (Equation 3.2):

$$\Delta\mu = \frac{\Delta\mu_{max} \cdot x^n}{K_D^n + x^n} \qquad \text{Equation 3.2}$$

where Δμ is the difference in electrophoretic mobility between the data point and the AuNSs before any antibody or protein is conjugated, x is the concentration of the antibody or protein added to the sample, K_D is the dissociation constant (in M) correlating to the value of the x concentration for one-half of $\Delta\mu_{max}$, and n is the cooperativity parameter. In the Hill model, the cooperativity parameter defines a positive (n > 1), or negative (n < 1), or non-existent (n = 1) cooperativity, which the binding of the next component (antibody or protein) is favoured, or unfavoured, or no cooperativity is present, respectively.

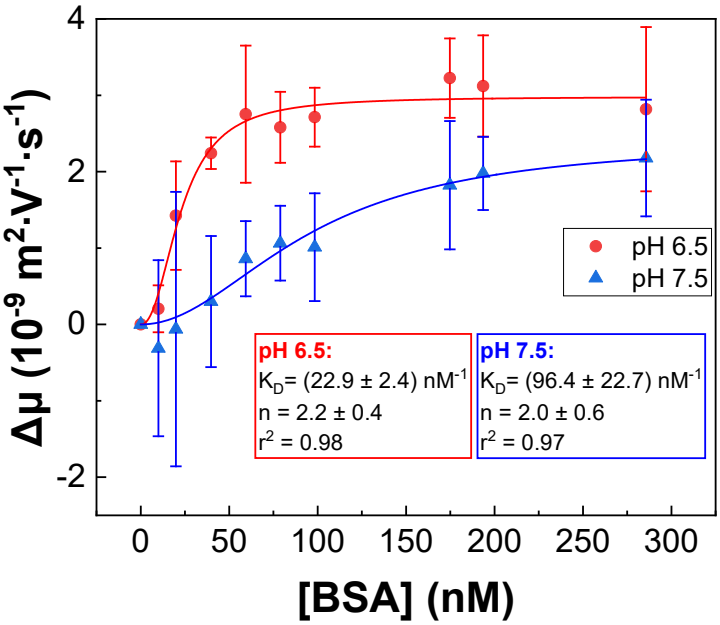

Figure 3.11: Variation of electrophoretic mobilities of different samples of AuNSs with varying BSA concentrations (from 0 to 286 nM). Electrophoretic mobility values were calculated through the mobility obtained by eReuss software analysis of digital images. The results of the samples at pH 6.5 are represented by red spheres with a corresponding red box, and the samples at pH 7.5 are represented by blue triangles with a corresponding blue box. The error bars represent the standard deviation of triplicate measurements.

Figure 3.11 represents electrophoretic mobilities obtained for the bioconjugation made with the two pH values at which it was possible to obtain robust bioconjugates, *i.e.*, pH 6.5 and 7.5. At basic buffer, AuNSs-MBA had the necessary electrostatic repulsion to avoid AuNSs aggregation[59]. Thus, at lower pH values, AuNSs-MBA are unstable. At basic buffer, the negatively charged groups of BSA dissociated and the repelling forces overcomes the attracting forces[112]. Although BSA prefers binding at lower pH, at pH 5.5 AuNSs-MBA are unstable, and adding BSA at this pH the instability is increased, leading to aggregation. Therefore, the samples at pH 5.5 did not migrate into the gel, and the AGE results for these samples had larger errors when compared with the other samples with more basic pH. The Hill model did not fit in these results, due to the great variation of aggregation in triplicates samples. At pH 6.5 and 7.5, the electrophoretic mobilities obtained were similar having only a different dissociation constant (K_D). For the samples at pH 6.5 the dissociation constant was lower (22.0 ± 2.4 nM^{-1}) than the samples at pH 7.5 (96.4 ± 22.7 nM^{-1}), which means that half of the AuNSs-MBA binding sites are occupied. The pH influences the binding through physisorption and at pH 7.5, which has a more than three-times higher K_D than at pH 6.5, the binding of BSA has low-affinity to the AuNSs-MBA surface. At pH 6.5, it is possible to have more BSA adsorbed to the AuNSs surface, since the $\Delta\mu_{max}$ is higher ($(3.2 \pm 0.5) \times 10^{-9}$ m^2·V^{-1}·s^{-1}) than at pH 7.5 ($(2.2 \pm 0.8) \times 10^{-9}$ m^2·V^{-1}·s^{-1}), meaning that at pH 6.5 the binding seems more favourable[113], choosing this pH for future work.

Other authors obtained a higher K_D (256 ± 50 μM) for 51 nm citrate-capped spherical AuNPs with a pH solution of 7-7.5[111], which cannot be directly compared due to the different morphologies, concentrations and the analysis was through a modified Langmuir model. Nevertheless, another study of 40 nm citrate-capped spherical AuNPs, with a same range of pH solution, had the same order of magnitude of dissociation constant[114]. However, these two studies had a negative cooperativity parameter, indicating an unfavoured binding where the affinity for other ligands decreases once the binding sites are filled[111,114]. For the samples at pH 6.5 and 7.5 the cooperativity parameter was higher than 1, indicative for a positive cooperativity between AuNSs and BSA. This difference might be explained due to anisotropic NPs that can increase the affinity of BSA to AuNSs-MBA surface[111].

3.3.1.2 Conjugation with anti-Perox

Several aliquots with AuNSs-MBA at 0.2 nM were incubated with different final concentrations of anti-Perox antibodies (from 0 to 221.51 nM). This experiment was performed in a similar way to the conjugation of BSA to AuNSs-MBA (see section 3.3.1.1 in Results and Discussion). As we can observe in AGEs presented in Figure 3.12a, all the samples migrate from the negative to the positive electrode, which indicates a negative global charge. The higher the amount of anti-Perox surrounding the AuNSs-MBA, the lower is the electrophoretic mobility, which can indicate that the AuNSs-MBA

are not only becoming larger and heavier, but also were losing the negative charged surface due to the interaction with positive groups of anti-Perox from the conjugation process. It is possible to observe a stable migration in the samples with high anti-Perox final concentrations, suggesting the saturation of anti-Perox in the AuNSs-MBA surface. The concentration 81 nM was considered a suitable concentration to form stable bioconjugates.

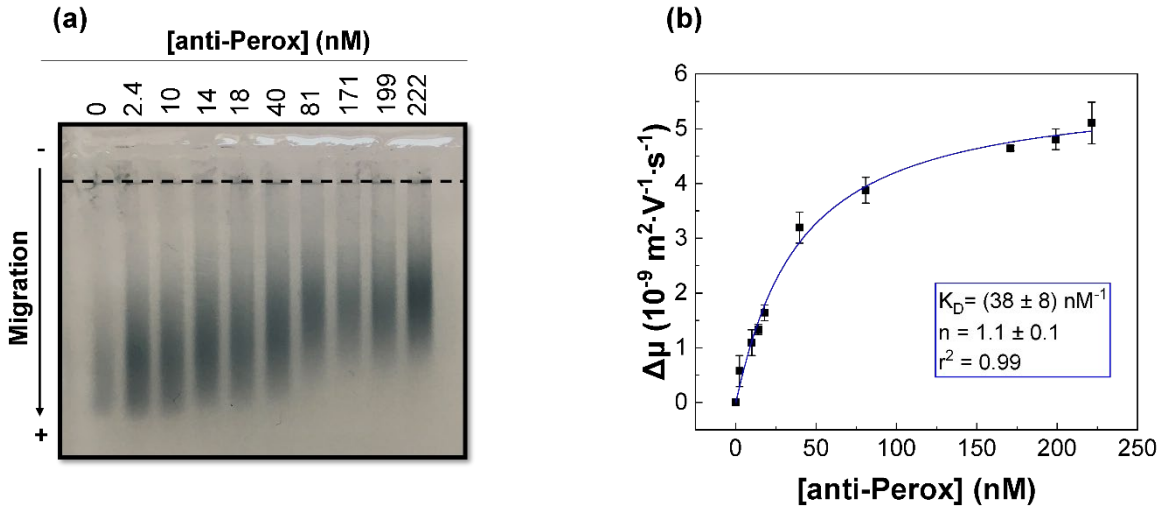

Figure 3.12: AuNSs-MBA were incubated with several concentrations of anti-Perox (from 0 to 221.51 nM). (a) Digital image of AGE with samples of AuNSs-MBA incubated with anti-Perox. (b) Variation of electrophoretic mobilities of different samples. The values of electrophoretic mobility were calculated through the mobility obtained by eReuss software analysis of digital images and fitted to Equation 3.2. Fitting parameters are represented in a blue box. Error bars represent the standard deviation of triplicate measurements.

Electrophoretic mobilities were calculated through the equations 3.1 and 3.2 (see section 3.3.1.1 in Results and Discussion), with the mobilities obtained by eReuss software analysis of digital images. The data was plotted with BSA final concentration and fitted to a Hill model, seen in the Figure 3.12b. This fitting has dissociation constant of K_D = (38 ± 8) nM^{-1} of anti-Perox, and a cooperativity parameter higher than 1, which indicated a favoured binding to the next antibody. In comparison, the dissociation constant for anti-Perox had the same order of magnitude that the dissociation constant for BSA. The value of K_D was congruent with the obtained by Cui *et al.*[114] for citrate-AuNPs with a 39 nm of diameter, despite the fact that some authors had obtained lower values of K_D for 51 nm citrate-AuNPs[111].

3.3.2 Covalent conjugation

To ensure a stable bound between the AuNS-MBA and the antibody, a covalent conjugation was promoted. This procedure ensures that the antibody is linked to the AuNS-MBA and is not

washed during successive washes[70,115]. Seven different samples were prepared, which had the AuNSs functionalised with MBA with different conjugations. AuNSs-MBA and AuNSs-MBA conjugated with anti-Perox were used has comparison, since the first has no conjugate, and second has the antibody conjugated through physisorption. AuNSs-MBA conjugated with anti-Perox and with a mediator zero length cross-linker EDC/SNHS, was also prepared. The EDC/SNHS coupling functions as mediator linker to produce the covalent conjugation between amine groups of proteins (in this case antibodies) and carboxylic groups from AuNSs-MBA, producing a stronger bound than physisorption conjugation[70].

To simulate and test the sandwich immunoassay, AuNSs-MBA was conjugated with anti-Perox for detection and BSA for blocking. This SERS tags (AuNSs-MBA-EDC/SNHS-anti-Perox-BSA) were then prepared and conjugated with the antigen (Perox) and anti-Perox to complete de sandwich for the immunoassay. Additionally, the anti-Perox was conjugated in the SERS tags, *i.e.,* without Perox, to be used as negative control. After the incubation, all these samples were tested through UV-Vis spectroscopy and by AGE. All the proteins and antibodies were conjugated with a concentration of 84 nM to the AuNSs-MBA surface, to guarantee the full corona conjugation and removing the excess by centrifugation[57].

The conjugation of proteins and antibodies on the AuNSs-MBA surface change the local refractive index, causing a red shift of the plasmon resonance band[42], as we can see in the Figure 3.13. The LSPR of these samples continue to red shift by adding more macromolecules, except in the last sample, which is SERS tags-anti-Perox. The absent LSPR red shift from SERS tags-anti-Perox sample is a consequence of the lack of Perox. The anti-Perox cannot form the immunocomplex in absence of the antigen, *i.e.*, the Perox thus, the final sample is similar to the SERS tags itself without addition of the anti-Perox.

Interestingly, the LSPR band of AuNSs-MBA conjugated with anti-Perox with or without EDC/SNHS do not have a great difference due to the cross-linking event, which has a covalent conjugation or physisorption conjugation, respectively[70].

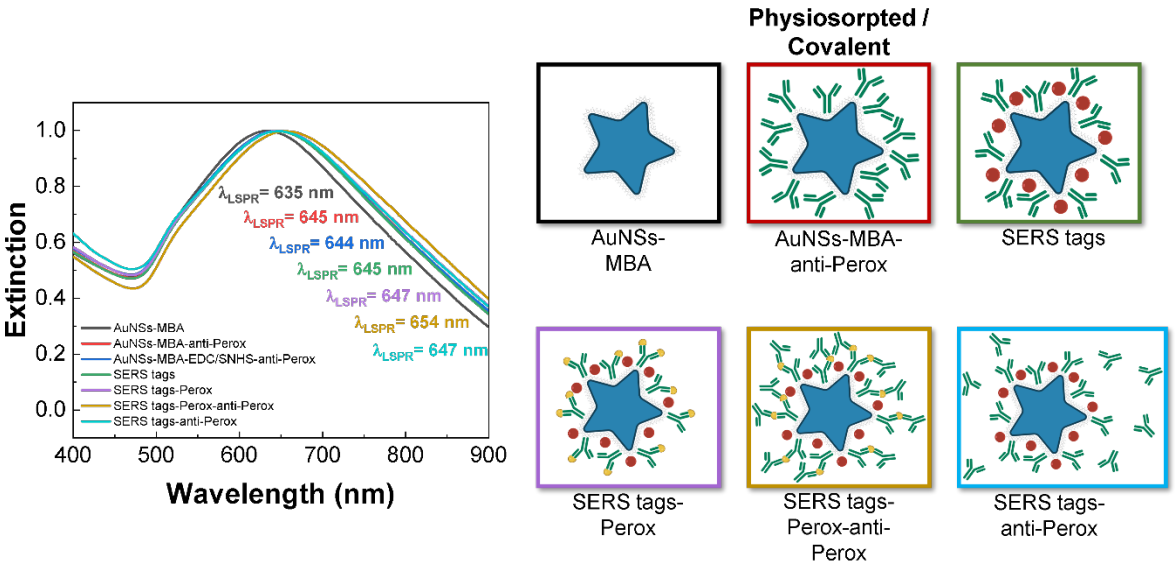

Figure 3.13: UV-Vis spectra normalised of seven different samples, such as AuNSs-MBA, AuNSs-MBA-anti-Perox, AuNSs-MBA-EDC/SNHS-anti-Perox, SERS tags (AuNSs-MBA-EDC/SNHS-anti-Perox-BSA), SERS tags-Perox, SERS tags-Perox-anti-Perox, and SERS tags-anti-Perox. Each sample is represented with a colour, which as LSPR maximum in the same colour. The conjugation of anti-Perox to the AuNSs-MBA surface was accomplished through physisorption and covalent with EDC/SNHS as mediator linker.

An AGE was performed with all these bioconjugates samples, as we can see in the Figure 3.14, resulted in different electrophoretic mobilities. Similar to UV-Vis spectra, when more proteins and/or antibodies are adsorbed by the AuNSs-MBA surface, the conjugates starts to reducing the global negative charge at the surface, and their mass increases, resulting in less electrophoretic mobility[70]. The sample SERS tags-anti-Perox was an exception, since it is a negative control because the Perox is absent, consequently the anti-Perox added has not Perox to recognise and bound, and it does not interact with the BSA and anti-Perox that are already conjugated to the AuNSs-MBA surface (Figure 3.14 represented by a red bar). The simulated immunocomplex has proven that the sample SERS tags-Perox-anti-Perox[68] is working, since anti-Perox in the AuNSs-MBA surface recognised the respective protein (Perox) and an equal antibody added to these complex, recognised the same antigen forming a sandwich that is indicative of the presence of the Perox antigen (Figure 3.14 represented by a green bar).

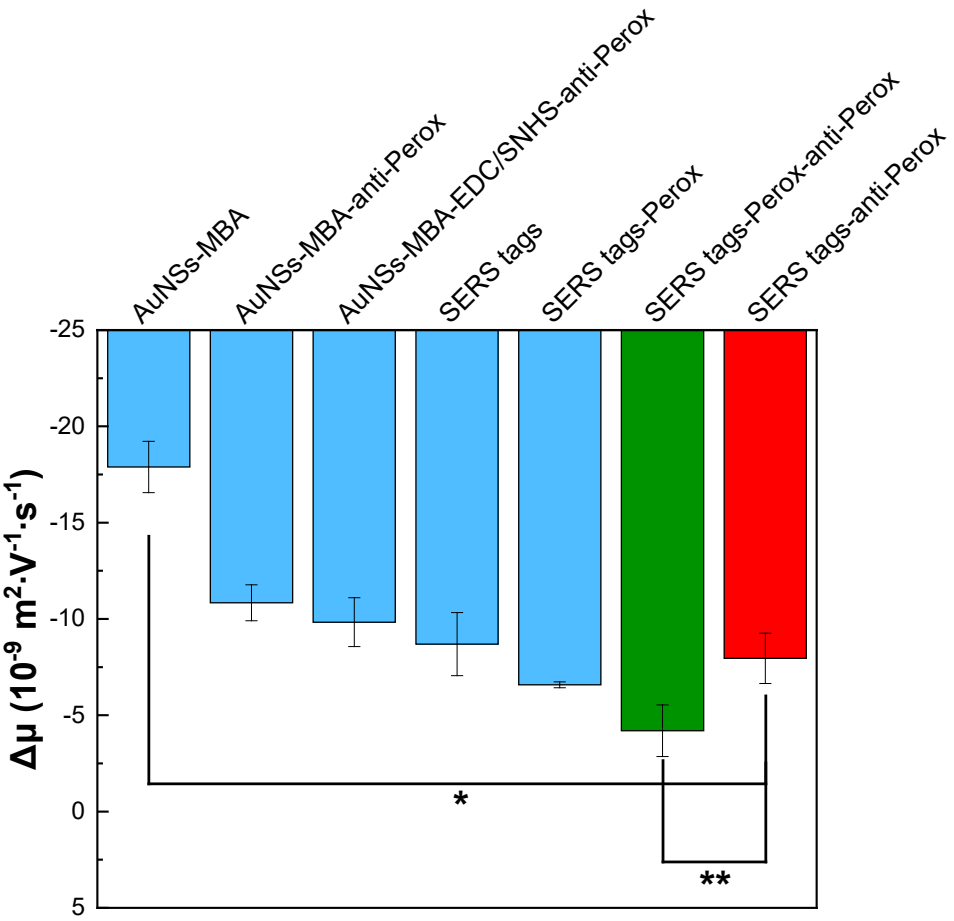

Figure 3.14: Electrophoretic mobility determined by AGE for the different seven samples. The green bar corresponds to the positive control, *i.e.*, the immunocomplex formed to detect Perox. The red bar is a negative control, since the Perox is not present. The error bars represent triplicate experiments with three different sets of bioconjugates. * *p*-value < 0.01. ** *p*-value < 0.05.

3.4 Colloidal stability of gold nanoparticles and SERS tags

Since the final aim of this work involves the incubation of SERS tags with a blood sample that contains salt, the colloidal stability of the SERS tags was studied[116]. Therefore, this study had the purpose to determine the stability of AuNPs with increased concentrations of sodium chloride (NaCl). Electrostatic repulsive forces can maintain NPs with negative charges on the surface stable, and the addition of salt in the solution reduces these electrostatic repulsive forces. At a certain ionic strength, the NPs become very unstable and start to aggregate[117]. This concentration is referred as the critical coagulation concentration (CCC). The coagulation of the NPs can be examined by UV-Vis spectroscopy or visually, since the colour of the NPs solution change due to the shift of the LSPR band. So, the

CCC is defined by the highest concentration of salt which the colloid is unchanged and the lowest concentration that causes aggregation[118].

Several aliquots were prepared with AuNPs-MBA at 2 nM and varying concentrations of NaCl from 0 to 500 mM, added immediately before reading in UV-Vis spectroscopy. At lower concentration of NaCl the LSPR band is approximately at 525 nm. From the concentration of 30 mM of NaCl, the LSPR band red shifts to about 630 nm, which is congruent with aggregation of AuNPs. The colours in some aliquots at higher ionic strength changed to blue as soon as the start of the reading. As seen in the Figure 3.15a, the UV-Vis spectrum at 20 mM and 30 mM concentration of NaCl has a significant difference, which indicates that with 30 mM of salt the AuNPs are aggregated.

Similarly, the same study was conducted with AuNSs-MBA to understand how the morphology might influence the stability of the particles. In this experiment a smaller interval of NaCl concentrations within the range 2 to 10 mM was included. The Figure 3.15b represents the UV-Vis spectra with AuNSs with increasing NaCl concentration, whereby a slightly difference of LSPR band is observed between 6 and 8 mM of NaCl. This difference was also observed visually, where the solution changed colour from strong to light blue. At lower concentration of NaCl, the LSPR band was around 600 nm. From 8 mM concentration of NaCl, the LSPR band red shifts to about 800 nm, which agrees with aggregation of AuNSs.

Afterwards, the colloidal stability was tested with the samples AuNSs-MBA-EDC/SNHS-anti-Perox and SERS tags to compare with AuNSs-MBA and to see the effect of blocking with BSA (Figure 3.15c and d). AuNSs-MBA-EDC/SNHS-anti-Perox showed higher stability than AuNSs-MBA, as can be verified by the red shift in the LSPR band at 40 mM of NaCl concentration whereas for the AuNSs-MBA the red shift was observed at only 8 mM (Figure 3.15c). This red shift of 28 nm was followed by a change in colour from strong to light blue. Adding the BSA completes the bioconjugation process originating the SERS tag. This sample had a LSPR band red shifted at 200 mM, simultaneously it was seen visually the change of colour of the sample (Figure 3.15d).

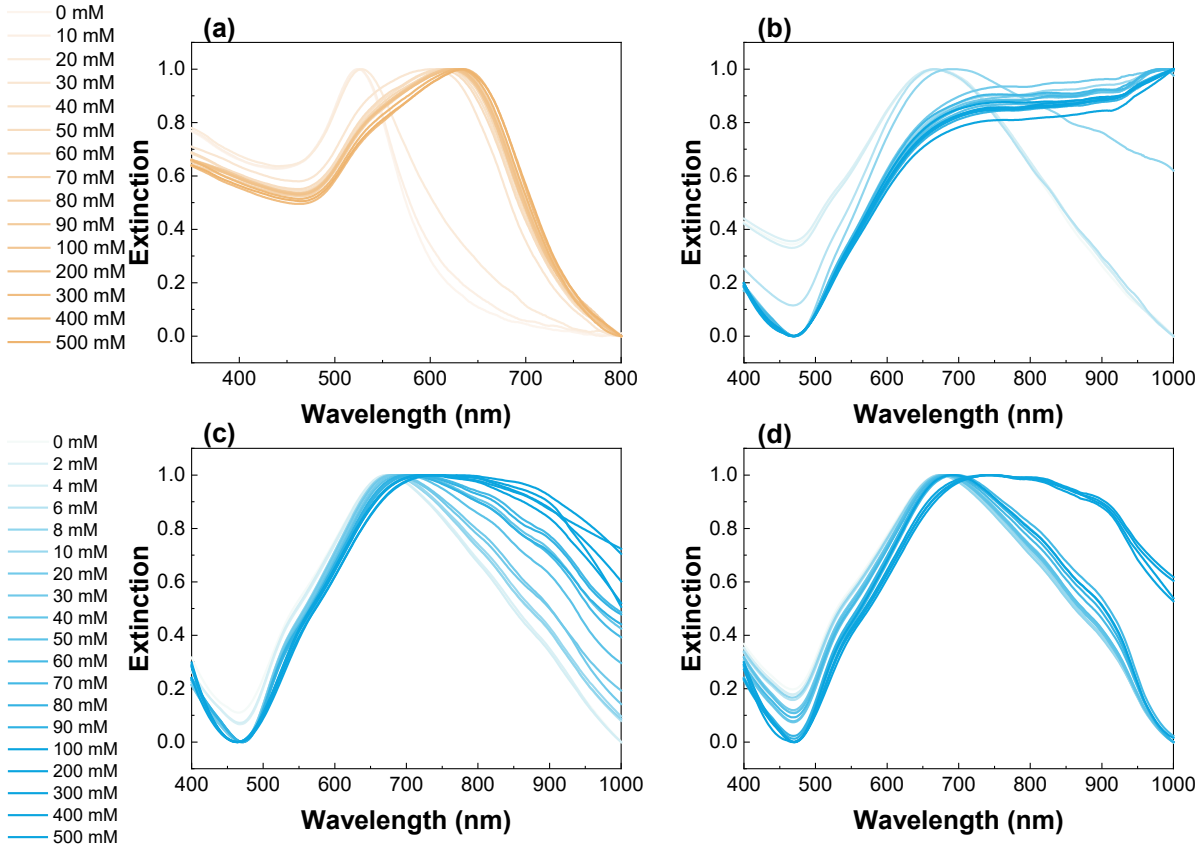

Figure 3.15: UV-Vis spectra normalised of gold NPs with NaCl at several concentrations (0-500 mM). (a) AuNPs-MBA, where the LSPR band red shifted with 30 mM concentration of NaCl, (b) AuNSs-MBA, whereupon the LSPR band red shifts to about 800 nm with only 8 mM concentration of NaCl, (c) AuNSs-MBA-EDC/SNHS-anti-Perox, where at 40 mM of NaCl concentration the LSPR band shifted, (d) SERS tags, which had a LSPR band red shift with 200 mM concentration of NaCl.

The aggregation index for AuNPs-MBA was calculated through dividing the value of absorbance at 600 nm and LSPR (Figure 3.16). A considerable difference is seen between the concentrations 20 and 30 mM of NaCl, corresponding the difference seen visually and by UV-Vis spectra. Other authors have been described different values of CCC, such as 50 mM of NaCl with AuNPs coated with poly(acrylic acid)[44], 50 mM of NaCl with ethyl cellulose NPs[117], 70 mM of NaCl with citrate-coated AuNPs[119], and 200 mM of NaCl with AuNPs coated with 11-mercaptoundecanoic acid[119]. Thus, the capping agent influences the CCC of the NPs, and a lower value was obtained in this work when compared to other reports, which can be explained by the higher dimensions of these capping agents that promote steric repulsion stabilising the NPs[119].

The aggregation index for AuNSs-MBA samples were calculated through dividing the value of the area under the curve and LSPR[86] (Figure 3.16). The AuNSs solution with 8 mM concentration of NaCl has a higher aggregation index than at 6 mM of NaCl, which confirms the CCC seen visually and by UV-Vis spectra. This electrostatic coagulation is mediated by the anions present, at higher concentration of NaCl the Cl^- anions binds electrostatically to the positively charged AuNSs, resulting

in the aggregation of the AuNSs[120]. In comparison, the AuNSs aggregates with lower concentrations of NaCl than the AuNPs, which can be explained by the anisotropic shape or the surface potential of the AuNSs[118].

The antibody added and binding in the AuNSs-MBA surface creates a higher stability, in which between the concentrations 30 and 40 mM of NaCl the aggregation index has a slight increase, congruent with the UV-Vis spectra and visual observation (Figure 3.16). Thus, the CCC determined for the AuNSs-MBA-EDC/SNHS-anti-Perox was between 30 and 40 mM of NaCl concentration. Adding another protein in this surface, such as BSA, improves the stability greatly until reaching 200 mM concentration of NaCl in the sample (Figure 3.16), which is also visible in the UV-Vis spectra. This confirms the CCC value for SERS tags between 100 and 200 mM of NaCl concentration.

The stability study revealed a CCC between 100 and 200 mM of NaCl, which was much higher than the CCC values observed for AuNSs-MBA (between 6 and 8 mM) and AuNSs-MBA-EDC/SNHS-anti-Perox (between 30 and 40 mM). Thus, is possible to conclude that the BSA in this sample can block the ligands sites and stabilise more the colloidal solution. Although are lack of studies of AuNSs in saline environment, Afrooz *et al.*[44] reporter a similar CCC value of ≈ 250 mM NaCl for the anisotropic nanorods coated with poly-acrylic acid[44], which is very difficult to compare since nanorods have a different behaviour. Since that a blood sample may contain 154 mM of NaCl concentration in a healthy patient, the SERS tags can be used for the LFA test.

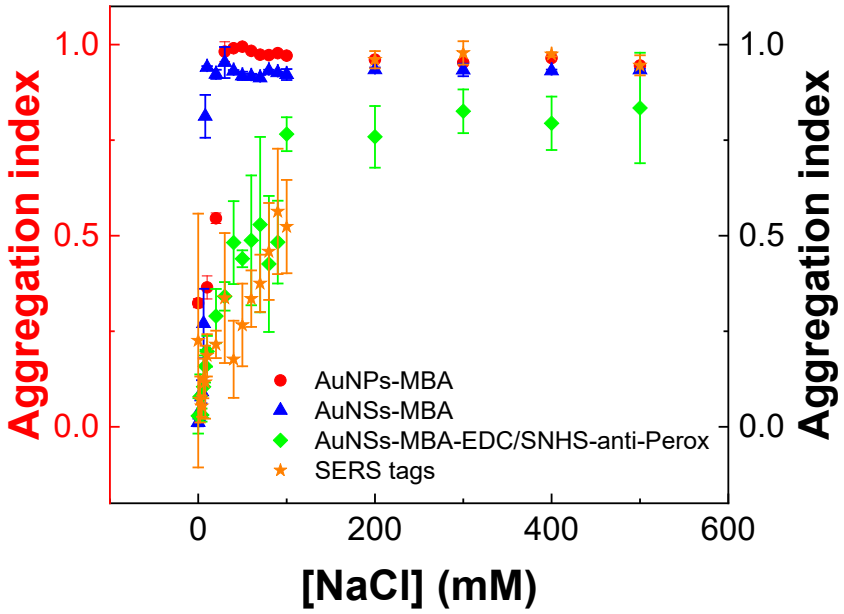

Figure 3.16: Aggregation index calculated through UV-Vis spectrum vs. corresponding NaCl concentration. The aggregation index of AuNPs-MBA (red dots) was calculated through the value of absorbance at 600 nm divided by the value of LSPR (red yy axis). For all the samples that contains the AuNSs-MBA, the aggregation index was calculated and normalised

through dividing the value of the area under the curve and the LSPR (black yy axis). The AuNSs-MBA are represented by blue triangles, the AuNSs-MBA-EDC/SNHS-anti-Perox by green rhombus and the SERS tags by orange stars. The error bars represent the standard deviation of triplicate measurements.

3.5 Enzymatic activity assay of peroxidase

The enzymatic activity assay was performed to prove the recognition of Perox by the respective antibody conjugated in the SERS tags. The samples SERS tags-Perox, SERS tags-Perox-anti-Perox, and SERS tags-anti-Perox, were tested in this assay after washing. The peroxidase activity was calculated has described in section 2.2.11 through the measurement of absorbances at 405 nm during 10 min, and in the Figure 3.17 the peroxidase activity of each sample are represented. The sample SERS tags-anti-Perox does not show any enzyme activity, due to lack of antigen, which was used as the blank sample. In comparison, SERS tags-Perox-anti-Perox (0.56 Units/mg_{solid}) has higher enzymatic activity than the SERS tags-Perox (0.53 Units/mg_{solid}), since the anti-Perox conjugated afterwards leads to higher captured amount of Perox. This experiment proves the recognition of Perox by the anti-Perox, similar Tripathi *et al.*[121] made a successful study with the same behaviour but for the recognition of an antibody[121].

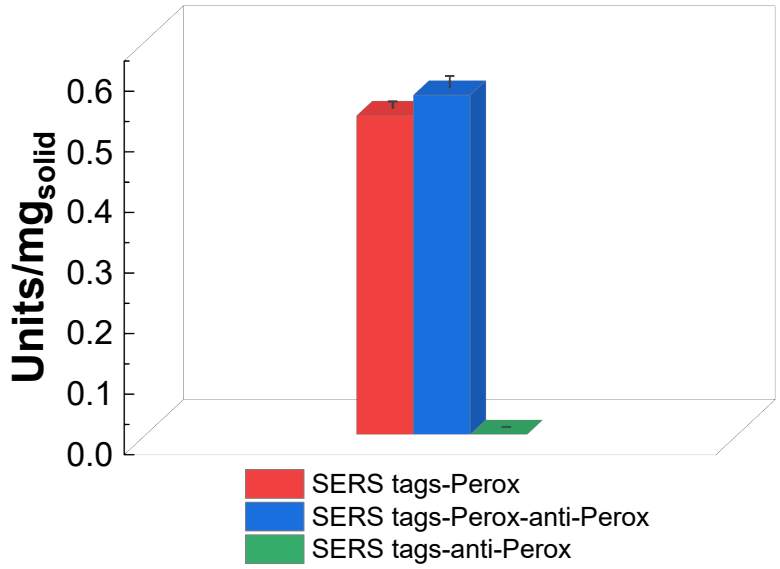

Figure 3.17: Peroxidase activity (Units/mg_{solid}) of the samples SERS tags-Perox (red), SERS tags-Perox-anti-Perox (blue), and SERS tags-anti-Perox (green). The SERS tags-anti-Perox showed no enzymatic activity, since was not added Perox. The error bars represent the standard deviation of triplicate measurements.

3.6 Dynamic light scattering

DLS is a technique used to determine the polydispersity and the hydrodynamic diameter of NPs. For the AuNSs, the diameter obtained is an approximation due to their inherent anisotropy morphology with tips of varying size contrary to spherical forms[88]. For this work, the samples AuNSs-MBA, AuNSs-MBA-EDC/SNHS-anti-Perox, and SERS tags were evaluated. As shown in the Figure 3.18a, the hydrodynamic diameter was obtained to each sample. The colloidal solution AuNSs-MBA had a hydrodynamic diameter of 77.2 ± 0.9 nm. The anti-Perox bound on the AuNSs-MBA surface, with EDC/SNHS as mediator cross-linker, caused an increase in diameter of 19.9 ± 0.5 nm (Figure 3.18b). The BSA protein in this conjugate can prevent the non-specific binding and has a hydrodynamic diameter approximately of 5 nm[111]. Thus, the addition of BSA to AuNSs-MBA surface causes an increase in the hydrodynamic diameter. In the case of AuNSs-MBA-EDC/SNHS-anti-Perox, when BSA (≈ 5 nm)[111] is added, it will block between the interstices that lack anti-Perox molecules. As a result, the difference between AuNSs-MBA-EDC/SNHS-anti-Perox and the entire SERS tags (*i.e.,* AuNSs-MBA-EDC/SNHS-anti-Perox-BSA) is smaller than the resolution needed for DLS to identifying as two different populations[88]. Hence, no appreciable difference is observed, since it was obtained a hydrodynamic diameter of 91.9 ± 1.5 nm, as seen in the Figure 3.18b. This can be explained with some changes in the structure of the protein after conjugation or the rearrange of the antibodies when BSA was added[122,123]. The hydrodynamic diameter of AuNSs-MBA-EDC/SNHS and the SERS tags can prove the binding of the molecules (anti-Perox and BSA) to the AuNSs-MBA surface and not the formation of aggregates, due to the three samples that had identical results. A close analysis regarding the standard deviation of AuNSs-MBA-EDC/SNHS-anti-Perox (97.1 ± 1.6 nm) and SERS tags (91.9 ± 1.5 nm), shows that this difference is not significant.

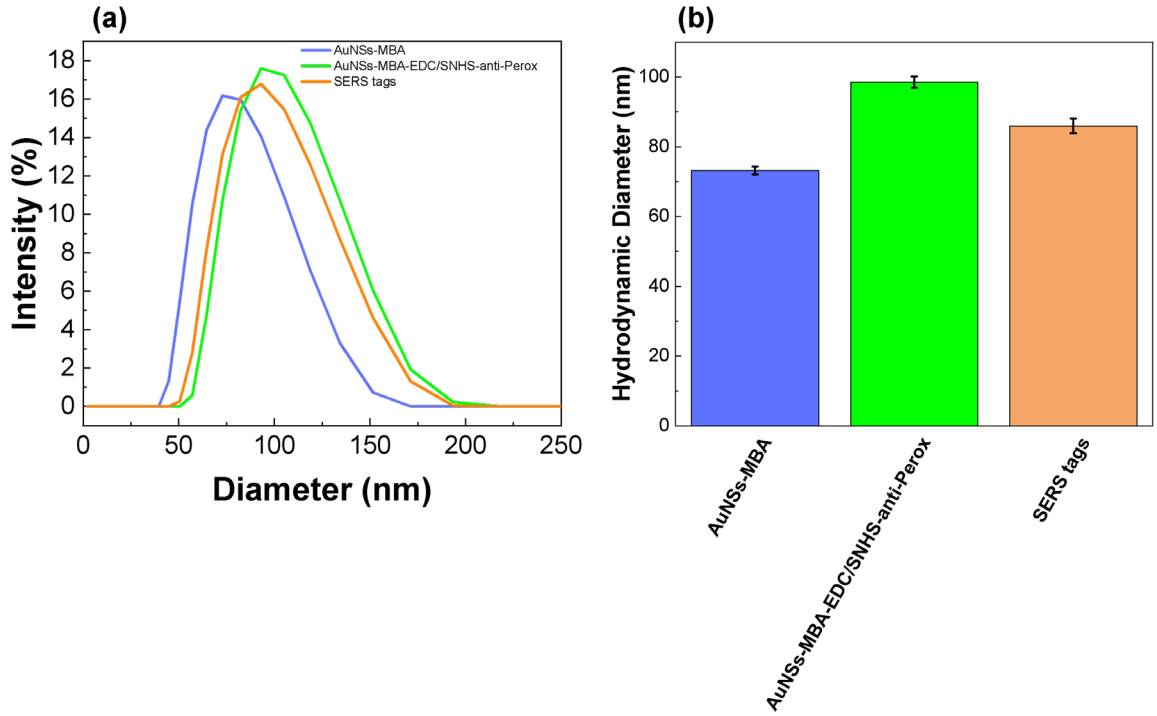

Figure 3.18: Results obtained for DLS measurements of AuNSs-MBA, AuNSs-MBA-EDC/SNHS-anti-Perox and SERS tags. (a) Percentage intensity obtained for the hydrodynamic diameter (nm) measured for these samples. (b) Hydrodynamic diameter (nm) obtained for each bioconjugate. The error bars represent the standard deviation of triplicate measurements.

Other parameter evaluated was the polydispersity index (PDI). The sample is considered highly monodisperse, moderately and highly polydisperse, when the PDI value is ≤ 0.1, 0.1-0.4, and > 0.4, respectively[88]. For AuNSs-MBA, AuNSs-MBA-EDC/SNHS-anti-Perox, and SERS tags, the PDI values obtained were 0.25 ± 0.06, 0.17 ± 0.05, and 0.18 ± 0.08, respectively. This means that all these samples were moderately polydisperse, which is common in AuNSs since there are differences in shape, length, and sharpness of their tips[68,124].

3.7 Lateral flow assay

To extend the sensitivity of the current LFAs, SERS tags were used to simultaneously function as colorimetric and SERS labels. Having the SERS tags and the recombinant malaria antigen produced, several optimisation studies of the LFA were performed and are described below.

A starter kit from Advanced Microdevices was used as described at 2.2.14 in Materials and Methods. Initially, several optimisations regarding the components of this kit were tested, namely (i) the nitrocellulose membrane (NM), (ii) an additional blocking NM step, (iii) the concentration of SERS tags, (iv) the absorbent pad and (v) antibodies. All the dimensions of the components were

based on previous work by Tomás *et al.*[71]. Afterwards, several dilutions of anti-Perox and anti-IgG in the test and control line respectively, were also tested to determine the minimum concentration required for reliable colorimetric detection, evaluated by the ImageJ software. ImageJ software was used to analyse the photographs, whereby three regions (the background, control, and the test line) were evaluated by selecting three squares of each region. From each square, a histogram was generated (for further information see annex I.2). This histogram has a grey scale, between 0 and 255 pixels, which corresponds to black and white, respectively[125]. This means that for every square selected, lower visibility of the colour line translates into high values of pixel intensity. Consequently, the difference between the background and test line must be high to provide a reliable positive result. All these optimisations had the objective to evaluate and select the LFA with better performance, *i.e.*, with higher difference of intensity between the background and test line. Using Perox and the respective antibody reduces the costs of these studies, and the developed system can be used as model system for our objective target antigen, *Pf*HRPII. In this LFA, the antigen is captured by the SERS tags, and an immunocomplex in the sandwich format is formed in the test line, which has anti-Perox immobilised. The anti-Perox recognises the antigen bound in the SERS tags and a coloured line is produced in the test line. In a case of a negative sample, the SERS tags do not capture the Perox, and consequently, do not bind in the test line producing any visible colour. The remaining SERS tags continue to flow by capillary forces, passing through the control line that has anti-IgG able to recognise the anti-Perox from the SERS tags. The bond between the SERS tags and the anti-IgG is revealed by a AuNSs blue colour from the SERS tags that appears and confirms that the LFA is valid. If anti-IgG fails to recognise the SERS tags, then, no colour appears in the control line and the LFA test is considered invalid.

3.7.1 Nitrocellulose membrane selection

Initially in all the NM types blocked with skim milk powder and PBS-T a control and test line were spotted manually, as described in 2.2.14.1. Afterwards, a positive sample (Perox in potassium phosphate buffer) was incubated in the NM, followed by an incubation with SERS tags at 1 nM. In total, eight types of NM were tested, namely: a low protein binding membrane (i) CNPF8 and (ii) CNPF10; a high protein binding membrane (iii) CNPC12 and (iv) CNPC15; and a highest protein binding membrane (v) CNPH70, (vi) CNPH90, (vii) CNPH150, and (viii) CNPH200. This study had the objective of evaluating which membrane generated the best signal, *i.e.*, the higher contrast when the SERS tags bind to the lines. To ensure the maximum signal, the membrane should exhibit some desirable features such as facilitating a homogenous flow, a strong functionalisation for capturing the receptor, and exhibit low non-specific binding[75]. After the assay, digital pictures were taken and analysed with ImageJ to compare colour intensities obtained in test line and background of NM.

The selection of the most suited NM was based on the difference between the background and the test line intensity, which means that the test line must have a distinguishable colour in comparison to the background, since the control line in all the NMs were highly visible at naked eye. Figure 3.19 shows that the CNPC15, the CNPH70 and the CNPH90, were the tests with least difference between the background and the test line colour giving 5, 6 and 5 pixels, respectively, which is congruent with what was seen in the naked eye. The CNPH150, the CNPF10, and the CNPC12, had a slightly higher difference than between the background and the test line colour giving 11, 16 and 9 pixels, respectively. The remaining NMs, CNPF8, and the CNPH200, had the largest difference between the background and the test line colour when compared to the others NMs, giving 49 and 23 pixels, respectively. A two-sample Student t-test was performed between the test line and background of all the NMs to see if they are significantly different. Although NMs did not provide any visual difference in the test line and background, the pixel analysis allowed to conclude that NMs had in fact a difference between the test line and the background with a p-value < 0.05, thus are statistical different.

A small pore size in the NM causes a higher capillary flow time, which reduces the wicking time in the NM[126]. This lower wicking time allows a longer interaction between the protein target in the SERS tags and the antibody immobilised in the test line. This group of variables improves the sensitivity of the NM but can also increase the non-specific binding[75]. Accordingly to the supplier[126], to detect malaria, AuNPs in LFA are normally used with a membrane with a pore size of 15 μm, and a wicking time between 90 and 110 s. These parameters are usually employed when the sensitivity is not an issue and the antibody affinity towards the antigen high. Although the pore size usually used by the supplier is 15 μm, the CNPF with pore size 8 μm had the bigger difference of intensity between the background and the test line (49 pixels). The CNPF8 has a wicking time of 180 s and was selected for the remaining optimisations tests, which is a wicking time higher that normally used with AuNPs to detect malaria[126]. Nonetheless, in this assay was used an anisotropic NPs, which can explain the difference when compared with the more isotropic AuNPs.

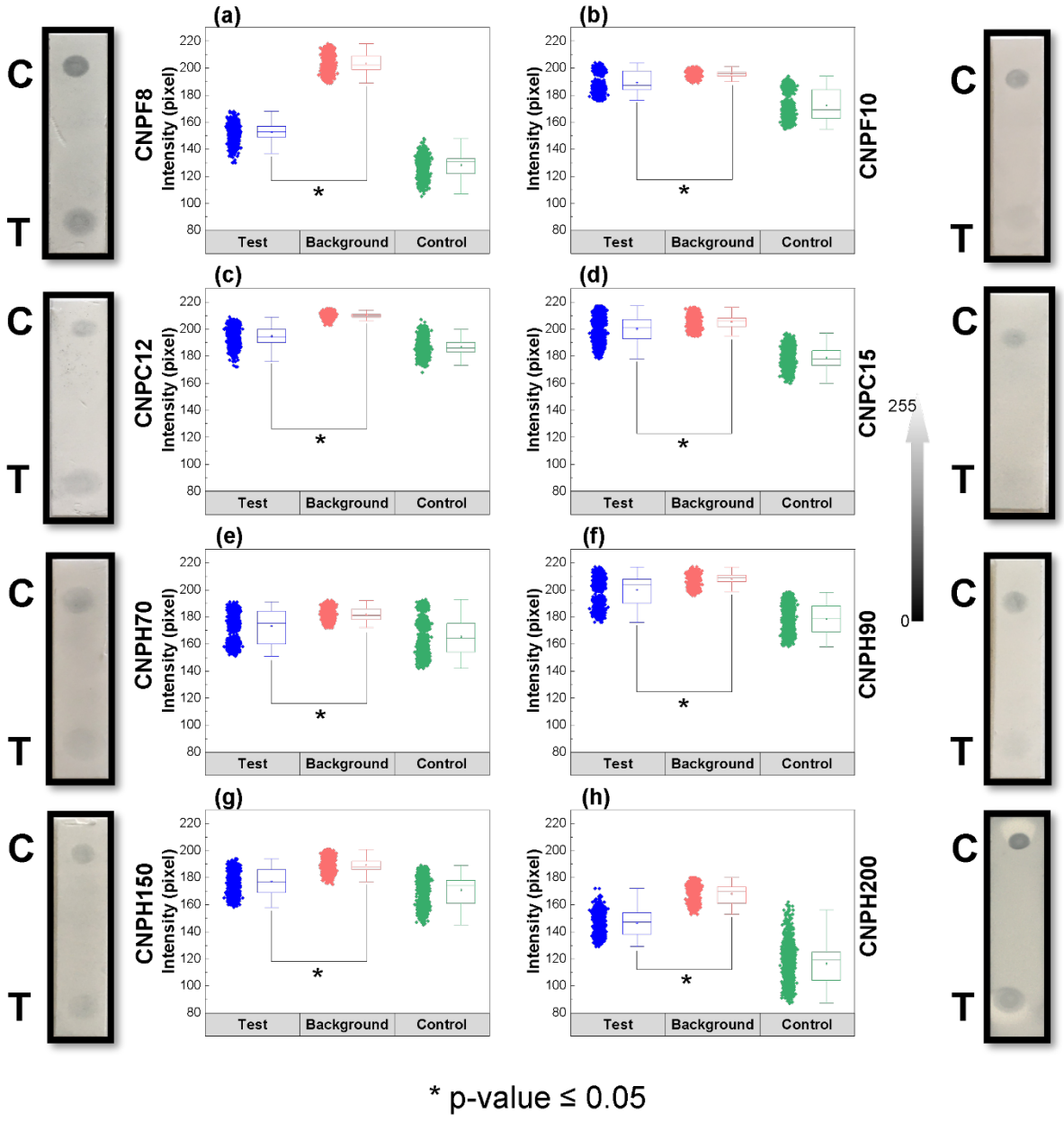

Figure 3.19: Intensity (pixel) of three selected squares in the background, test, and control line for three independent tests for the eight NMs, namely: (a) CNPF8, (b) CNPF10, (c) CNPC12, (d) CNPC15, (e) CNPH70, (f) CNPH90, (g) CNPH150, and (h) CNPH200. The digital pictures of spotted tests in NM are next to the respective graph, where C and T represent the control and test line, respectively. All the analysis of the squares in the test line are represented by blue dots, the background is represented by salmon dots, and the control line are represented by green dots. The box charts correspond to a confidence interval between 25-75%, the line is the median, and the inside box is the mean. The scale of pixels is between 0 (black) and 255 (white). A two-sample Student t-test was performed between all the test lines and the background for each type of NM.

3.7.2 Blocking process in nitrocellulose membrane selection

Simultaneously, the blocking of the NM with skim milk and PBS-T was tested and analysed as described for the selection of NM type, *i.e.*, a higher contrast was our objective. These NMs provided by Advanced Microdevices can be used without any blocking treatment, and it is advised to block the NM when is necessary achieve some requirements, such as stabilising antibodies, and reduce nonspecific interactions, for the assay[126]. The blocking process of the NM can decrease non-specific signals, which depends on the type of NM, the sample, and the antigen captured[75]. Yet, blocking NM require additional reagents, incubations, and drying steps, and can affect the flow of the sample and the reproducibility of the LFA[75].

To perform this selection, all the components (sample pad, conjugate pad, NM, and absorbent pad) were assembled after the anti-Perox and anti-IgG were spotted in the test and control line, respectively. The SERS tags at 1 nM were incubated in the conjugate pad and dried at room temperature for 2 h or at 37ºC inside a desiccator for 1 h. In both cases, the result was the same, the SERS tags seem uncapable to migrate from the conjugate pad, even after an overnight incubation with the sample, as seen in the Figure 3.20. An additional pre-treatment with PBS containing 5% sucrose, 1% BSA and 0.5% tween 20 in the conjugate pad was added to test if the SERS tags could be eluted from the conjugated pad, but the SERS tags remained in the conjugate pad. These results might be related to drying the AuNSs, which may not be functional after replacing the liquid with the sample diluted in potassium phosphate buffer.

In fact, several references describing similar operating systems, do not use the conjugate pad, instead, they mix the sample with the SERS tags, and incubate the complex directly in the sample pad, which is in direct contact with the NM[76,127]. Thus, the conjugate pad was excluded, and the sample was mixed directly into the SERS tags, followed by direct deposition in the sample pad. From this change, the LFA started working correctly, where the SERS tags conjugated with the protein in the sample flow through all the NM, and were immobilised in the test and control line, and so the conjugate pad was eliminated from the LFA assembly.

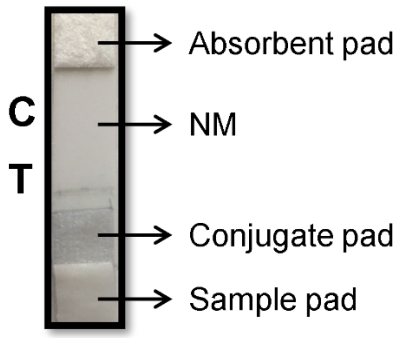

Figure 3.20: Digital pictures LFA with NM of type CNPF8, where C and T represents the control and test line, respectively. The SERS tags in the conjugate pad did not migrate in the NM and did not conjugate in the test and control line.

A CNPF8 membrane was used to evaluate the blocking process. As seen in the Figure 3.21, both the control and test lines have weak intensities in the NM with the blocking process, but in spite of that, the lines are a little distinguished from the background visually. On the other hand, the non-blocked NM resulted in more distinguishable control and test line compared to the blocked NM.

The data of these tests were plotted and compared through the difference in colour intensity of the background and the test line. The blocking process was performed to decrease the non-specific signals and to diminish the colour in the background[75]. For the NM blocked, the difference of intensity between the background and the test line was 8 pixels (Figure 3.21a), and for the NM not blocked was 39 pixels (Figure 3.21b). Thus, the non-blocked NM was chosen since it had higher difference between the test line and background, and no blocking requires less reagents, steps, and consequently less time to perform. This result is in agreement with the results obtained by Tomás *et al.*[71].

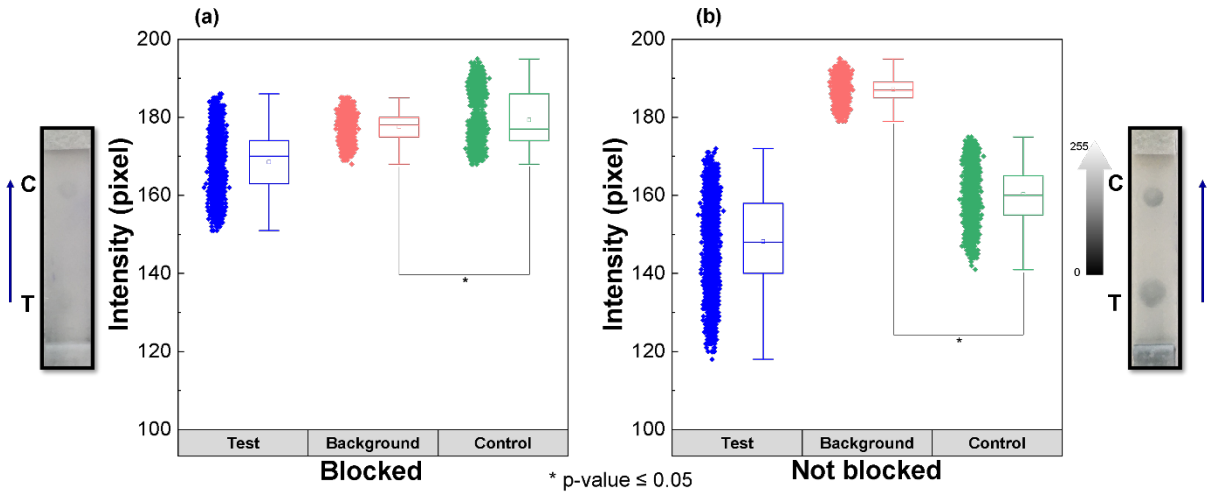

Figure 3.21: Intensity (pixel) of three selected squares in the background, test, and control line for three independent tests for NM type CNPF8. (a) NM blocked with skim milk and PBS-T and dried for 1 h at 37ºC prior deposition of the sample and SERS tags. (b) NM without any blocking treatment. The digital pictures of spotted tests are represented next to the respective graph, with C and T representing the control and test line, respectively. All the analysis of the squares in the test line are

represented by blue dots, the background is represented by salmon dots, and the control line are represented by green dots. The box charts correspond to a confidence interval between 25-75%, the line is the median, and the inside box is the mean. The scale of the pixels is between 0 and 255, corresponding to black and white, respectively. A two-sample Student t-test was performed between the test lines and the background for the NM blocked and NM not blocked.

3.7.3 Selection of an appropriate concentration of SERS tags

To determine which concentration of the SERS tags was enough to ensure detection of a visual signal, two different concentrations of SERS tags were tested, 0.2 and 1 nM. These two SERS tags concentrations were evaluated to verify if was possible to lower the cost of the LFA, since the production of the SERS tags at 1 nM could be a limiting factor. For both concentrations, the test and control line appear in the visual inspection, as shown in the Figure 3.22. The lower concentration used has less colour in the test line than at higher concentrations but can be used as detection and distinction between the background and test lines is still possible.

After plotting the data, a closer analysis regarding the difference between the background and the test line colour was made (Figure 3.22). The most significant difference between the two concentrations of SERS tags was the intensity of the test line. For the highest SERS tags concentration (1 nM), the test line has less intensity, *i.e.*, has a darker colour (Figure 3.22b), with a median of 148 pixels, while at the lowest concentration the test line had a median intensity of 181 pixels (Figure 3.22a). Although with SERS tags at 0.2 nM the colour is noticeably light in the test line, it remains a possibility to use in case of detection of malaria to diminish the cost of LFA. In the remaining optimisations SERS tags at 1 nM was used for better analysis.

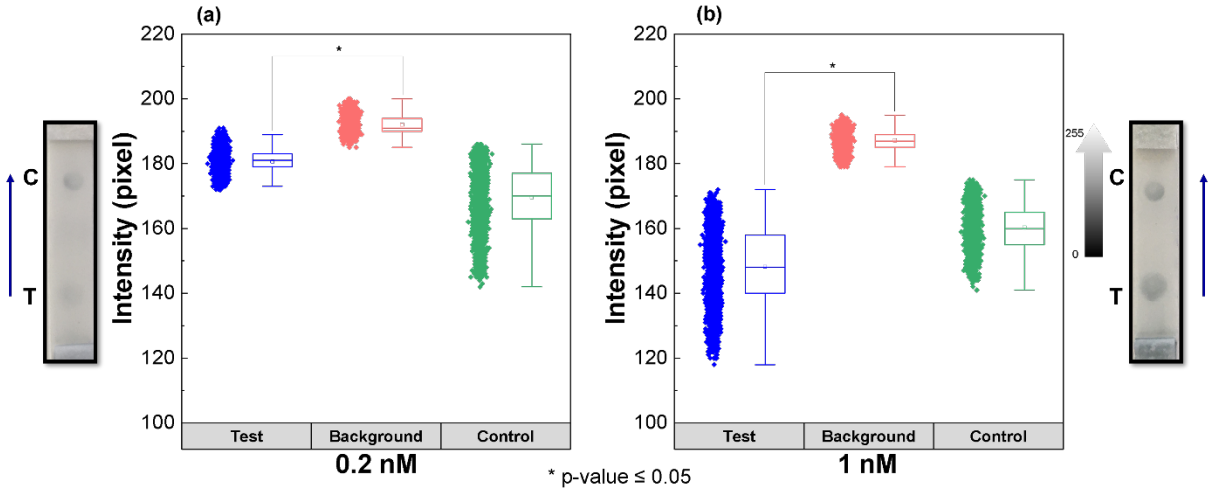

Figure 3.22: Intensity (pixel) of three selected squares in the background, test, and control line for three independent tests. The LFA was assembled with NM (type CNPF8), sample pad (GFB-R7L) and absorbent pad (AP-045). (a) LFA incubated with the sample mixed in 0.2 nM of SERS tags. (b) LFA incubated with a mixing of the sample and the SERS tags at 1 nM.

The digital pictures of LFA are next to the respective graph, with C and T representing the control and test line, respectively. The capillary forces of LFA are represented by a blue arrow. All the analysis of the squares in the test line are represented by blue dots, the background is represented by salmon dots, and the control line are represented by green dots. The box charts correspond to a confidence interval between 25-75%, the line is the median, and the inside box is the mean. The scale of the pixels is between 0 and 255, corresponding to black and white, respectively. A two-sample Student t-test was performed between the test lines and the background for the LFA incubated with SERS tags at 0.2 nM and 1 nM.

3.7.4 Absorbent pad selection

The absorbent pad is used to accumulate the liquid that has crossed the membrane, decreasing the background noise, controlling the volume that goes through the assay and ensuring that the solution flows through the entire strip[75]. In this study, all the LFA components were assembled with two different absorbent pads (AP-045 and AP-080). The LFA test with the absorbent pad AP-080 demonstrate more background noise than AP-045 by visual inspection, as shown in the Figure 3.23.

By analysing the plots, the background in the LFA test with the absorbent pad AP-080 has lower intensity (darker colour) (Figure 3.23b) than with the AP-045 (Figure 3.23a). The intensity difference between the background and the test line was slightly lower when AP-045 (39 pixels) was used, than AP-080 (43 pixels). For a better analysis, the background must have a light colour, *i.e.*, high intensity nearly white, to thereby have a more distinguishable test line. The absorption pad AP-045 with 0.4 mm of thickness cannot absorb liquid as much as the absorption pad AP-080 (with 0.9 mm of thickness). For this amount of sample, the absorbent pad AP-045 was chosen, due to the lighter background and for having a more easily visually distinguishable test line.

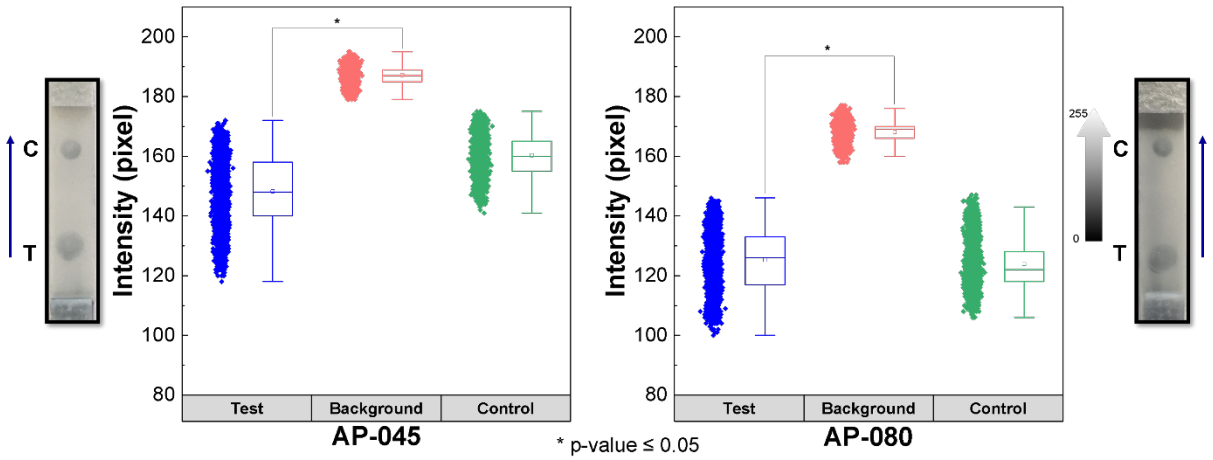

Figure 3.23: Intensity (pixel) of three selected squares in the background, test, and control line for three independent tests. The LFA was assembled with NM (type CNPF8) and sample pad (GFB-R7L). (a) LFA assembled with the absorbent pad AP-045. (b) LFA assembled with the absorbent pad AP-080. The digital pictures of LFA are represented next the respective graph, with C and T representing the control and test line, respectively. The capillary forces of LFA are represented by a blue

arrow. All the analysis of the squares in the test line are represented by blue dots, the background is represented by salmon dots, and the control line are represented by green dots. The box charts correspond to a confidence interval between 25-75%, the line is the median, and the inside box is the mean. The scale of the pixels is between 0 and 255, corresponding to black and white, respectively. A two-sample Student t-test was performed between the test lines and the background for the LFA assembled with AP-045 and AP-080.

3.7.5 Control and test line dilution selection

Several concentrations of anti-IgG and anti-Perox were tested, for the control and test line, respectively, to determine the lowest concentration that can be used for reducing costs of LFA. For the test line, the colour of the test line with anti-Perox, was evaluated by ImageJ software. The darker colour, *i.e.*, lower intensity of the zone analysed, indicates that a higher amount of SERS tags with the antigen are immobilised in the test line. For the control line, the analysis was similar but the SERS tags without protein are immobilised in the control line.

In the control line, four different dilutions were tested from 0.5 to 0.005 $mg{\cdot}mL^{-1}$ of anti-IgG with Tris buffer while maintaining the test line with anti-Perox at 9 $mg{\cdot}mL^{-1}$. In Figure 3.24b, the control line is visible only in the lower dilution, *i.e.*, 0.5 $mg{\cdot}mL^{-1}$ of anti-IgG. Although the remaining tests have high background noise and high intensity in the test line colour (*i.e.*, light colour), the objective was to detect the conjugation in the control line of these LFA tests. The data obtained by ImageJ through these digital pictures were plotted to compare the difference of intensity between the background and the control line (Figure 3.24). The control line, anti-IgG at 0.5 $mg{\cdot}mL^{-1}$, was the only condition to provide a difference from the background (27 pixels). Therefore, lower concentrations cannot be used, although the intensity of backgrounds of LFA tests varies between the several concentrations of anti-IgG tested, the control line dilution chosen anti-IgG at 0.5 $mg{\cdot}mL^{-1}$ (Figure 3.24b). Other authors[128,129], have reported a higher concentration of anti-IgG (1 $mg{\cdot}mL^{-1}$), which the host are the same used in this Thesis, *i.e.*, mouse host.

Different dilutions, from 9 to 0.009 $mg{\cdot}mL^{-1}$, of anti-Perox in the test line were assessed, using a control line with anti-IgG at 0.5 $mg{\cdot}mL^{-1}$. In four different LFA, a visual inspection was carried out, as it seen in the Figure 3.24a, and all LFA tests except one has a spot colour in the test line. The difference of intensity between the background and the test line is not significant at the lowest anti-Perox concentration tested (0.009 $mg{\cdot}mL^{-1}$ of anti-Perox), 6 pixels, in comparison with the concentration 0.09 $mg{\cdot}mL^{-1}$ of anti-Perox (19 pixels). With increasing anti-Perox concentration the difference of intensity of background and test line increases (Figure 3.24a). The lowest concentration that can be used and seen visually in the test line is 0.09 $mg{\cdot}mL^{-1}$. Parolo *et al.*[75], recommended higher, optimised concentrations of antibody immobilised in the test line to maximise the chances of the sandwich for-

mation. For this reason, a concentration of 0.9 mg·mL^{-1} of anti-Perox was chosen to immobilise in the test line for further testing.

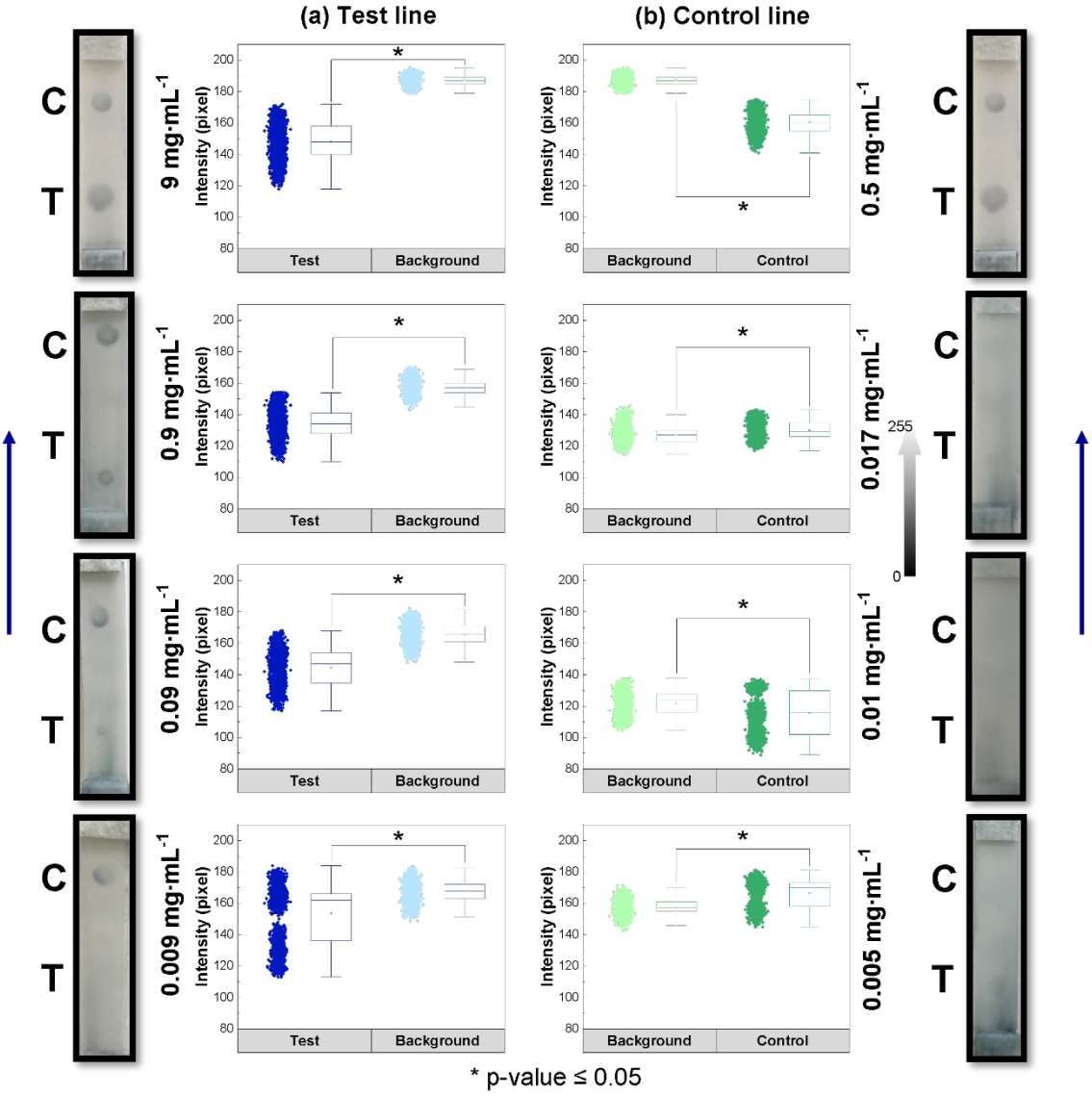

Figure 3.24: Intensity (pixel) of three selected squares in the background, test, and control line for three independent tests. The LFA was assembled with NM (type CNPF8), sample pad (GFB-R7L), and absorbent pad (AP-045). (a) Comparison of intensities between the test line and background, with several concentrations of anti-Perox immobilised in the test line. The dilutions tested were from 9 to 0.009 mg·mL^{-1}. (b) Several concentrations of anti-IgG tested, from 0.5 to 0.005 mg·mL^{-1}, in the control line. Each graph compares the intensity of the background to the control line, where is immobilised the corresponding anti-IgG concentration. The digital pictures of LFA are represented next to the respective graph, with C and T representing the control and test line, respectively. The capillary forces of LFA are represented by a blue arrow. All the analysis of the squares in the test line are represented by blue dots, the control line is represented by green dots, and the background is represented by lighter colours that correspond to control and test line. The box charts correspond to a confidence interval between 25-75%, the line is the median, and the inside box is the mean. The scale of the pixels is between 0 and 255, corresponding to black and white, respectively. A two-sample Student t-test was performed between the test lines and the corresponding background for the anti-Perox dilutions tested and between the control lines and the corresponding background for the different anti-IgG dilutions.

3.7.6 Sensitivity tests

All LFA tests were assembled with the NM type CNPF8 not blocked, the sample pad GFB-R7L and the absorbent pad AP-045, excluding the conjugate pad, which the sample was mixed with the SERS tags at 1 nM. Several concentrations, from 0.01 to 100 µg·mL^{-1}, of Perox were tested where anti-Perox at 0.9 mg·mL^{-1} and anti-IgG at 0.5 mg·mL^{-1} were immobilised in the test and control line, respectively. As can be seen in Figure 3.25, all the LFA tests had a similar colour in the control line, and the background intensity varies randomly with the concentration of Perox in the sample. Due to this darker background in the LFA tests, no significant difference was observed for decreasing concentrations of Perox (Figure 3.25).

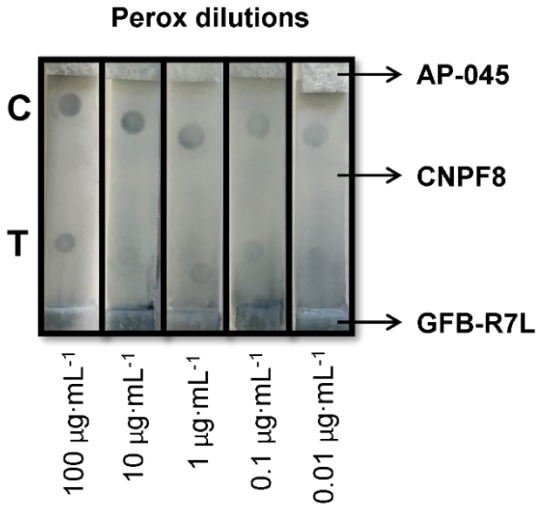

Figure 3.25: Digital pictures of LFA, where the C and T represents the control and test line, respectively. The absorbent pad, NM, and sample pad used were AP-045, CNPF8, and GFB-R7L, respectively. In the control and test line anti-IgG at 0.5 mg·mL^{-1} and anti-Perox at 0.9 mg·mL^{-1} were immobilised. Several concentrations of Perox from 0.01 µg·mL^{-1} to 100 µg·mL^{-1} were tested. The digital pictures are shown in decreasing concentrations, from the left to the right.

The median peak intensity of the background obtained through the ImageJ software was subtracted to the intensity of the test line, to all the LFA tests. These data were plotted versus the target analyte (Perox) concentration used, as represented in the Figure 3.26. Accordingly to Parolo *et al.*[75], the signal in the test line of a non-competitive assay increases proportionally with the concentration of the protein in the sample, *i.e.*, the darker colour in the test line more protein is present in the sample[75]. Thus, there are an initial part of concentration dependence that is linear. For this reason, more samples with lower concentrations of Perox is needed to test, since with these chosen points it cannot see this linearity. Similar to other authors[76], the data was fitted to a Langmuir isotherm model, where it is preferred to competitive assays, but can be used in sandwich assays since at lower concentrations is linear[75].

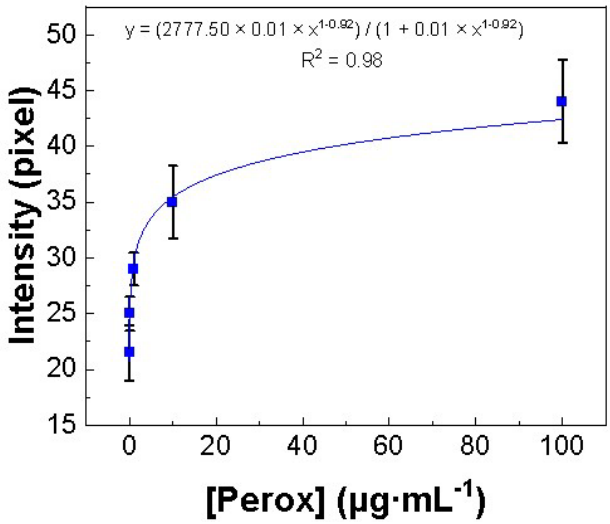

Figure 3.26: Intensity obtained by subtracting the peak intensity of the test line from the background intensity versus the Perox concentration used. Langmuir isotherm model fitting to the data. The error bars represent the standard deviation of triplicate measurements (median ± SD).

As seen in the Figure 3.26, at lower concentration of Perox in LFA, the intensity of difference between the background and the test line is higher than 0 pixels and it is possible to see at naked eye the test line, as well as at 0 µg·mL^{-1} the intensity is higher than 0 pixels. Although LFA has high intensity between the background and the test line at low Perox concentration, these results are promising for using this LFA with *Pf*HRPII-anti-*Pf*HRPII. This fitting allowed the determination of the LOD, calculated through the difference between the intensity of the background and the test line of the blank sample sum three times its standard deviation, and the limit of quantification (LOQ), calculated through the same intensity of the blank sample sum ten times its standard deviation. Thereby, the LOD and LOQ was determined as 5.24 and 7.28 µg·mL^{-1}, respectively. In comparison, Sánchez-Purrà *et al.*[76] had obtained a much lower LOD value by using similar SERS tags for Zika (0.72 ng·mL^{-1}) and Dengue (7.67 ng·mL^{-1}). More optimisations are necessary to obtain a more reliable LFA and with lower LOD and LOQ values.

3.7.7 Raman and SERS measurements

To prove if this LFA was reliable to use for detection of malaria, the recombinant *Pf*HRPII previously purified as described in section 3.1.2 was used. For that, nine LFA tests with varying concentrations of *Pf*HRPII (from 0 ng·mL^{-1} to 50 ng·mL^{-1}) were prepared. The Raman spectrum of NM and the SERS spectrum of the SERS tags were analysed and used as standards. As observed in Figure 3.27, MBA conjugated in the SERS tags has two main vibrational lines at 1079 cm^{-1} and 1587 cm^{-1} (Table 3.2), these values are shifted to lower energy in relation to the Raman spectrum (1099 cm^{-1} and

1595 cm^{-1}) as some authors observed. A possible explanation for the observed shifts can be related to the fact that these molecules are not bound through a thiol group in the SERS tags[130]. As described by other authors[131,132], NM has several strong bands at 1121 cm^{-1}, 1290 cm^{-1} and 1376 cm^{-1}, which is similar to what was detected in the Raman spectrum obtained (Table 3.2) (Figure 3.27).

Table 3.2: Vibrational lines assignment for SERS spectrum of MBA and for Raman spectra of nitrocellulose[131–133].

Wavenumber (cm^{-1})	Strength	Assignment (vibration)	Origin	Reference
MBA				
1079	Strong	Aromatic ring vibrations	SERS (SERS tags-MBA)	133
1587	Strong	Aromatic ring vibrations	SERS (SERS tags-MBA)	133
Cellulose				
1122	Weak	Stretching	Raman (NM)	131,132
1283	-	HCC and HCO bending	Raman (NM)	131,132
1369	Strong	HCC, HCO, and HOC bending	Raman (NM)	131,132

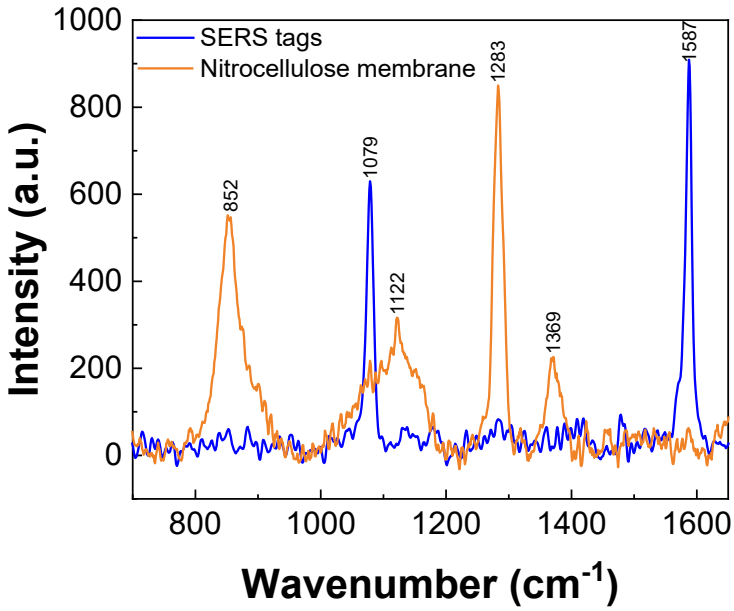

Figure 3.27: (Blue line) SERS spectrum of the SERS tags, possessing the Raman probe MBA. Two main vibrational lines can be detected at 1079 cm^{-1} and 1587 cm^{-1}, assigned to aromatic ring vibrations (see Table 3.2). (Orange line) Raman spectrum of NM, which has a particular intense vibrational line at 1283 cm^{-1}, assigned to HCC and HCO bending of cellulose molecules (see Table 3.2).

Two LFAs were prepared with anti-*Pf*HRPII immobilised in three different spots in NM. Two samples with 0 and 50 ng·mL^{-1} of recombinant *Pf*HRPII mixed with SERS tags at 0.2 nM were incubated in each LFA, as seen in the Figure 3.28b and c. A SERS map was performed in the test line and background, in triplicate for each sample. During this analysis, the direct classical least squares (DCLS) method was used, which can isolate each component signal from each pixel present in a complex mixture with overlapped peaks. Individual SERS tag and NM spectra were used as references to a DCLS analysis which resulted in a SERS map that identified the contributions of SERS tag and NM in each pixel[134,135]. For this analysis, a Raman map of the background after the incubation without the recombinant *Pf*HRPII was performed and analysed to be possible to identify the positive signal of MBA in the surface of AuNSs in the test lines, *i.e.*, a threshold was determined. A threshold value of 1.317 component coefficient was established, where above this value 95% confidence is considered a positive sample, which had the purpose of determine the recombinant *Pf*HRPII immobilised in the test line, as seen in the Figure 3.28a. In the test line, SERS tags were identified through DCLS method, which at higher DCLS score, more intense is the blue colour. In the LFA tests, incubated without and with 50 ng·mL^{-1} of recombinant *Pf*HRPII, was identified SERS tags and NM (Figure 3.28b and c, orange map).

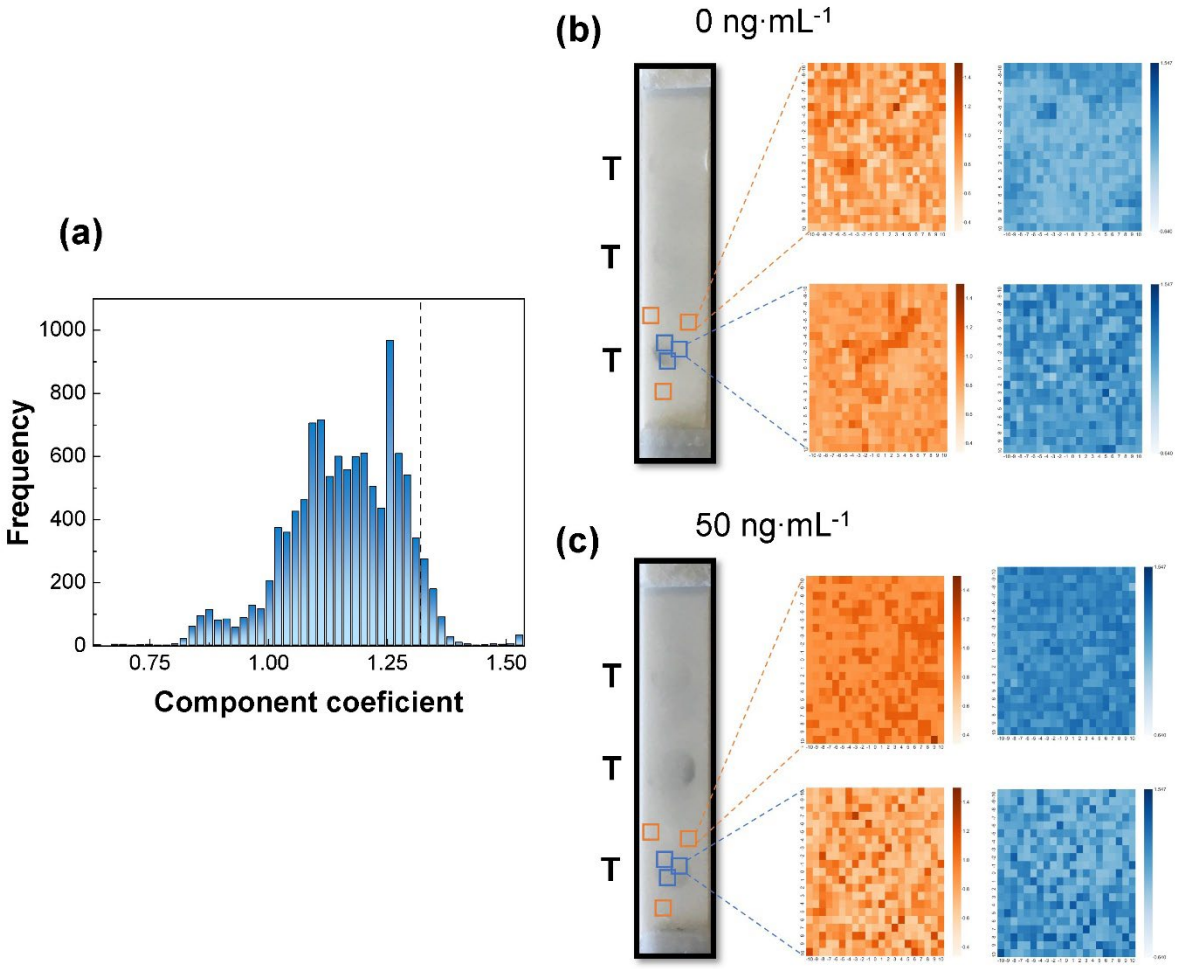

Figure 3.28: Data treatment of the results of both LFA incubated with 0 and 50 ng·mL^{-1} of recombinant *Pf*HRPII mixed with SERS tags at 0.2 nM. (a) Histogram of component coefficient frequencies for the background of LFA. The dashed line represents the 1.317 component coefficient, which is the threshold for the positive detection of LFA. (b) Pixelated SERS tags map (blue) and Raman map NM (orange) of LFA incubated without recombinant *Pf*HRPII. (c) Pixelated SERS tags map (blue) and Raman map NM (orange) of LFA incubated with 50 ng·mL^{-1} of recombinant *Pf*HRPII.

The LFA test incubated with 50 ng·mL^{-1} of recombinant *Pf*HRPII must have more SERS tags identified than a LFA test without recombinant *Pf*HRPII, *i.e.*, higher DLCS counts. However, this analysis demonstrated that the control had identical intense colour in SERS map than with higher concentration of recombinant *Pf*HRPII, *i.e.*, in the test line of the LFA without recombinant *Pf*HRPII a higher concentration of this protein was identified that in the LFA test incubated with 50 ng·mL^{-1}. As seen in Figure 3.29, the DCLS score between the LFA incubated with 50 ng·mL^{-1} (1.16 ± 0.12 DCLS score) and without recombinant *Pf*HRPII (1.14 ± 0.13 DCLS score) have a small, but significant difference (p-value < 0.01), since this difference is within the standard deviation. Supposedly, the LFA incubated with the protein should have a higher DCLS score than the LFA without protein.

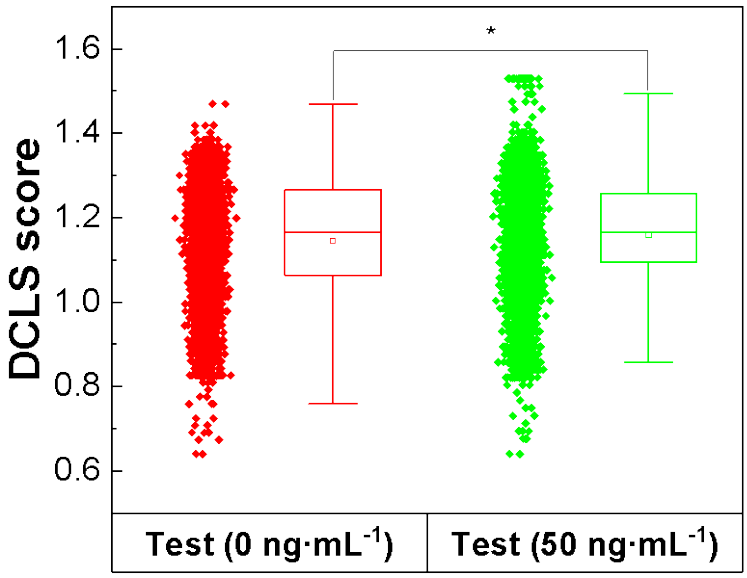

Figure 3.29: The DCLS score of two LFA tests, incubated with 50 ng·mL^{-1} of recombinant *Pf*HRPII and a negative control (without *Pf*HRPII). The negative test, *i.e.*, without recombinant *Pf*HRPII is represented by red dots and the positive test (50 ng·mL^{-1} of recombinant *Pf*HRPII) is represented by green dots. The box charts correspond to a confidence interval between 25-75%, the line is the median, and the inside box is the mean. A two-sample Student t-test was performed between these two LFA, * p-value < 0.01.

A good LFA must have repeatability, replicability and reproducibility, and an automated disposing of the lines tests into the NM are fundamental to the reproducibility of the LFA, due to the control in the flow rate and speed[75]. During the analysis of LFA tests, differences of background colour between tests were noticeable. Besides, a LFA test without any protein was supposed to not have any signal visual, and lowest SERS signal, which was not seen due to unspecified interactions in the test line. This conjugation between the test line and the SERS tags can possibly be avoided by washing the LFA with washing buffers, such as phosphate buffer or PBS with 0.1% (v/v) of tween 20, after the SERS tags incubation as some authors reported to eliminate unbound conjugates and can decrease the background[75,76,136]. This could be an explanation why the DCLS scores were higher with no recombinant *Pf*HRPII. More optimisation is needed to construct a working SERS-based LFA for malaria antigen detection.

4

CONCLUSION AND FUTURE PERSPECTIVES

4.1 Conclusion

A SERS-based LFA was developed to detect a biomarker of malaria, *Pf*HRPII, which is highly expressed during malaria blood stage infection. A recombinant form of this biomarker was easily produced in *E. coli* BL21/DE3 containing a pET-15b vector overexpressing the protein containing a His-tag, allowing its purification using a Ni-NTA column. Protein quality was assessed by SDS-PAGE, and western blot was performed to confirm the protein identity. Several optimisations of the western blot protocol were performed with a Perox-anti-Perox complex to infer the primary and secondary antibody minimal concentration needed for an observable detection of the colour by the oxidation of the peroxidase substrate (TMB), thus reducing the western blot costs. The optimised concentrations were: Perox at 20 $\mu g \cdot mL^{-1}$; primary antibody at 6 $\mu g \cdot mL^{-1}$; and secondary antibody at 0.125 $\mu g \cdot mL^{-1}$. An SDS-PAGE of the purified solution had two main bands, at 67 and 22 kDa. The western blot confirmed that the band at 67 kDa of MW, was in fact the recombinant *Pf*HRPII. The band at 22 kDa of MW did not reveal any colour, which was indicative of a contaminant that has some affinity to the Ni-NTA resin[23]. This western blot was performed using anti-*Pf*HRPII at 0.6 $\mu g \cdot mL^{-1}$ as primary antibody, and the secondary antibody at 0.125 $\mu g \cdot mL^{-1}$. The pixel bands intensities of the SDS-PAGE were measured corresponding 27% to the recombinant *Pf*HRPII and 73% to the contaminants. Considering the 27% from the SDS-PAGE, the final concentration of recombinant *Pf*HRPII was determined as 0.12 ± 0.03 $mg \cdot mL^{-1}$ by applying the BCA method to whole protein determination.

The other components that comprise the SERS-based LFA in the sandwich format were developed. Namely, SERS tags (*i.e.*, AuNSs-MBA-EDC/SNHS-anti-Perox-BSA) were developed, where anti-Perox and Perox were used to reduce costs. Gold nanostars, synthesised from spherical gold nanoparticles, using a protocol described in the literature[66]. These gold nanostars were functionalised with MBA, conjugated with a specific antibody to detect an antigen, and blocked with BSA to avoid non-specific interactions. A series of tests, such as DLS, UV-Vis, agarose gel electrophoresis (AGE), and enzymatic activity assay of peroxidase, were performed to construct a stable SERS tags, where the covalent conjugation, which provides a stronger bond between the AuNSs-MBA and the antibodies[70], was chosen using a linker, EDC/SNHS, for coupling. The confirmation of SERS tag formation was assessed by DLS whereby the addition of anti-Perox antibodies to AuNSs-MBA resulted in an increase of the hydrodynamic diameter. Nevertheless, further addition of BSA for blocking did not result in an increased hydrodynamic diameter. Such observation might be explained by BSA blocking the interstices that lack anti-Perox molecules. Furthermore, SERS tag development was followed by UV-Vis, where the addition of antibodies and proteins to AuNSs-MBA resulted in a LSPR red shift, confirming the bioconjugation.

A simulation of the sandwich immunoassay was performed by using these SERS tags, the Perox antigen and the anti-Perox to "close the sandwich". AGE assays, showed that SERS tags-Perox-anti-Perox had all the molecules bound, proving that the simulated immunocomplex works and can be used in the LFA, since the anti-Perox in the SERS tags surface recognised the Perox added, forming a sandwich with the anti-Perox added lastly. SERS tags-anti-Perox do not bound the anti-Perox at the SERS tags surface, since the Perox is absent and the anti-Perox in the SERS tags cannot be bound, making this the negative control. The AGE technique also proved that this conjugation was successful by less electrophoretic mobility of this sample in comparison with the negative control. An enzymatic activity assay of Perox was also performed with these samples, which confirm if the anti-Perox could recognise the antigen properly by measuring the activity of peroxidase bounded, which was confirmed. Since this Thesis was focused on the incubation of SERS tags with a blood sample, which contains salt (154 mM NaCl in a healthy person), the CCC value of the SERS tags was determined as ≈ 200 mM. Hence, the SERS tags can be used in an LFA test. Successful conjugation was also confirmed by the CCC value observed for each stage of the bioconjugation being higher than the one who proceeded it, *i.e.,* the CCC value of the AuNSs-MBA-EDC/SNHS-anti-Perox-BSA (SERS tag) was higher than the CCC value obtained for AuNSs-MBA-EDC/SNHS-anti-Perox which was higher than the CCC for AuNSs-MBA. Thus, the increase value of CCC results from the addition of antibodies and proteins to the AuNSs-MBA surface, which creates a higher stability.

Regarding the SERS-based LFA several optimisations of the components were made to select the LFA with the best performance, *i.e.,* allowing a higher reliable colour detection. In these optimisations, Perox was used as the model antigen to be detected by the respective antibody, thus reducing optimisation costs. The Perox-optimised LFA, can then serve as a starting point for a LFA based on the recombinant *Pf*HRPII and its respective antibody. The selection process of every optimisation was based on the difference of intensity between the background and the test line, as analysed by ImageJ. The conjugate pad was excluded due to the inability to release the SERS tags to migrate into the NM after introducing the sample. Thus, the sample was mixed into the SERS tags and deposited directly in the sample pad. The sample pad GFB-R7L was chosen in the prior work of Tomás *et al.*[71] and the NM type CNPF8 not blocked and blocked, since this last is only recommended to achieve assay requirements, were compared and the not blocking process was selected through ImageJ. The absorbent pad AP-045, and a concentration of 0.9 $mg \cdot mL^{-1}$ in the test line and 0.5 $mg \cdot mL^{-1}$ in the control line, for the anti-Perox and anti-IgG, respectively, were also selected. Followed the LFA optimisation, the sensitivity of the LFA was tested using Perox with a concentration range of 0.01 to 100 $\mu g \cdot mL^{-1}$. Since this is a non-competitive assay, the signal in the test line increases proportionally with the concentration of the protein in the sample[75], and the data were fitted to a Langmuir isotherm model. At lower concen-

tration of Perox (0.01 $\mu g \cdot mL^{-1}$), the visual signal in the test line was higher than expected (21.5 pixels). The LOD and LOQ were also determined as 5.24 and 7.28 $\mu g \cdot mL^{-1}$, respectively.

Afterwards, two SERS-based LFA to detect malaria were performed, with a concentration of 50 $ng \cdot mL^{-1}$ of recombinant *Pf*HRPII and compared with a control (0 $ng \cdot mL^{-1}$ of recombinant *Pf*HRPII). The analysis of the SERS maps revealed that the LFA test with 50 $ng \cdot mL^{-1}$ had an identical DCLS score in the SERS map and less colour at naked eye when compared to the assay without recombinant *Pf*HRPII. Supposedly, LFA test without any protein would not have any visual signal, and low DCLS scores, which did not happen due to non-specific interactions in the test line. Hence, more optimisations tests are needed, but the work presented in this Thesis proves that this SERS-based LFA has the possibility to detect malaria through the biomarker *Pf*HRPII.

4.2 Future perspectives

To have a more reliable LFA, more optimisations are needed regarding the purification of the recombinant *Pf*HRPII, where it is necessary to obtain a constant amount of recombinant *Pf*HRPII per liter of culture, as compared to other works[22]. The contaminants in the solution purified were much higher than the protein, whereupon some optimisations could be achieved by varying reagents and their quantity during the purification process to obtain more recombinant *Pf*HRPII concentration per liter of culture and with less contaminants[22].

The NMs used in the LFA can be blocked to achieve goals such as stabilising antibodies and reducing nonspecific interactions[126]. The blocking process performed could be tested in Raman and compared to the NM without any blocking treatment for further knowledge regarding nonspecific interactions in the background of the LFA, or even try different blocking treatments, such as BSA (1-2% w/v), IgG (1-2% w/v), gelatine (0.1-0.5% w/v), casein (1-2% w/v), polyvinylpyrrolidone (0.5-1% w/v) or polyvinyl alcohol (0.1-1% w/v), whereupon the choice depends on the type of NM, the sample and the antibody bioreceptor[75].

The sensitivity tests performed fitted in a Langmuir model, but at lower concentrations of Perox, are supposed to be linear due to the dependence in this sandwich assay[75]. Although a linear trend was obtained at low Perox concentrations (from 0.01 to 100 $\mu g \cdot mL^{-1}$), this linear trend can be improved by performing more samples with low Perox concentrations between 0 and 10 $\mu g \cdot mL^{-1}$. The values of LOD and LOQ can also be improved with the optimisations described.

The sensitivity of this LFA assay is limited by the dissociation constant of the equilibrium between recombinant *Pf*HRPII and the conjugated anti-*Pf*HRPII[74]. The recombinant *Pf*HRPII purified in this Thesis had a high percentage of contaminant proteins (73%). Due to this, an AGE should have

been ran to determine the dissociation constant by using this recombinant *Pf*HRPII fraction, which has high percentage of contaminants.

The various LFA tests performed exhibited some differences, especially, the background colour was not always consistent between the triplicates. An additional optimisation is needed to construct a more reproducible LFA, such as a washing step with phosphate buffer or PBS with 0.1% (v/v) of tween 20 after the addition of the SERS tags mixed with the sample, that could eliminate nonspecific interactions in the test line[75,76,136], which was observed by a positive signal in a test line of a LFA without antigen (negative control). This optimisation can result in a more reliable LFA with fewer non-specific interactions and lower background colour. Additionally, another absorbent pad optimisation is required because more liquid will be added to the LFA. Furthermore, using automated dispensers in the test and control line immobilisation allows to control the flow rate and the speed of deposition, which could lead to a more reproducible LFA[75].

REFERENCES

1. Nghochuzie NN, Olwal CO, Udoakang AJ, Amenga-Etego LNK, Amambua-Ngwa A. Pausing the Fight Against Malaria to Combat the COVID-19 Pandemic in Africa: Is the Future of Malaria Bleak? *Front Microbiol*. 2020;11(June):1-5. doi:10.3389/fmicb.2020.01476
2. Health Organization W. *World Malaria Report 2021*.; 2021.
3. Sherman IW. Biochemistry of Plasmodium (malarial parasites). *Microbiol Rev*. 1979;43(4):453-495. doi:10.1128/mmbr.43.4.453-495.1979
4. Lee H, Halverson S, Ezinwa N. Mosquito-Borne Diseases. *Prim Care - Clin Off Pract*. 2018;45(3):393-407. doi:10.1016/j.pop.2018.05.001
5. Azikiwe C, Ifezulike C, Siminialayi I, Amazu L, Enye J, Nwakwunite O. A comparative laboratory diagnosis of malaria: microscopy versus rapid diagnostic test kits. *Asian Pac J Trop Biomed*. 2012;2(4):307-310. doi:10.1016/S2221-1691(12)60029-X
6. Cowman AF, Healer J, Marapana D, Marsh K. Malaria: Biology and Disease. *Cell*. 2016;167(3):610-624. doi:10.1016/j.cell.2016.07.055
7. Poti KE, Sullivan DJ, Dondorp AM, Woodrow CJ. HRP2: Transforming Malaria Diagnosis, but with Caveats. *Trends Parasitol*. 2020;36(2):112-126. doi:10.1016/j.pt.2019.12.004
8. Bartoloni A, Zammarchi L. Clinical aspects of uncomplicated and severe malaria. *Mediterr J Hematol Infect Dis*. 2012;4(1). doi:10.4084/MJHID.2012.026
9. Doolan DL, Dobaño C, Baird JK. Acquired Immunity to Malaria. *Clin Microbiol Rev*. 2009;22(1):13-36. doi:10.1128/CMR.00025-08
10. Okwa O. *Malaria Parasites*. (Okwa O, ed.). InTech; 2012. doi:10.5772/1477
11. Ragavan K V., Kumar S, Swaraj S, Neethirajan S. Advances in biosensors and optical assays for diagnosis and detection of malaria. *Biosens Bioelectron*. 2018;105(November 2017):188-210. doi:10.1016/j.bios.2018.01.037

12. Kilejian A. A unique histidine rich polypeptide from the malaria parasite, Plasmodium lophurae. *J Biol Chem*. 1974;249(14):4650-4655. doi:10.1016/s0021-9258(19)42468-x

13. Panton LJ, McPhie P, Lee Maloy W, Wellems TE, Taylor DW, Howard RJ. Purification and partial characterization of an unusual protein of Plasmodium falciparum: histidine-rich protein II. *Mol Biochem Parasitol*. 1989;35(2):149-160. doi:10.1016/0166-6851(89)90117-5

14. Singh B, McCaffery JN, Kong A, et al. Purification of native histidine-rich protein 2 (nHRP2) from Plasmodium falciparum culture supernatant, infected RBCs, and parasite lysate. *Malar J*. 2021;20(1). doi:10.1186/s12936-021-03946-1

15. Sullivan DJ, Gluzman IY, Goldberg DE. Plasmodium hemozoin formation mediated by histidine-rich proteins. *Science (80-)*. 1996;271(5246):219-222. doi:10.1126/science.271.5246.219

16. Schneider EL, Marletta MA. Heme binding to the histidine-rich protein II from Plasmodium falciparum. *Biochemistry*. 2005;44(3):979-986. doi:10.1021/bi048570p

17. Das P, Grewal JS, Chauhan VS. Interaction of Plasmodium falciparum histidine-rich protein II with human lymphocytes leads to suppression of proliferation, IFN-γ release, and CD69 expression. *Parasitol Res*. 2006;100(1):39-50. doi:10.1007/s00436-006-0228-6

18. Ndonwi M, Burlingame OO, Miller AS, Tollefsen DM, Broze GJ, Goldberg DE. Inhibition of antithrombin by Plasmodium falciparum histidine-rich protein II. *Blood*. 2011;117(23):6347-6354. doi:10.1182/blood-2010-12-326876

19. Sahdev S, Khattar SK, Saini KS. Production of active eukaryotic proteins through bacterial expression systems: A review of the existing biotechnology strategies. *Mol Cell Biochem*. 2007;307(1-2):249-264. doi:10.1007/s11010-007-9603-6

20. Khow O, Suntrarachun S. Strategies for production of active eukaryotic proteins in bacterial expression system. *Asian Pac J Trop Biomed*. 2012;2(2):159-162. doi:10.1016/S2221-1691(11)60213-X

21. Burgess R, Deutscher M. Methods in Enzymology, Guide to Protein Purification. In: Burguess R, Deutscher M, eds. 2nd Editio. Academic Press; 2009. doi:10.1016/S0076-6879(09)63045-7

22. Spriestersbach A, Kubicek J, Schäfer F, Block H, Maertens B. Purification of His-Tagged Proteins. *Methods Enzymol*. 2015;559:1-15. doi:10.1016/bs.mie.2014.11.003

23. Crowe J, Döbeli H, Gentz R, Hochuli E, Stüber D, Henco K. 6xHis-Ni-NTA Chromatography as a Superior Technique in Recombinant Protein Expressiod/Purification. In: *Protocols for Gene Analysis*. Vol 31. Humana Press; 1994:371-388. doi:10.1385/0-89603-258-2:371

24. Magdeldin S, Moser A. Affinity Chromatography: Principles and Applications. *Affin Chromatogr*. Published online 2012. doi:10.5772/39087

25. Crowe J, Masone BS, Ribbe J. One-Step Purification of Recombinant Proteins with the 6xHis Tag and Ni-NTA Resin. In: *Basic DNA and RNA Protocols*. Vol 58. Humana Press; 1995:491-510. doi:10.1385/0-89603-402-X:491

26. Moody A. Rapid Diagnostic Tests for Malaria Parasites. *Clin Microbiol Rev*. 2002;15(1):66-78. doi:10.1128/CMR.15.1.66-78.2002

27. Jain P, Chakma B, Patra S, Goswami P. Potential biomarkers and their applications for rapid and reliable detection of malaria. *Biomed Res Int*. 2014;2014. doi:10.1155/2014/852645

28. Keough DT, Ng AL, Winzor DJ, Emmerson BT, De Jersey J. Purification and characterization of Plasmodium falciparum hypoxanthine-guanine-xanthine phosphoribosyltransferase and comparison with the human enzyme. *Mol Biochem Parasitol*. 1999;98(1):29-41. doi:10.1016/S0166-6851(98)00139-X

29. Rodríguez-Acosta A, Domínguez NG, Aguilar I, Girón ME. Characterization of Plasmodium falciparum glutamate dehydrogenase-soluble antigen. *Brazilian J Med Biol Res*. 1998;31(9):1149-1155. doi:10.1590/S0100-879X1998000900008

30. Bronzan RN, McMorrow ML, Patrick Kachur S. Diagnosis of Malaria. *Mol Diagn Ther*. 2008;12(5):299-306. doi:10.1007/BF03256295

31. Tangpukdee N, Duangdee C, Wilairatana P, Krudsood S. Malaria diagnosis: A brief review. *Korean J Parasitol*. 2009;47(2):93-102. doi:10.3347/kjp.2009.47.2.93

32. Johnston SP, Pieniazek NJ, Xayavong M V., Slemenda SB, Wilkins PP, Da Silva AJ. PCR as a confirmatory technique for laboratory diagnosis of malaria. *J Clin Microbiol*. 2006;44(3):1087-1089. doi:10.1128/JCM.44.3.1087-1089.2006

33. Doderer C, Heschung A, Guntz P, et al. A new ELISA kit which uses a combination of Plasmodium falciparum extract and recombinant Plasmodium vivax antigens as an alternative to IFAT for detection of malaria antibodies. *Malar J*. 2007;6:1-8. doi:10.1186/1475-2875-6-19

34. Mahdavi SA, Raeesi A, Faraji L, Youssefi MR, Rahimi MT. Malaria or flu? A case report of misdiagnosis. *Asian Pac J Trop Biomed*. 2014;4(Suppl 1):S56-S58. doi:10.12980/APJTB.4.2014C932

35. Health Organization W. Rapid diagnostic tests. Available online: https://www.who.int/teams/global-malaria-programme/case-management/diagnosis/rapid-diagnostic-tests (Acessed on 18 July 2022).

36. Baker J, McCarthy J, Gatton M, et al. Genetic Diversity of Plasmodium falciparum Histidine-Rich Protein 2 (PfHRP2) and Its Effect on the Performance of PfHRP2-Based Rapid Diagnostic Tests. *J Infect Dis*. 2005;192(5):870-877. doi:10.1086/432010

37. Peixoto de Almeida M, Pereira E, Baptista P, et al. Gold Nanoparticles as (Bio)Chemical Sensors. In: *Comprehensive Analytical Chemistry*. Vol 66. ; 2014:529-567. doi:10.1016/B978-0-444-63285-2.00013-4

38. Saha K, Agasti SS, Kim C, Li X, Rotello VM. Gold nanoparticles in chemical and biological sensing. *Chem Rev*. 2012;112(5):2739-2779. doi:10.1021/cr2001178

39. Petryayeva E, Krull UJ. Localized surface plasmon resonance: Nanostructures, bioassays and biosensing-A review. *Anal Chim Acta*. 2011;706(1):8-24. doi:10.1016/j.aca.2011.08.020

40. Ou J, Zhou Z, Chen Z, Tan H. Optical diagnostic based on functionalized gold nanoparticles. *Int J Mol Sci*. 2019;20(18). doi:10.3390/ijms20184346

41. Nehl CL, Hafner JH. Shape-dependent plasmon resonances of gold nanoparticles. *J Mater Chem*. 2008;18(21):2415-2419. doi:10.1039/b714950f

42. D. Howes P, Rana S, M. Stevens M. Plasmonic nanomaterials for biodiagnostics. *Chem Soc Rev*. 2014;43(11):3835-3853. doi:10.1039/c3cs60346f

43. Nehl CL, Liao H, Hafner JH. Optical properties of star-shaped gold nanoparticles. *Nano Lett*. 2006;6(4):683-688. doi:10.1021/nl052409y

44. Afrooz ARMN, Sivalapalan ST, Murphy CJ, Hussain SM, Schlager JJ, Saleh NB. Spheres vs. rods: The shape of gold nanoparticles influences aggregation and deposition behavior. *Chemosphere*. 2013;91(1):93-98. doi:10.1016/j.chemosphere.2012.11.031

45. Favi PM, Gao M, Johana Sepúlveda Arango L, et al. Shape and surface effects on the cytotoxicity of nanoparticles: Gold nanospheres versus gold nanostars. *J Biomed Mater Res - Part A*. 2015;103(11):3449-3462. doi:10.1002/jbm.a.35491

46. Bagheri S, Yasemi M, Safaie-Qamsari E, et al. Using gold nanoparticles in diagnosis and treatment of melanoma cancer. *Artif Cells, Nanomedicine, Biotechnol*. 2018;46(sup1):462-471. doi:10.1080/21691401.2018.1430585

47. Jiang P, Wang Y, Zhao L, Ji C, Chen D, Nie L. Applications of gold nanoparticles in non-optical biosensors. *Nanomaterials*. 2018;8(12):1-23. doi:10.3390/nano8120977

48. Oliveira MJ, Quaresma P, De Almeida MP, et al. Office paper decorated with silver nanostars - an alternative cost effective platform for trace analyte detection by SERS. *Sci Rep*.

2017;7(1):1-14. doi:10.1038/s41598-017-02484-8

49. Wang Y, Yan B, Chen L. SERS Tags: Novel optical nanoprobes for bioanalysis. *Chem Rev*. 2013;113(3):1391-1428. doi:10.1021/cr300120g

50. Schlücker S. SERS microscopy: Nanoparticle probes and biomedical applications. *ChemPhysChem*. 2009;10(9-10):1344-1354. doi:10.1002/cphc.200900119

51. Xia F, Zuo X, Yang R, et al. Colorimetric detection of DNA, small molecules, proteins, and ions using unmodified gold nanoparticles and conjugated polyelectrolytes. *Proc Natl Acad Sci U S A*. 2010;107(24):10837-10841. doi:10.1073/pnas.1005632107

52. Shrivastav AM, Cvelbar U, Abdulhalim I. A comprehensive review on plasmonic-based biosensors used in viral diagnostics. *Commun Biol*. 2021;4(1):1-12. doi:10.1038/s42003-020-01615-8

53. Cialla D, März A, Böhme R, et al. Surface-enhanced Raman spectroscopy (SERS): Progress and trends. *Anal Bioanal Chem*. 2012;403(1):27-54. doi:10.1007/s00216-011-5631-x

54. Jones RR, Hooper DC, Zhang L, Wolverson D, Valev VK. Raman Techniques: Fundamentals and Frontiers. *Nanoscale Res Lett*. 2019;14(1). doi:10.1186/s11671-019-3039-2

55. Langer J, de Aberasturi DJ, Aizpurua J, et al. Present and future of surface-enhanced Raman scattering. *ACS Nano*. 2020;14(1):28-117. doi:10.1021/acsnano.9b04224

56. Schlücker S. Surface-Enhanced Raman Spectroscopy: Concepts and Chemical Applications. *Angew Chemie Int Ed*. 2014;53(19):4756-4795. doi:10.1002/anie.201205748

57. Oliveira MJ, Cunha I, de Almeida MP, et al. Reusable and highly sensitive SERS immunoassay utilizing gold nanostars and a cellulose hydrogel-based platform. *J Mater Chem B*. 2021;9(36):7516-7529. doi:10.1039/D1TB01404H

58. Xia X, Li W, Zhang Y, Xia Y. Silica-coated dimers of silver nanospheres as surface-enhanced Raman scattering tags for imaging cancer cells. *Interface Focus*. 2013;3(3). doi:10.1098/rsfs.2012.0092

59. Mir-Simon B, Reche-Perez I, Guerrini L, Pazos-Perez N, Alvarez-Puebla RA. Universal one-pot and scalable synthesis of SERS encoded nanoparticles. *Chem Mater*. 2015;27(3):950-958. doi:10.1021/cm504251h

60. Khan I, Saeed K, Khan I. Nanoparticles: Properties, applications and toxicities. *Arab J Chem*. 2017;12(7):908-931. doi:10.1016/j.arabjc.2017.05.011

61. Ojea-Jiménez I, Bastús NG, Puntes V. Influence of the sequence of the reagents addition in the

citrate-mediated synthesis of gold nanoparticles. *J Phys Chem C*. 2011;115(32):15752-15757. doi:10.1021/jp2017242

62. Turkevich J, Stevenson PC, Hillier J. A Study of the Nucleation and Growth Processes in the Synthesis of Colloidal Gold. Published online 1951.

63. Daruich De Souza C, Ribeiro Nogueira B, Rostelato MECM. Review of the methodologies used in the synthesis gold nanoparticles by chemical reduction. *J Alloys Compd*. 2019;798:714-740. doi:10.1016/j.jallcom.2019.05.153

64. Grzelczak M, Pérez-Juste J, Mulvaney P, Liz-Marzán LM. Shape control in gold nanoparticle synthesis. *Chem Soc Rev*. 2008;37(9):1783-1791. doi:10.1039/b711490g

65. Zou X, Ying E, Dong S. Seed-mediated synthesis of branched gold nanoparticles with the assistance of citrate and their surface-enhanced Raman scattering properties. *Nanotechnology*. 2006;17(18):4758-4764. doi:10.1088/0957-4484/17/18/038

66. Yuan H, Khoury CG, Hwang H, Wilson CM, Grant GA, Vo-Dinh T. Gold nanostars: Surfactant-free synthesis, 3D modelling, and two-photon photoluminescence imaging. *Nanotechnology*. 2012;23(7). doi:10.1088/0957-4484/23/7/075102

67. Michota A, Bukowska J. Surface-enhanced Raman scattering (SERS) of 4-mercaptobenzoic acid on silver and gold substrates. *J Raman Spectrosc*. 2003;34(1):21-25. doi:10.1002/jrs.928

68. Oliveira MJ, de Almeida MP, Nunes D, et al. Design and simple assembly of gold nanostar bioconjugates for surface-enhanced raman spectroscopy immunoassays. *Nanomaterials*. 2019;9(11). doi:10.3390/nano9111561

69. Jazayeri MH, Amani H, Pourfatollah AA, Pazoki-Toroudi H, Sedighimoghaddam B. Various methods of gold nanoparticles (GNPs) conjugation to antibodies. *Sens Bio-Sensing Res*. 2016;9:17-22. doi:10.1016/j.sbsr.2016.04.002

70. Bartczak D, Kanaras AG. Preparation of Peptide-Functionalized Gold Nanoparticles Using One Pot EDC/Sulfo-NHS Coupling. *Langmuir*. 2011;27(16):10119-10123. doi:10.1021/la2022177

71. Tomás AL, de Almeida MP, Cardoso F, et al. Development of a Gold Nanoparticle-Based Lateral-Flow Immunoassay for Pneumocystis Pneumonia Serological Diagnosis at Point-of-Care. *Front Microbiol*. 2019;10. doi:10.3389/fmicb.2019.02917

72. Wang L, Wang X, Cheng L, et al. SERS-based test strips: Principles, designs and applications. *Biosens Bioelectron*. 2021;189:113360. doi:10.1016/j.bios.2021.113360

73. Bahadır EB, Sezgintürk MK. Lateral flow assays: Principles, designs and labels. *TrAC Trends Anal Chem*. 2016;82:286-306. doi:10.1016/j.trac.2016.06.006

74. Koczula KM, Gallotta A. Lateral flow assays. Estrela P, ed. *Essays Biochem*. 2016;60(1):111-120. doi:10.1042/EBC20150012

75. Parolo C, Sena-Torralba A, Bergua JF, et al. Tutorial: design and fabrication of nanoparticle-based lateral-flow immunoassays. *Nat Protoc*. 2020;15(12):3788-3816. doi:10.1038/s41596-020-0357-x

76. Sánchez-Purrà M, Carré-Camps M, De Puig H, Bosch I, Gehrke L, Hamad-Schifferli K. Surface-Enhanced Raman Spectroscopy-Based Sandwich Immunoassays for Multiplexed Detection of Zika and Dengue Viral Biomarkers. *ACS Infect Dis*. 2017;3(10):767-776. doi:10.1021/acsinfecdis.7b00110

77. Lin L-K, Stanciu LA. Bisphenol A detection using gold nanostars in a SERS improved lateral flow immunochromatographic assay. *Sensors Actuators B Chem*. 2018;276:222-229. doi:10.1016/j.snb.2018.08.068

78. Zhang W, Tang S, Jin Y, et al. Multiplex SERS-based lateral flow immunosensor for the detection of major mycotoxins in maize utilizing dual Raman labels and triple test lines. *J Hazard Mater*. 2020;393(February):122348. doi:10.1016/j.jhazmat.2020.122348

79. 3, 3′, 5 5′-Tetramethylbenzidine. Available online: https://www.sigmaaldrich.com/deepweb/assets/sigmaaldrich/product/documents/342/708/t2885pis.pdf (Acessed on 17 February 2022).

80. Smith PK, Krohn RI, Hermanson GT, et al. Measurement of protein using bicinchoninic acid. *Anal Biochem*. 1985;150(1):76-85. doi:10.1016/0003-2697(85)90442-7

81. Preparation of the BCA working reagent (WR) Microplate procedure (sample to WR ratio = 1:8). *Available Online: Https://Assets.Thermofisher.Com/TFS-Assets/LSG/Manuals/MAN0011430_Pierce_BCA_Protein_Asy_UG.Pdf (Acessed on 4 October 2021).*

82. Lin W, Zhang RW, Jang SS, Wong CP, Hong J Il. Organic aqua regia-Powerful liquids for dissolving noble metals. *Angew Chemie - Int Ed*. 2010;49(43):7929-7932. doi:10.1002/anie.201001244

83. Turkevich J. Colloidal gold. Part II - Colour, coagulation, adhesion, alloying and catalytic properties. *Gold Bull*. 1985;18(4):125-131. doi:10.1007/BF03214694

84. Haiss W, Thanh NTK, Aveyard J, Fernig DG. Determination of size and concentration of gold

nanoparticles from UV-Vis spectra. *Anal Chem*. 2007;79(11):4215-4221. doi:10.1021/ac0702084

85. Swinehart DF. The Beer-Lambert law. *J Chem Educ*. 1962;39(7):333-335. doi:10.1021/ed039p333

86. Sánchez-Purrà M, Roig-Solvas B, Rodriguez-Quijada C, Leonardo BM, Hamad-Schifferli K. Reporter Selection for Nanotags in Multiplexed Surface Enhanced Raman Spectroscopy Assays. *ACS Omega*. 2018;3(9):10733-10742. doi:10.1021/acsomega.8b01499

87. Enzymatic Assay of PEROXIDASE (EC 1.11.1.7) 2 2'-Azino-bis(3-Ethylbenzthiazoline-6-Sulfonic Acid) as a subtrate. Available Online: https://www.sigmaaldrich.com/PT/En/technical-documents/protocol/protein-biology/enzyme-activity-assays/enzymatic-assay-of-peroxidase-abts-as-substrate (Acessed on 15 October 2021).

88. Bhattacharjee S. DLS and zeta potential – What they are and what they are not? *J Control Release*. 2016;235:337-351. doi:10.1016/j.jconrel.2016.06.017

89. Sheskin DJ. *Handbook of Parametric and Nonparametric Statistical Procedures*. 5th Editio. Chapman and Hall/CRC; 2020. doi:10.1201/9780429186196

90. Shapiro ASS, Wilk MB. An Analysis of Variance Test for Normality (Complete Samples). *Biometrika*. 1965;52(3):591-611. https://pdfs.semanticscholar.org/1f1d/9a7151d52c2e26d35690dbc7ae8098beee22.pdf

91. Grubbs FE. Sample Criteria for Testing Outlying Observations. *Ann Math Stat*. 1950;21(1):27-58. doi:10.1214/aoms/1177729885

92. Welch ABL. The Generalization of `Student ' s' Problem when Several Different Population Variances are Involved. *Biometrika*. 1947;34(1):28-35.

93. Munroe PT. ANOVA (Analysis of Variance). *Blackwell Encycl Sociol*. Published online 2015. doi:10.1002/9781405165518.wbeosa055.pub2

94. Tukey JW. The philosophy of multiple comparisons. *Stat Sci*. 1991;6(1):100-116. doi:10.1214/ss/1177011945

95. Kricka LJ. *Nonisotopic DNA Probe Techniques*. Academic Press; 1992.

96. Welinder KG. Covalent structure of the glycoprotein horseradish peroxidase (EC 1.11.1.7). *FEBS Lett*. 1976;72(1):19-23. doi:10.1016/0014-5793(76)80804-6

97. Mahmood T, Yang PC. Western blot: Technique, theory, and trouble shooting. *N Am J Med*

Sci. 2012;4(9):429-434. doi:10.4103/1947-2714.100998

98. Kurien BT, Scofield RH. Western blotting. *Methods*. 2006;38(4):283-293. doi:10.1016/j.ymeth.2005.11.007

99. Rock EP, Marsh K, Taylor DW, et al. Comparative analysis of the Plasmodium falciparum histidine-rich proteins HRP-I, HRP-II and HRP-III in malaria parasites of diverse origin. *Parasitology*. 1987;95(2):209-227. doi:10.1017/S0031182000057681

100. Wellems TE, Howard RJ. Homologous genes encode two distinct histidine-rich proteins in a cloned isolate of Plasmodium falciparum. *Proc Natl Acad Sci U S A*. 1986;83(16):6065-6069. doi:10.1073/pnas.83.16.6065

101. Schneider EL, King DS, Marletta MA. Amino acid substitution and modification resulting from Escherichia coli expression of recombinant Plasmodium falciparum histidine-rich protein II. *Biochemistry*. 2005;44(3):987-995. doi:10.1021/bi048571h

102. Robichon C, Luo J, Causey TB, Benner JS, Samuelson JC. Engineering Escherichia coli BL21(DE3) derivative strains to minimize E. coli Protein contamination after purification by immobilized metal affinity chromatography. *Appl Environ Microbiol*. 2011;77(13):4634-4646. doi:10.1128/AEM.00119-11

103. Carvalho DW de. Bioengineered Gold Nanostars For One-pot Separation & Immunodetection of a Recombinant Malaria Antigen, Master thesis. Published online 2021.

104. Ahmed W, Stefan Kooij E, Van Silfhout A, Poelsema B. Controlling the morphology of multi-branched gold nanoparticles. *Nanotechnology*. 2010;21(12). doi:10.1088/0957-4484/21/12/125605

105. Oliveira MJ. Nanosers Microfluidics Platform for Rapid Screening for Infectious Diseases. PhD thesis. Unpublished.

106. Giannini V, Rodríguez-Oliveros R, Sánchez-Gil JA. Surface plasmon resonances of metallic nanostars/nanoflowers for surface-enhanced Raman scattering. *Plasmonics*. 2010;5(1):99-104. doi:10.1007/s11468-009-9121-3

107. Xiao Y, Isaacs SN. Enzyme-linked immunosorbent assay (ELISA) and blocking with bovine serum albumin (BSA)-not all BSAs are alike. *J Immunol Methods*. 2012;384(1-2):148-151. doi:10.1016/j.jim.2012.06.009

108. Medda L, Monduzzi M, Salis A. The molecular motion of bovine serum albumin under physiological conditions is ion specific. *Chem Commun*. 2015;51(30):6663-6666. doi:10.1039/c5cc01538c

109. Rabe M, Verdes D, Seeger S. Understanding protein adsorption phenomena at solid surfaces. *Adv Colloid Interface Sci*. 2011;162(1-2):87-106. doi:10.1016/j.cis.2010.12.007

110. Avvakumova S, Pandolfi L, Soprano E, et al. Does conjugation strategy matter? Cetuximab-conjugated gold nanocages for targeting triple-negative breast cancer cells. *Nanoscale Adv*. 2019;1(9):3626-3638. doi:10.1039/c9na00241c

111. Dominguez-Medina S, McDonough S, Swanglap P, Landes CF, Link S. In situ measurement of bovine serum albumin interaction with gold nanospheres. *Langmuir*. 2012;28(24):9131-9139. doi:10.1021/la3005213

112. Zhong R, Liu Y, Zhang P, Liu J, Zhao G, Zhang F. Discrete nanoparticle-BSA conjugates manipulated by hydrophobic interaction. *ACS Appl Mater Interfaces*. 2014;6(22):19465-19470. doi:10.1021/am506497s

113. Gomes I, Feio MJ, Santos NC, et al. Controlled adsorption of cytochrome c to nanostructured gold surfaces. *J Nanoparticle Res*. 2012;14(12). doi:10.1007/s11051-012-1321-7

114. Cui M, Liu R, Deng Z, Ge G, Liu Y, Xie L. Quantitative study of protein coronas on gold nanoparticles with different surface modifications. *Nano Res*. 2014;7(3):345-352. doi:10.1007/s12274-013-0400-0

115. Puertas S, Batalla P, Moros M, et al. Taking Advantage of Unspecific Interactions to Produce Highly Active Magnetic Nanoparticle−Antibody Conjugates. *ACS Nano*. 2011;5(6):4521-4528. doi:10.1021/nn200019s

116. Tsumoto K, Ogasahara K, Ueda Y, Watanabe K, Yutani K, Kumagai I. Role of salt bridge formation in antigen-antibody interaction: Entropic contribution to the complex between hen egg white lysozyme and its monoclonal antibody HyHEL10. *J Biol Chem*. 1996;271(51):32612-32616. doi:10.1074/jbc.271.51.32612

117. Bizmark N, Ioannidis MA. Effects of Ionic Strength on the Colloidal Stability and Interfacial Assembly of Hydrophobic Ethyl Cellulose Nanoparticles. *Langmuir*. 2015;31(34):9282-9289. doi:10.1021/acs.langmuir.5b01857

118. Glomm WR. Functionalized gold nanoparticles for applications in bionanotechnology. *J Dispers Sci Technol*. 2005;26(3):389-414. doi:10.1081/DIS-200052457

119. Liu J, Legros S, Ma G, Veinot JGC, Kammer F Von Der, Hofmann T. Influence of surface functionalization and particle size on the aggregation kinetics of engineered nanoparticles. *Chemosphere*. 2012;87(8):918-924. doi:10.1016/j.chemosphere.2012.01.045

120. Kah JCY, Zubieta A, Saavedra RA, Hamad-Schifferli K. Stability of gold nanorods passivated

with amphiphilic ligands. *Langmuir*. 2012;28(24):8834-8844. doi:10.1021/la3000944

121. Tripathi K, Driskell JD. Quantifying Bound and Active Antibodies Conjugated to Gold Nanoparticles: A Comprehensive and Robust Approach to Evaluate Immobilization Chemistry. *ACS Omega*. 2018;3(7):8253-8259. doi:10.1021/acsomega.8b00591

122. Zheng T, Cherubin P, Cilenti L, Teter K, Huo Q. A simple and fast method to study the hydrodynamic size difference of protein disulfide isomerase in oxidized and reduced form using gold nanoparticles and dynamic light scattering. *Analyst*. 2016;141(3):934-938. doi:10.1039/c5an02248g

123. Wangoo N, Suri CR, Shekhawat G. Interaction of gold nanoparticles with protein: A spectroscopic study to monitor protein conformational changes. *Appl Phys Lett*. 2008;92(13):1-4. doi:10.1063/1.2902302

124. Danaei M, Dehghankhold M, Ataei S, et al. Impact of particle size and polydispersity index on the clinical applications of lipidic nanocarrier systems. *Pharmaceutics*. 2018;10(2):1-17. doi:10.3390/pharmaceutics10020057

125. Hartig SM. Basic image analysis and manipulation in ImageJ. *Curr Protoc Mol Biol*. 2013;(SUPPL.102):1-12. doi:10.1002/0471142727.mb1415s102

126. Diagnostic - Product Guide - Advanced Microdevices. Available Online: https://mdimembrane.com/system/product_catalog/Diagnostic%20Product%20Guide.pdf (Acessed on 8 March 2022). https://mdimembrane.com/system/product_catalog/Diagnostic Product Guide.pdf

127. Jeon J, Lee SH, Joung Y, Kim K, Choi N, Choo J. Improvement of reproducibility and thermal stability of surface-enhanced Raman scattering-based lateral flow assay strips using silica-encapsulated gold nanoparticles. *Sensors Actuators, B Chem*. 2020;321(April):128521. doi:10.1016/j.snb.2020.128521

128. Peng F, Wang Z, Zhang S, et al. Development of an Immunochromatographic Strip for Rapid Detection of H9 Subtype Avian Influenza Viruses. *Clin Vaccine Immunol*. 2008;15(3):569-574. doi:10.1128/CVI.00273-07

129. Xiao M, Xie K, Dong X, et al. Ultrasensitive detection of avian influenza A (H7N9) virus using surface-enhanced Raman scattering-based lateral flow immunoassay strips. *Anal Chim Acta*. 2019;1053:139-147. doi:10.1016/j.aca.2018.11.056

130. Li R, Lv H, Zhang X, et al. Vibrational spectroscopy and density functional theory study of 4-mercaptobenzoic acid. *Spectrochim Acta Part A Mol Biomol Spectrosc*. 2015;148:369-374.

doi:10.1016/j.saa.2015.03.132

131. Wiley JH, Atalla RH. Band assignments in the raman spectra of celluloses. *Carbohydr Res*. 1987;160:113-129. doi:10.1016/0008-6215(87)80306-3

132. Österberg M, Schmidt U, Jääskeläinen AS. Combining confocal Raman spectroscopy and atomic force microscopy to study wood extractives on cellulose surfaces. *Colloids Surfaces A Physicochem Eng Asp*. 2006;291(1-3):197-201. doi:10.1016/j.colsurfa.2006.06.039

133. Schlücker S, Kömpe K, Gellner M. Multiplexing with SERS labels using mixed SAMs of raman reporter molecules. *Anal Bioanal Chem*. 2009;394(7):1839-1844. doi:10.1007/s00216-009-2868-8

134. Tan Z, Zhang Y, Thackray BD, Ye J. Improvement of surface-enhanced Raman scattering detection and imaging by multivariate curve resolution methods. *J Appl Phys*. 2019;125(17). doi:10.1063/1.5091477

135. Byrne HJ, Knief P, Keating ME, Bonnier F. Spectral pre and post processing for infrared and Raman spectroscopy of biological tissues and cells. *Chem Soc Rev*. 2016;45(7):1865-1878. doi:10.1039/c5cs00440c

136. Choi JR, Yong KW, Tang R, et al. Lateral Flow Assay Based on Paper–Hydrogel Hybrid Material for Sensitive Point-of-Care Detection of Dengue Virus. *Adv Healthc Mater*. 2017;6(1):1-9. doi:10.1002/adhm.201600920

137. Zakaria HM, Shah A, Konieczny M, Hoffmann JA, Nijdam AJ, Reeves ME. Small Molecule and Amino Acid Induced Aggregation of Gold Nanoparticles. *Langmuir*. 2013;29(25):7661-7673. doi:10.1021/la400582v

A

APPENDICES

A.1 Ni-NTA column regeneration

The column was regenerated with 0.1 M ethylenediamine tetraacetic acid (EDTA, ≥ 98%, Honeywell Fluka – Thermo Fisher Scientific, Waltham, USA) and 0.5 M NaCl at pH 7.5, this allows to remove all metal ions in the solid phase and remove any bound materials such as proteins. Then, the resin was washed thoroughly with ultrapure water (H_2O, 18 MΩ·cm at 25ºC). To restore the column, a solution of 0.1 M of nickel chloride hexahydrate (Sigma-Aldrich, St. Louis, MO, USA) was circulated in the column for 10 min followed by washing with ultrapure water immediately before using the column.

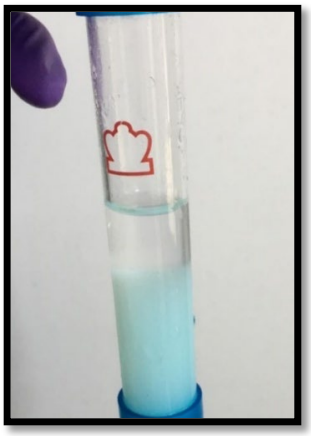

Figure A.1: Ni-NTA column after regeneration and restored with nickel chloride hexahydrate.

A.2 Synthesis of spherical and star-shaped gold nanoparticles

During this Thesis, two batches of AuNPs were synthesised, and as seen in the Figure A.2 the UV-Vis spectrum obtained were identical with the same LSPR band. For AuNSs, several batches were synthesised, and as seen in the Figure A.3 are represented a few of these batches.

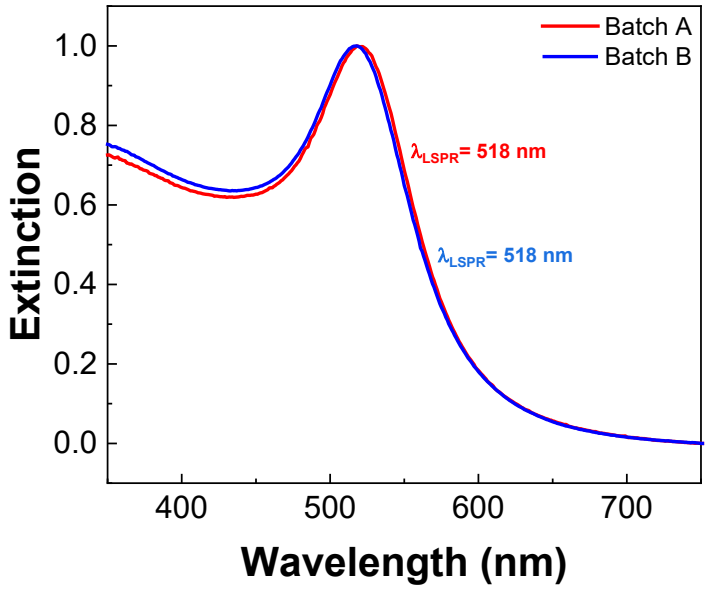

Figure A.2: UV-Vis characterisation of the two batches AuNPs synthetised. Normalised UV-Vis spectrum taken immediately after both AuNPs synthesis, with a LSPR band at 518 nm.

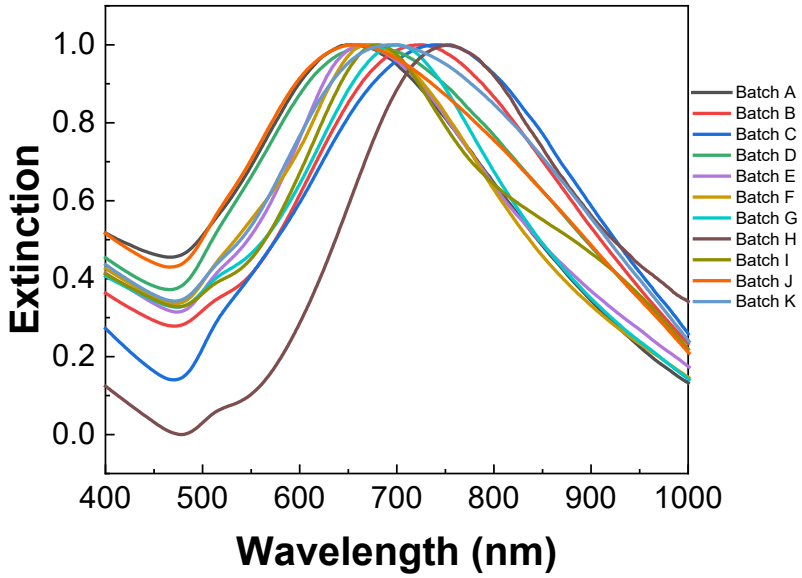

Figure A.3: UV-Vis characterisation of several batches AuNSs synthetised. The batches A-K had LSPR bands between 651 and 739 nm.

A.3 Star-shaped gold nanoparticles conjugation with BSA at pH 5.5

The samples with AuNSs-MBA at varying molar concentrations of BSA at pH 5.5 demonstrated a high variability in electrophoretic mobilities even between triplicates of the same condition as can be seen in Figure A.4. For higher molar concentrations of BSA, the samples had more electrophoretic mobility, which may be explained by the coating of AuNSs-MBA with more BSA. However, the electrophoretic mobility varies between the triplicates, which indicates that at this pH, the AGE was not reproductible. Is possible that this phenomenon is related to the stochastic behaviour of NP aggregation[137] induced at pH 5.5.

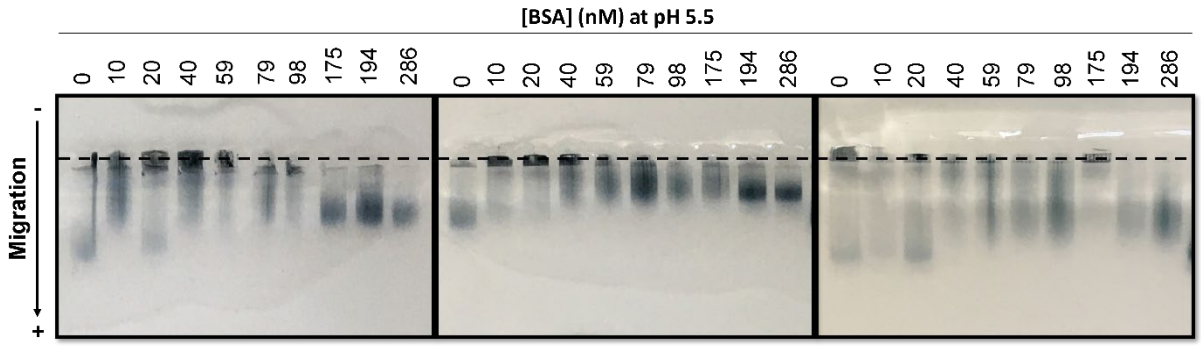

Figure A.4: Digital image of triplicates AGE with sample of AuNSs-MBA incubated with several BSA final concentrations (from 0 to 286 nM) at pH 5.5.

I

ANNEXES

I.1 Equipment

The equipment used during this Thesis is listed below.

Table I.1: Table of equipment used.

Equipment	Supplier
Gallenkamp Orbital Shaker Incubator	Cambridge, United Kingdom
Centrifuge Beckman Coulter Avanti J26-XPI with a JA-10 rotor	California, USA
Centrifuge tubes	Beckman Coulter , California, USA
French pressure cell press	Thermo Electron Corporation – Thermo Fisher Scientific, Waltham, USA
Ultracentrifuge	Beckman Optima LE-80K , California, USA
Amicon Ultra-4 Centrifugal Filter Units, 30k, 4 mL	Merck Millipore, Cork, Ireland
Mini-rocking shaker	Biosan, Latvia
Polyvinylidene difluoride membrane (PVDF)	Sigma-Aldrich, St. Louis, MO, USA
0.20 µm syringe filter	GVS North America, Sandford, USA
UV-Vis spectrophotometer	Cary 50 Bio, Varian®, San Francisco, CA, USA
Quartz cells witch 1 cm and 3 mm of path-length	Hellma®, Müllheim, Germany
Centurion Scientific K3 Series centrifuge	North America by Core Life Sciences, USA
Orbital shaker	Biosan TS-100, Latvia

LFA started kit	Advanced Microdevices, Ambala Cantt, India
Mini-sub cell GT and Mini-sub cell GT	Bio-Rad, Portugal
SZ-100 Nanopartica series	Horiba, Japan
Desiccator	Vacuo-Temp, JP Selecta, Barcelona, Spain
Renishaw inVia Qontor micro-Raman spectrometer	Renishaw Iberica S.A.U., Barcelona, Spain

I.2 ImageJ analysis

A digital picture was taken of all the LFA tests 30 min after every test. These digital pictures were analysed by image analysis software (Image J, National Institutes of Health, https://imagej.nih.gov/ij/) by selecting three squares with the same size of the test and control line, and background. As seen an example in the Figure I.1a, a total nine squares were selected in the digital picture of LFA, and from each square was obtained the mean, median, standard deviation, among others, of intensity of each pixel (Figure I.1b). More importantly, a histogram from each square was obtained (Figure I.1c), which values were used to compare the intensity (pixel) of background and test and control lines.

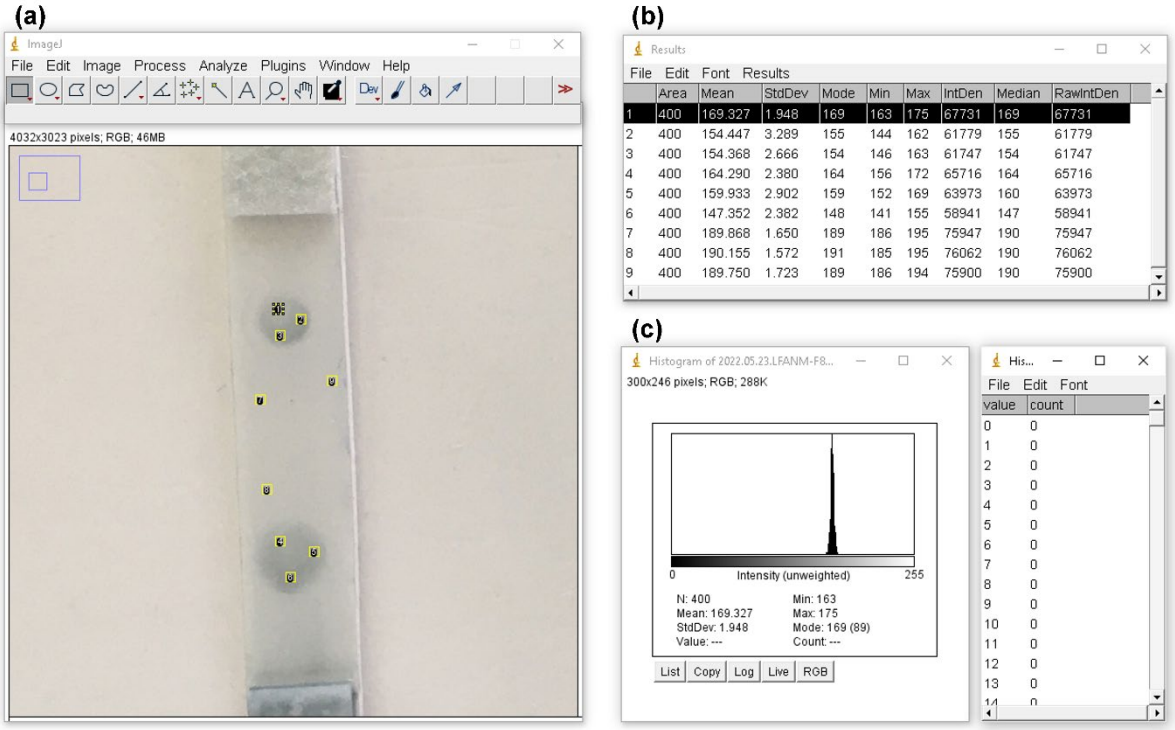

Figure I.1: Analysis of LFA digital pictures by ImageJ software. (a) Three squares from the background, test and control line of the same size were selected to the analysis. (b) From each square was obtained the mean, median, mode, minimum, maxi-

mum and standard deviation of intensity of each pixel. (c) Histogram of each square was obtained, as example for the first square selected, which in a scale from 0 to 255 pixel (black to white) the intensity was analysed and compared (background, test, and control line).